



HAL
open science

Dynamics of flexible and Brownian filaments in viscous flow

Yanan Liu

► **To cite this version:**

Yanan Liu. Dynamics of flexible and Brownian filaments in viscous flow. Physics [physics]. Université Sorbonne Paris Cité, 2018. English. NNT : 2018USPCC196 . tel-02451935

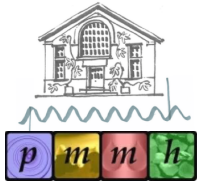
HAL Id: tel-02451935

<https://theses.hal.science/tel-02451935>

Submitted on 23 Jan 2020

HAL is a multi-disciplinary open access archive for the deposit and dissemination of scientific research documents, whether they are published or not. The documents may come from teaching and research institutions in France or abroad, or from public or private research centers.

L'archive ouverte pluridisciplinaire **HAL**, est destinée au dépôt et à la diffusion de documents scientifiques de niveau recherche, publiés ou non, émanant des établissements d'enseignement et de recherche français ou étrangers, des laboratoires publics ou privés.



THÈSE DE DOCTORAT DE L'UNIVERSITÉ SORBONNE PARIS CITÉ

Spécialité : Physique

préparée à

l'Université Paris Diderot

École doctorale n° 564 : Physique en Île-de-France

Laboratoire de Physique et Mécanique des Milieux Hétérogènes

Yanan LIU

sur le sujet :

Dynamics of flexible and Brownian filaments in viscous flows

soutenue le 24 septembre 2018

sous la direction de: **Anke LINDNER & Olivia DU ROURE**

devant le jury composé de:

M. CLEMENT Eric	Professeur (IMFT)	Rapporteur
M. LETTINGA Pavlik	Professeur (Forschungszentrum Jülich)	Rapporteur
M. DESCHAMPS Julien	Maître de Conférences (IRPHE)	Examineur
Mme. FAUCI Lisa	Professeur (Tulane University)	Examinatrice
Mme. LEROUGE Sandra	Professeur (MSC Paris Diderot)	Président du jury
Mme. Olivia du Roure	Directeur de recherche (PMMH CNRS)	Directrice de thèse
Mme. LINDNER Anke	Professeur (PMMH Paris Diderot)	Directrice de thèse

This thesis is dedicated to:
my parents, my sister, my husband.

致父母，妹妹，爱人。

Acknowledgement

The work reported in this dissertation was carried out in PMMH (Physique et Mécanique des Milieux Hétérogènes), from October 2014 to September 2018. I spent a wonderful time here with so many nice people, providing me many help in my study and life.

First of all, I would like to sincerely appreciate my supervisors: Prof. Anke Lindner and Prof. Olivia Du Roure for their encouragements, positive attitudes, generous supportings, successive efforts and patient guidances to my project. I have been extremely lucky to be their students and their behaviors will be the models of my future research.

I would like to appreciate Brato Chakrabarti and his supervisor Prof. David Saintillan for pleasant and fruitful discussions and collaboration, which helped me a lot to understand my work from another view.

I would like to thank Prof. Guillaume Romet-Lemonne and Doctor Antoine Jégou for providing actin monomers and discussions. I also would like to thank Prof. Lisa Fauci, Prof. Michael Shelley, Prof. Jing Guangyin, Doctor Harishankar Manikantan for the contributive discussions. I also would like to thank engineers, Thierry Darnige, Xavier Benoit Gonin for technical supporting.

I would like to express my gratitude to my fellow research colleagues, Adeline Favier, Charles Duchene, Jia Pan, Jessica Planade, Marine Daïeff, Jean Cappello, Joana Fidalgo, Francesca Tesser, Vincent Gognet, for the discussions, accompany and help in my study and daily life. I also would like to express my gratitude to my friends, Zhang tianzhen, Jiangye, Chen yinjun, Zhao menghua, Guo hui, Tian ye, Wang hongyue, Lin hongru, Pan teng, for their accompany and help in my life abroad.

I would like to acknowledge financial support from China Scholarship Council, ERC Consolidator Grant No. 682367 as well as COST (European Cooperation in Science & Technology).

At last, I would like to express my most sincere gratitude to my families, my dear parents Liu Baozhong and Lu Jie, my dear little sister Liu jie, and my dear husband Wang jun, for their love and accompany.

Abstract

The dynamics of an individual flexible filaments in viscous flows is the key to deciphering the rheological behavior of many complex fluids and soft materials. It also underlies a wealth of biophysical processes from flagellar propulsion to intracellular streaming. This thesis presents systematic experiments to investigate the dynamics of flexible and Brownian filaments in viscous flows. Biopolymer actin has been chosen to be our experimental model filament: its typical length can be varied from 1 to 100 μm , it is flexible at these dimensions with a persistence length in the order of 20 μm , it is Brownian due to its small diameter with bending fluctuations and it can be labelled by fluorescent dye. Microfluidic channels and flow control systems are combined with optical microscope with an automated stage to carry out well-controlled experiments on the diverse dynamics of actin filaments in shear flow and pure straining flow. In shear flow, simulations matching the experimental conditions have also been performed using inextensible Euler-Bernoulli beam theory and non-local slender body hydrodynamics in the presence of thermal fluctuations and agree quantitatively with the experimental results.

We demonstrate that filament dynamics in this flow geometry is primarily governed by a dimensionless elasto-viscous number comparing viscous forces to elastic forces with thermal fluctuations only playing a secondary role. We present a complete characterization of the different modes of deformation undergone by the filament while rotating as well as of the transitions between these different modes. In pure straining flow, we opt to use an optimized hyperbolic channel to allow long residence time at constant strain rate to be applied. We directly observe the suppression of transverse fluctuations in the extensional part of the hyperbolic channel while we observe, in the compressive part of the flow, the formation of three dimensional helical structures subsequent to the initial buckling of the filament. Finally, this thesis manuscript also reports on experimental developments to fabricate suspensions of actin filament with a narrow distribution of lengths and on preliminary results on shear-thinning effects. All together the results presented here pave the way for future studies towards the understanding of filament dynamics in more complex flows, as Poiseuille flows or oscillatory flows, as well as towards establishing the link between filament deformations and rheological response in dilute suspensions of flexible Brownian filaments, which remains nearly unexplored from an experimental point of view.

Keywords: flexible and Brownian filaments, morphological dynamics, microfluidic, monodisperse suspension, fluid structure interaction

Résumé

La dynamique de filaments flexibles individuels en écoulement visqueux est un étape essentielle pour comprendre et contrôler la rhéologie de nombreux fluides complexes. Cette dynamique sous-tend également une multitude de processus biophysiques allant de la propulsion des micro-organismes aux écoulements intracellulaires. Cette thèse présente des expériences systématiques permettant d'étudier la dynamique de filaments flexibles browniens dans un écoulement visqueux. Nous avons choisi d'utiliser un biopolymère, l'actine, comme système modèle de filaments. Sa longueur typique varie de 1 à 100 μm , il est flexible à ces échelles avec une longueur de persistance de l'ordre de 20 μm , à cause de ses petites dimensions, il est soumis aux forces Browniennes avec des fluctuations en flexion, et enfin il peut être marqué en fluorescence. Nous utilisons des dispositifs microfluidiques associés à des systèmes de contrôle d'écoulements, un microscope optique équipé avec une platine motorisée pour réaliser des expériences contrôlées permettant de suivre la dynamique des filaments d'actine dans un écoulement de cisaillement pur et dans un écoulement élongationnel. Pour les expériences en cisaillement pur, des simulations reproduisant les conditions expérimentales ont aussi été menées en utilisant la théorie des poutres inextensibles de Euler-Bernoulli et la théorie non locale des corps élancés en présence de fluctuations Browniennes et sont en accord quantitatif avec les résultats expérimentaux.

Nous montrons que la dynamique des filaments dans ce système est principalement régie par le nombre élasto-visqueux, nombre sans dimension comparant les forces de traînée visqueuses aux forces de flexion élastiques, les fluctuations thermiques ne jouant qu'un rôle secondaire. Nous présentons une caractérisation complète des différents modes de déformation subies par le filament pendant une rotation ainsi que des transitions entre les différents modes. Dans la géométrie élongationnelle, nous avons choisi un canal hyperbolique optimisé pour permettre de longs temps de résidence sous taux de déformation constant. Nous avons observé directement la suppression des fluctuations transverse dans la partie extensionnelle tandis que nous observons, dans la partie compressive la formation de structures hélicoïdales tridimensionnelles après le flambage du filament. Pour finir, ce manuscrit de thèse décrit des développements expérimentaux permettant de fabriquer des suspensions de filaments d'actine relativement monodisperse en taille ainsi que des résultats préliminaires sur des effets rhéofluidifiants. Au bilan, les résultats présentés dans ce manuscrit pose les premières pierres de travaux futurs en direction de l'étude de la dynamique de ces filaments dans des écoulements plus complexes comme des écoulements de Poiseuille ou oscillants. Ils permettent aussi d'envisager des études sur le lien entre déformations de particules et propriétés des suspensions diluées d'objets flexibles et Brownien, lien encore peu étudié du point de vue expérimental.

Mots clés : filaments flexibles et browniens, dynamique morphologique, microfluidique, suspension diluée, interaction fluide-structure

Contents

Abstract	I
Résumé	II
Nomenclature	VI
1 Introduction	1
1.1 Theoretical formulations	3
1.1.1 Stokes equations and fundamental solutions	3
1.1.2 Slender Body Theory	5
1.1.3 Flexibility and elastohydrodynamics	6
1.1.4 Brownian forces	7
1.2 Elastic filaments in flow	7
1.2.1 Buckling instabilities of a filament in a compressive flow	7
1.2.2 Dynamics of filaments in shear flow	10
1.2.3 From the microscopic to the macroscopic	14
1.3 Conclusion and short description of this manuscript	16
References	16
2 Actin as a flexible filament	21
2.1 Introduction	22
2.1.1 Actin in cells	22
2.1.2 Actin polymerization	23
2.1.3 Filaments characteristics	24
2.2 Method and materials	24
2.2.1 Polymerization protocol	24
2.2.2 Thin chamber with confinement	25
2.2.3 Image processing and shape reconstruction	26
2.3 Characteristics measurement	27
2.3.1 Brownian fluctuations	27
2.3.2 Persistence length ℓ_p	27
2.4 Summary	29
References	29

3	The dynamics of flexible filaments in shear flow	31
3.1	Introduction	32
3.2	Method and materials	32
3.2.1	Experimental setup	32
3.2.2	Microfluidic geometry	33
3.2.3	z correction program	35
3.2.4	Quantitative parameters	36
3.3	Numerical simulations	38
3.4	Morphological dynamics in shear flow	40
3.4.1	Rod-like tumbling	41
3.4.2	C shape buckling with global rotation	42
3.4.3	Snake turn dynamics	43
3.4.4	Complex dynamics	45
3.5	Transitions between different dynamics	46
3.5.1	Order parameters and phase diagram	46
3.5.2	The transition from C buckling to U snake turn	50
3.6	Frequency dynamics in shear flow	56
3.7	Summary	58
	References	59
4	The dynamics of flexible filaments in straining flow	61
4.1	Introduction	62
4.2	Microfluidic device for linear straining flow	63
4.2.1	Optimized hyperbolic channel	63
4.2.2	Experimental Implementation	67
4.3	Filament dynamics	70
4.3.1	Experimental observations	70
4.3.2	Suppression of Brownian fluctuations in extensional flow	73
4.3.3	Buckling and helical coiling under compression	74
4.4	Summary	76
4.5	Discussion and outlook	77
	References	78
5	Actin filament suspensions	81
5.1	Introduction	82
5.2	Microfluidic rheometer	83
5.2.1	Microfluidic geometry	83
5.2.2	Interface detection	84
5.2.3	Y channel viscometer calibration using fluorescein	85
5.3	Monodisperse suspensions	85
5.3.1	A biochemical approach to fabricate monodisperse suspensions	85
5.3.2	Polymerization dynamics	86

5.4 Shear viscosities of actin suspensions	88
5.5 Summary and outlook	90
References	90
6 Conclusion and outlook	93
6.1 Conclusion	94
6.2 Outlook	95
References	96
Appendix A Eigenmodes under tension	99
References	102
Appendix B Monodispersed suspension fabrication	103
Appendix C Tumbling, buckling, snaking: Morphological transitions of elastic filaments in shear flow	105
List of figures	122
List of tables	123

Nomenclature

k_B	Boltzmann constant $1.38 \times 10^{-23} \text{ m}^2 \text{ kg s}^{-2} \text{ K}^{-1}$	c	slenderness
T	Kelvin temperature	\mathbb{G}	stokeslet
ℓ_p	persistence length	\mathbb{D}	doublet
B	bending rigidity	ρ	density
L	contour length of filaments	μ	viscosity
L_{ee}	end-to-end vector	$\bar{\mu}$	elasto-viscous number
E	bending energy	ω	sphericity parameter
d	the diameter of filaments	κ	curvature
s	arc length	Λ	local mobility operator
\mathbf{G}	gyration tensor	σ	Lagrange multiplier, tension
W	channel width	Σ	Dimensionless tension
H	channel height	χ	gyration angle
p	pressure	ϵ	aspect ratio
Q	flow rate	$\dot{\epsilon}$	strain rate
K	integral operator	$\dot{\gamma}$	shear rate

Chapter 1

Introduction

Contents

1.1 Theoretical formulations	3
1.1.1 Stokes equations and fundamental solutions	3
1.1.2 Slender Body Theory	5
1.1.3 Flexibility and elastohydrodynamics	6
1.1.4 Brownian forces	7
1.2 Elastic filaments in flow	7
1.2.1 Buckling instabilities of a filament in a compressive flow	7
1.2.2 Dynamics of filaments in shear flow	10
1.2.2.1 Deformations of elastic fibers in shear flow	11
1.2.2.2 Characteristic frequency dynamics	12
1.2.3 From the microscopic to the macroscopic	14
1.3 Conclusion and short description of this manuscript	16
References	16

General Introduction

In nature and our daily life, complex suspensions, made of particles suspended in a simple fluid like water, are ubiquitous around us. For example, biofluids are mainly water containing different kinds of microscopic structures: long polymer chains in saliva, red and white blood cells in blood, fibers and organelles in the cytoplasm of a cell. Particle suspensions are also very common in industry, from paper pulp or paint to food like ketchup. The way such suspensions flow is tightly linked to the presence and the nature of the particles they contain. When a fluid like water flows under an external force, the relation between the imposed stress and the resulting strain is characterized by a single coefficient of viscosity. Fluids with this behavior are called Newtonian fluids. On the contrary, for non-Newtonian fluids the relation between stress and strain is characterized by a complex function of multiple parameters like the volume fraction, the strain rate etc. Non-Newtonian fluids present a large range of behaviors from strain-rate dependent viscosities, rod climbing effects, to elasto-viscous instability or turbulence.

If we zoom in the microscopic world of flowing suspensions, we will see surprisingly diverse and complex behaviors of particles depending on their individual properties - geometry, size, aspect ratio or elasticity. As soon as the particle has a finite size, it may rotate, deform or cross streamlines as a consequence of its interaction with the flow. In many situations, the coupling between the particle and the fluid is not fully understood. It is, however, a fundamental issue both as the first step of the understanding of suspensions properties but also to many problems at the microscopic scale. Important cellular processes like intracellular transport or micro-organism locomotion, for example, involve the motion of fibers or slender structures in the cytoplasm or in the surrounding medium of a cell. Another new field that would benefit from better understandings of the fluid-structure interaction is lab-on-chip where microfluidic chips are used to do the analysis of biological samples. For these samples, being able to isolate some of the constituents based on their dimensions, shapes or mechanical properties would be very useful both for diagnosis and pre-analysis steps.

The research field has been the place of intense activity for the last 20 years mainly in theoretical and numerical studies. Experimental works are less numerous because of the difficulties that arise when controlled experiments need to be performed. Double stranded DNA has been used as the first model system to study single flexible polymer dynamics in experiments ([Perkins et al., 1997](#); [Smith et al., 1999](#); [Schroeder et al., 2003](#)). The dynamics of flexible polymers is governed by the competition between thermal entropic forces favoring coiled configurations and viscous stresses that tend to stretch the polymer in strain-dominated flows. The interplay between these two effects is responsible for the coil-stretch transition in extensional flows as well as tumbling and stretching motions in shear flows. These microscopic dynamics has been related to the shear-dependent viscosity and normal stress differences, leading to rod climbing and

Weissenberg effects in solutions of long polymers (Bird et al., 1977; Doi and Edwards, 1988).

The case of flexible fibers has received much less attention. Such an elastic filament can undergo a buckling instability due to viscous stress (Becker and Shelley, 2001; Young and Shelley, 2007; Wandersman et al., 2010; Quennouz et al., 2015). This transition from an *elongated/stretch* to a *buckled/coil* shape can be compared to the *coil-stretch* transition observed for coiled polymer. Similarly to the case of long polymer solutions, it has been predicted that the buckling instability yields first normal stress differences in a suspension of flexible filaments in shear flow (Becker and Shelley, 2001). In this context, this PhD thesis aims at understanding the coupling between a flexible fiber and simple flows and establishing the link between the microscopic behavior of the fibers and the suspension properties. Strong emphasis has been put to develop controlled experiments both on the fiber properties and on the flow geometry. The work reported here is mainly experimental but has been complemented by numerical and theoretical approaches developed in close collaboration with Brato Chakrabarti and David Saintillan from University of California, San Diego, USA.

The following chapter is devoted to the presentation of the state of the art of the field and starts with a description of the ingredients of our problem: viscous forces which need to take into account the slenderness of our filament, elastic restoring forces that tend to keep the filament straight and Brownian forces which, due to the dimensions, mainly tend to bend the filament transversally. Note that in this manuscript, *flexible fiber* and *elastic filament* are equivalent as well as any other combination of the words.

1.1 Theoretical formulations

1.1.1 Stokes equations and fundamental solutions

Fluid motion is governed by the well-known Navier-Stokes equations which result from the combination of mass conservation and Newton's laws. The Reynolds number, Re , compares inertial forces to viscous forces within a fluid and determines the flow regimes. Its expression depends on the density of the fluid, ρ , the average velocity of the fluid, u , a characteristic length scale of the problem, L , and the dynamic viscosity of the fluid, μ .

$$Re = \frac{\text{inertial forces}}{\text{viscous forces}} = \frac{\rho u^2}{\mu u/L} = \frac{\rho u L}{\mu} \quad (1.1)$$

High values of the Reynolds number describe inertia-dominated flows which tend to produce chaotic eddies, vortices and other flow instabilities. At low Reynolds numbers,

viscous forces are dominant and flows are laminar. This is the regime of this thesis where we studied the behavior of actin filaments - with typical length of $10\mu m$ - in water - $\rho = 10^3 kg/m^3$ and $\mu = 10^{-3} mPa \cdot s$ - flowing at typical velocities of $10 - 100\mu m/s$ leading to a Reynolds number around 10^{-5} to 10^{-4} . In this flow regime the Navier-Stokes equations reduce into Stokes equations which, due to the incompressibility of water, take the form indicated in Eqn. (1.2) where we denote the velocity field by \mathbf{u} , the pressure by p , and call \mathbf{f} a force acting on the fluid.

$$\begin{aligned} \nabla \cdot \mathbf{u} &= 0 & \text{in } \Omega \\ -\Delta p + \mu \nabla^2 \mathbf{u} + \mathbf{f} &= \mathbf{0} & \text{in } \Omega \end{aligned} \quad (1.2)$$

Here, μ is the viscosity of the fluid, $\Omega = \mathbb{R}^3$. The Stokes equations are linear in velocity and pressure, which leads to a linear relation between the magnitude of the force and fluid velocity. One of the consequences of this linearity is that doubling the pressure gradient yields to the doubling of the flow rate in a pressure driven Stokes flow. The mathematical advantage of this linearity is that the superposition of different solutions gives another solution of the Stokes equations. Another important property of the Stokes equations is the absence of time-dependence leading to instantaneity property of the flow. This implies that motions at low Reynolds numbers are time-reversible which has been beautifully illustrated by G.I. Taylor in a famous film (1966).

The Stokes equations (Eqn. 1.2) need boundary conditions to be fully solved. In fluid-structure interaction problems this is where the presence of the object in the flow enters into account. In general, the no-slip condition is used on the surface of the object Γ and far away the velocity equals the background velocity \mathbf{U}_0 which is also a solution of the Stokes equations:

$$\mathbf{u} = \mathbf{u}_\Gamma \text{ on } \Gamma, \quad \mathbf{u} \rightarrow \mathbf{U}_0 \text{ for } \|\mathbf{r}\| \rightarrow \infty \quad (1.3)$$

If the object is rather slender, like a filament, the full boundary integral on the surface of the filament can be reduced to the integral along the filament centerline. This can be done by using fundamental solutions of Stokes equations. The simplest fundamental solution is called 'Stokeslet' and is the solution due to a point force $\mathbf{F}\delta(\mathbf{R})$, $\delta(\mathbf{R})$ being the Dirac delta function, $\mathbf{R} = \mathbf{r} - \mathbf{r}_0$ represents the separation vector. The solution for the pressure p and velocity \mathbf{u} is here given by,

$$\mathbf{u}(\mathbf{R}) = \mathbf{F} \cdot \mathbb{G}(\mathbf{R}), \quad p(\mathbf{r}) = \frac{\mathbf{F} \cdot \mathbf{R}}{4\pi|\mathbf{R}|^3} \quad (1.4)$$

where $\mathbb{G}(\mathbf{R})$ is the Stokeslet tensor, which reads $\mathbb{G}(\mathbf{R}) = \frac{1}{8\pi\mu} \left(\frac{\mathbf{I} + \mathbf{R}\mathbf{R}}{|\mathbf{R}|} \right)$ with \mathbf{I} the identity

tensor, $\mathbf{R}\mathbf{R}$ the dyadic product of \mathbf{R} and $|\mathbf{R}|$ the magnitude of \mathbf{R} . Higher orders of fundamental solutions can be obtained by differentiation. The next one is called doublet and is expressed as $\mathbb{D}(\mathbf{R}) = \frac{1}{2}\Delta\mathbb{G}(\mathbf{R}) = \frac{1}{8\pi\mu} \frac{\mathbf{I}-3\mathbf{R}\mathbf{R}}{|\mathbf{R}|^3}$.

1.1.2 Slender Body Theory

Thanks to the linearity of the Stokes equations, a general solution can be expressed as the sum of fundamental solutions that satisfy the boundary conditions. The Slender Body Theory approximates the problem by placing fundamental solutions, either stokeslets only (local SBT) or both stokeslets and doublets (non-local SBT) along the centerline of the body. Both local and non-local SBT allow an approximate relationship between the velocity of the filament at each point along the arclength and the force per unit length experienced by the body at that point to be derived. Non-local Slender Body Theory takes into account the hydrodynamic interactions between the different parts of the filament and also between different filaments.

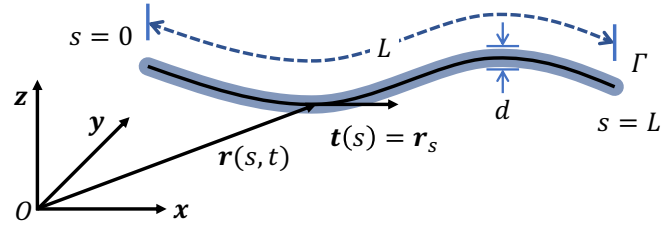


Figure 1.1: Parametrization of the filament. $\mathbf{r}(s, t)$ describes the centerline of the filament along the arclength s , at time t . d is the filament diameter. The tangential vector is the derivative of $\mathbf{r}(s, t)$ with respect to s , $\mathbf{t}(s) = \mathbf{r}_s$.

An approximation of the velocity of the filament centerline in a background flow \mathbf{U}_0 given by non-local SBT has been proposed by (Johnson, 1980),

$$8\pi\mu(\mathbf{r}_t - \mathbf{U}_0(\mathbf{r}, t)) = -\Lambda[\mathbf{f}](s) - K[\mathbf{f}](s) \quad (1.5)$$

with

$$\Lambda[\mathbf{f}] = [-c(\mathbf{I} + \mathbf{r}_s\mathbf{r}_s) + 2(\mathbf{I} - \mathbf{r}_s\mathbf{r}_s)] \cdot \mathbf{f}(s), \quad (1.6)$$

$$K[\mathbf{f}] = \int_0^L \left(\frac{\mathbf{I} + \mathbf{R}\mathbf{R}}{|\mathbf{R}|} \mathbf{f}(s') - \frac{\mathbf{I} + \mathbf{r}_s\mathbf{r}_s}{|s-s'|} \mathbf{f}(s) \right) ds' \quad (1.7)$$

Here, $c = -\ln(\epsilon^2 e)$ is a geometric parameter, \mathbf{f} is the force per unit length on the filament. Λ is a local mobility operator that accounts for drag anisotropy, while the integral

operator K captures the effect of hydrodynamic interactions between different parts of the filament.

1.1.3 Flexibility and elasto-hydrodynamics

We see that the slender body (Eqn. 1.5) connects the velocities of each point along a filament to a force distribution along its centerline. In elasto-hydrodynamics problem like the one studied in this thesis, this force distribution is an elastic one and counterbalance the viscous drag. Thus, the force distribution f along the centerline of the filament has to follow the laws of elasticity (Wiggins et al., 1998). The elastic energy due to bending depends on the curvature but does not depend on the sign of the curvature. It can be expressed as,

$$\mathcal{E} = \frac{1}{2} \int_0^L B r_{ss}^2 ds \quad (1.8)$$

where, L is the length of the filament, r_{ss} is the curvature, and $B = YI$ is the bending rigidity, Y being the Young's modulus and I being the area moment of inertia. The functional derivative of this energy provides a first approximation for the restorative elastic force per unit length on the backbone of the filament.

In the case of very elongated filaments whose length is much larger than the diameter, it is reasonable to regard these filaments as inextensible since the modulations in extension relax much faster than those in bending, the two timescales being different by a factor of $(2L/d)^2$ (Powers, 2010). In order to satisfy the inextensibility constraint, one can introduce the method of Lagrange multiplier. Consider the functional:

$$\mathcal{E} = \frac{1}{2} \int_0^L [B r_{ss}^2 + \sigma(s)(r_s^2 - 1)] ds \quad (1.9)$$

Here, $\sigma(s)$ is a Lagrangian multiplier forcing the filament locally inextensible $\mathbf{r}_s \cdot \mathbf{r}_s = 1$. Physically, $\sigma(s)$ corresponds to a line tension along the centerline of the filament that keeps its length constant. Taking the first variation we get

$$\mathbf{f}(s) = \delta \mathcal{E} = B \mathbf{r}_{ssss} - (\sigma(s) \mathbf{r}_s)_s \quad (1.10)$$

With boundary conditions at free ends:

$$\mathbf{r}_{ss}(s=0, L) = 0, \mathbf{r}_{sss}(s=0, L) = 0 \text{ and } \sigma(s)(s=0, L) = 0.$$

1.1.4 Brownian forces

For micrometer-sized filaments, Brownian forces play a role and can cause diffusion of the centre of mass, rotational diffusion and transverse fluctuations. Fluctuation-dissipation theorem makes possible to model the Brownian forces in the continuum hypothesis. The random fluctuating force acting on an immersed particle is equal to the dissipative frictional force that is required by the mobility of the particle. In the case of filaments, the Brownian force per unit length \mathbf{f}^{br} obeys the fluctuation-dissipation theorem (Munk et al., 2006; Manikantan and Saintillan, 2013) and can be added in Eqn. (1.10) as,

$$\langle \mathbf{f}^{br}(s, t) \rangle = 0, \quad (1.11)$$

$$\langle \mathbf{f}^{br}(s, t) \mathbf{f}^{br}(s', t') \rangle = 2k_B T \mathcal{M}^{-1} \delta(s - s') \delta(t - t') \quad (1.12)$$

Where angle brackets represents an ensemble average, δ is the Dirac delta function, \mathcal{M} is the hydrodynamic mobility of the filament segments.

1.2 Elastic filaments in flow

We will now give an overview of experimental, theoretical and numerical works that have studied different situations where filament(s) interact(s) with a viscous flow. In all these situations, the dynamics is governed by the combination of elastic and viscous forces plus, in certain cases, the Brownian forces. We will start by describing the deformation and transport of isolated filaments in compressive and shear flow and then consider the scale of the suspensions. This part has been written based on different research and review articles: Becker and Shelley (2001); Tornberg and Shelley (2004); Young and Shelley (2007); Duprat and Shore (2015); Lindner et al. (2018).

1.2.1 Buckling instabilities of a filament in a compressive flow

When a flexible filament transports freely in a compressive flow, the viscous stresses applied on the filament may overcome bending resistance and may lead to structural instabilities reminiscent of Euler buckling of elastic beams. How flexible filaments are buckled by flow is a central question to many nonlinear dynamics observed in simulations and experiments. Because of its relative simplicity, local slender body theory is usually favored to study the linear stability of immersed filaments (Becker and Shelley, 2001; Duprat and Shore, 2015). Again, consider a flexible filament of length L , of circular cross section with a diameter d , whose centerline position is described by $\mathbf{r}(s, t)$. The analysis is based on Euler-Bernoulli beam theory and local slender body theory, which exploits

the large aspect ratio of the fiber by using the slenderness $\epsilon = d/L$ as an expansion variable. The combination of equations (1.5) and (1.10) gives:

$$8\pi\mu(\mathbf{r}_t - \mathbf{U}_0(\mathbf{r}(s, t), t)) = c\mathbf{D}(-B\mathbf{r}_{ssss} + (\sigma(s, t)\mathbf{r}_s)_s) \quad (1.13)$$

$$\mathbf{r}_s \cdot \mathbf{r}_{ts} = 0 \quad (1.14)$$

Here B is the bending rigidity, μ is the viscosity of fluid, σ is the tension inside the filament whose role is to ensure the condition of inextensibility. The tensor $\mathbf{D} = (\mathbf{I} + \mathbf{r}_s\mathbf{r}_s^T)$ arises from drag anisotropy, and c is related to the slenderness of the filament, $c = -\ln(\epsilon^2 e)$. The arclength s and time t are independent variables and thus $\partial_{st} = \partial_{ts}$. This property associated to the inextensibility $\mathbf{r}_s \cdot \mathbf{r}_s = 1$ leads to Eqn. (1.14). We nondimensionalize Eqn. (1.13) by scaling spatial variables with L , time by $\dot{\gamma}$, deterministic forces by the typical bending force B/L^2 . The dimensionless equation reads,

$$\mathbf{r}_t = \mathbf{A}\mathbf{r} + \frac{c}{\bar{\mu}}\mathbf{D}(-\mathbf{r}_{ssss} + (\sigma\mathbf{r}_s)_s) \quad (1.15)$$

Here $\bar{\mu} = 8\pi\mu\dot{\gamma}L^4/B$ is the elasto-viscous number, $\mathbf{U}(\mathbf{r}) = \mathbf{A}\mathbf{r}$ is the background shear flow. The boundary conditions are $\mathbf{r}_{ss}|_{s=\pm 1/2} = \mathbf{0}$, $\mathbf{r}_{sss}|_{s=\pm 1/2} = \mathbf{0}$ and $\sigma|_{s=\pm 1/2} = 0$. Combing the Eqn. (1.14) to Eqn. (1.15) yields an elliptic equation for tension σ of the form

$$2\sigma_{ss} - \mathbf{r}_{ss}^T \mathbf{r}_{ss} \sigma = -\frac{\bar{\mu}}{c} \mathbf{r}_s^T \mathbf{A} \mathbf{r}_s - 6\mathbf{r}_{sss}^T \mathbf{r}_{sss} - 7\mathbf{r}_{ss}^T \mathbf{r}_{ssss} \quad (1.16)$$

Here we first consider the case of a straight rod freely moving in 2D flow, the rod can be represented by $\mathbf{r} = s\hat{\mathbf{t}}(t)$, $\hat{\mathbf{t}}(t)$ being the unit orientation vector. Inserting this form into Eqn. (1.16) and applying the boundary conditions of tension $\sigma|_{s=\pm 1/2} = 0$ yields

$$\sigma = -\frac{\bar{\mu}}{4c} (\hat{\mathbf{t}}^T \mathbf{A} \hat{\mathbf{t}}) (s^2 - \frac{1}{4}) \quad (1.17)$$

$$\dot{\hat{\mathbf{t}}} = (\mathbf{I} - \hat{\mathbf{t}}\hat{\mathbf{t}}^T) \mathbf{A} \hat{\mathbf{t}} \quad (1.18)$$

To implement this equations in numerical simulations and observe a deformation it is necessary to add an infinitely small perturbation, \mathbf{w} to the shape: $\mathbf{r} = s\hat{\mathbf{t}} + \mathbf{w}$, with the condition that $|\mathbf{w}| \ll 1$. Inserting this expression into Eqn. (1.15) and multiplying by $\hat{\mathbf{n}}^T (\mathbf{I} - \hat{\mathbf{t}}\hat{\mathbf{t}}^T)$ to get the component in the normal direction, we have:

$$\frac{\bar{\mu}}{c}(\mathbf{w}_t - (\hat{\mathbf{t}}^T \mathbf{A} \hat{\mathbf{t}}) \mathbf{w}) = 2\sigma_s \mathbf{w}_s + \sigma \mathbf{w}_{ss} - \mathbf{w}_{ssss} \quad (1.19)$$

If $\mathbf{A} = \begin{pmatrix} -1 & 0 \\ 0 & 1 \end{pmatrix} \hat{\mathbf{t}}$ represents the background flow, the axis of the rod aligns with the compression part of the flow so that $\hat{\mathbf{t}}^T \mathbf{A} \hat{\mathbf{t}} = -1$. Inserting $\mathbf{w} = e^{\lambda t} f \hat{\mathbf{n}}$ to Eqn. (1.19), we get a time-independent eigenvalue problem.

$$\lambda f = f + s f_s + \frac{1}{4}(s^2 - \frac{1}{4}) f_{ss} - \frac{c}{\bar{\mu}} f_{ssss} \quad (1.20)$$

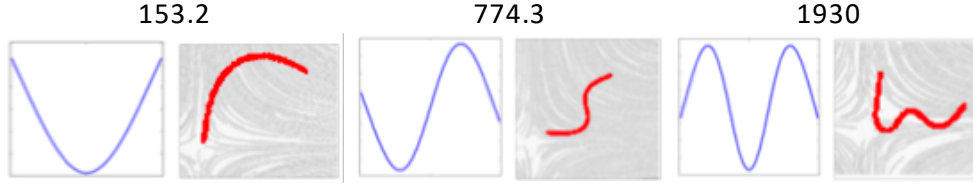


Figure 1.2: Critical values of $\bar{\mu}/c$ and corresponding buckling modes from linear stability analysis and experiments (Quennou et al., 2015).

By increasing $\bar{\mu}/c$ one can find increasing higher order of buckling modes. The first three buckling modes occur at $\bar{\mu}/c = 153.2, 774.3, 1930$ (Becker and Shelley, 2001), and their associated eigenfunctions are showed in Fig. 1.2.

In experiment pure straining flow and reasonably long residence times for a fiber moving in it are difficult to achieve. One possibility is to use the approach of a fiber to a stagnation point. Fiber buckling has been investigated in a macroscopic realization of such a system by (Wandersman et al., 2010) who used centimetric soft elastomer fibers. These fibers move in a viscous 2D cellular flow, an array of hyperbolic stagnation points generated by an array of counter-rotating vortices. Above a critical value of $\tilde{\eta}$, fibers start to buckle (Fig. 1.3A) in the vicinity of the stagnation points. Increasing $\tilde{\eta}$ further induces more complex fiber shapes to develop (Fig. 1.2), which correspond to the shapes predicted by the linear stability analysis.

The influence of Brownian fluctuations on buckling instabilities has also been investigated. (Manikantan and Saintillan, 2015) have shown in numerical simulations that Brownian fluctuations have a minor effect on the buckling instability and mainly broaden the threshold. (Kantsler and Goldstein, 2012) investigated the deformation of a micrometric actin fiber held at a stagnation point in a microfluidic cross-slot device. Their experiments as well as numerical simulations by (Manikantan and Saintillan, 2015) show shapes qualitatively similar to the deterministic predictions, modified however by the Brownian fluctuations (see Figs. 1.3B, C).

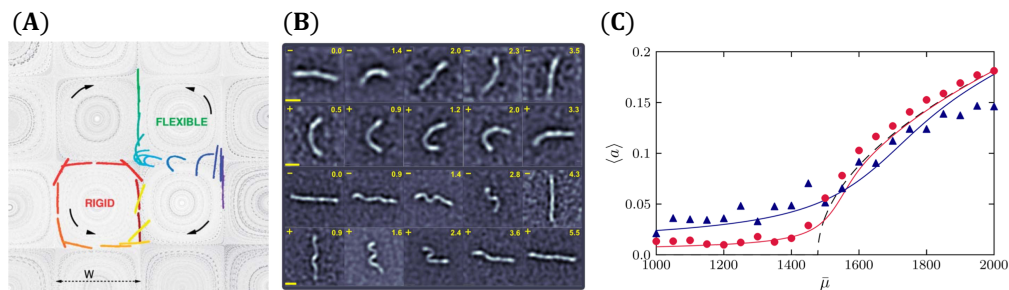


Figure 1.3: **(A)**: Experimental study of the dynamics of flexible fibers in an array of stagnation points (Wandersman et al., 2010). **(B)**: Buckling under compression of fluctuating filaments - actin - held at a stagnation point by microfluidic device (Kantsler and Goldstein, 2012). **(C)**: Amplitude of the first buckling mode of non-Brownian filaments (black dash line) and Brownian filaments (colorful lines and markers) as a function of flow strength in numerical simulations (Manikantan and Saintillan, 2015).

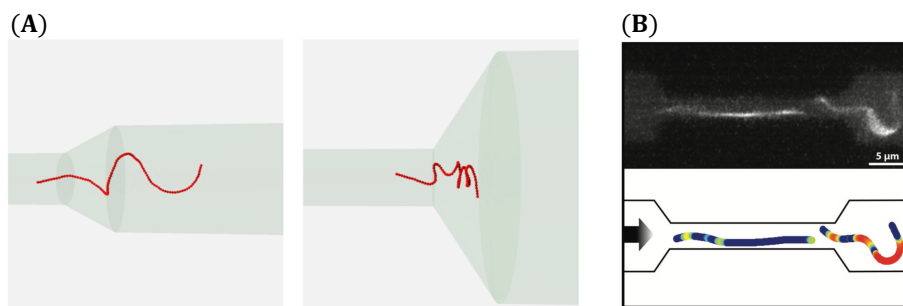


Figure 1.4: **(A)**: Numerical study of flow-induced helical coiling of Brownian filaments in a diverging channel (Chelakkot et al., 2012). **(B)**: Actin filaments dynamics in a confined hyperbolic channel (Strelnikova et al., 2017).

The optimal flow geometry for the investigation of buckling instabilities is a hyperbolic channel, where constant extension rates can be achieved over long residence times. A succession of stretching and coiling has been observed in microchannels with constrictions for actin filaments ((Strelnikova et al., 2017)) and polymeric microfibers (Nunes et al., 2012).

The dynamics of flexible and Brownian filaments in a diverging channel have been numerically studied in the work of (Chelakkot et al., 2012) and an illustration is shown in Fig. 1.4(A). The filaments is not deforming in 2-dimensions but rather form helical structures in 3-D. A similar experimental study shows similar behavior with polymeric microfibers (Mercader et al., 2010).

1.2.2 Dynamics of filaments in shear flow

The classical case of a non-Brownian rigid rod-like particle in shear flow is well understood since the work of Jeffery (Jeffery, 1922), who first described the periodic tumbling of an ellipsoid in shear flow now known as Jeffery orbits.

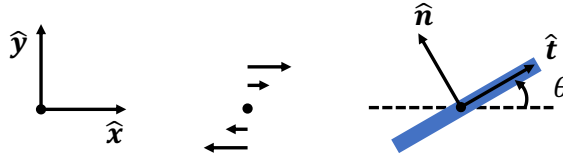


Figure 1.5: Schematic of a straight rod in a simple shear flow

Let's consider the situation depicted in Fig. 1.5, with a rigid rod of length L and circular cross section of constant diameter d . The rod is free to move in a shear flow $\mathbf{U} = (\dot{\gamma}y, 0) = \mathbf{A}\mathbf{r} = \mathbf{\Omega}^\infty + \mathbf{E}^\infty$, \mathbf{r} being the position vector, $\dot{\gamma}$ the shear rate, $\mathbf{\Omega}^\infty = (\mathbf{A} - \mathbf{A}^T)/2$ and $\mathbf{E}^\infty = (\mathbf{A} + \mathbf{A}^T)/2$ being respectively the rotation and strain part of the shear flow. Because of the anisotropy of the particle the aspect ratio $\epsilon = d/L \ll 1$, and the orientational dynamics is determined both by the whole rotational portion of the flow and partly by the strain portion with a fraction $\beta = (\epsilon^2 - 1)/(\epsilon^2 + 1)$ (Guazzelli and Morris, 2011).

$$\frac{d\hat{\mathbf{t}}}{dt} = (\mathbf{\Omega}^\infty + \beta\mathbf{E}^\infty) \cdot \hat{\mathbf{t}} \quad (1.21)$$

Here, $\hat{\mathbf{t}} = [\cos\theta, \sin\theta]$ is the tangent vector of the rod, yields

$$\dot{\theta} = -\frac{\dot{\gamma}}{\epsilon^2 + 1} (\sin^2\theta + \epsilon^2 \cos^2\theta) \quad (1.22)$$

After integration of equation 1.22 with initial condition $\theta(t=0) = 0$ we get

$$\tan\theta = \epsilon \tan\left[-\frac{\dot{\gamma}t}{\epsilon + 1/\epsilon}\right] \quad (1.23)$$

The rod is tumbling periodically with a period $T = 2\pi(\epsilon + 1/\epsilon)/\dot{\gamma}$. When the rod becomes flexible and Brownian, the filament behavior in shear flow is expected to be a combination of deformation and rotation with a non trivial dynamic. In the following, we describe the different works reporting the deformations experienced by the filament while rotating and the impact of flexibility on frequency dynamics.

1.2.2.1 Deformations of elastic fibers in shear flow

Early experiments on the deformation of millimetric elastic fibers under shear, in corn syrup have been done in a Couette cell (Forgacs and Mason, 1959b,a). These authors were the first to address fiber buckling and report on behavior that they called "springy

rotations" ((Forgacs and Mason, 1959b)). For longer fibers "snake" turns have been identified as shown on Fig. 1.6(A) ((Forgacs and Mason, 1959a)). Only later, was the transition to fiber buckling for a fiber in a shear flow clearly identified by a numerical study (see Fig. 1.6(B)) (Becker and Shelley, 2001). Recently, complex dynamics of very long and very flexible filaments have been simulated in shear flow using a diatom chain model (Nguyen and Fauci, 2014).

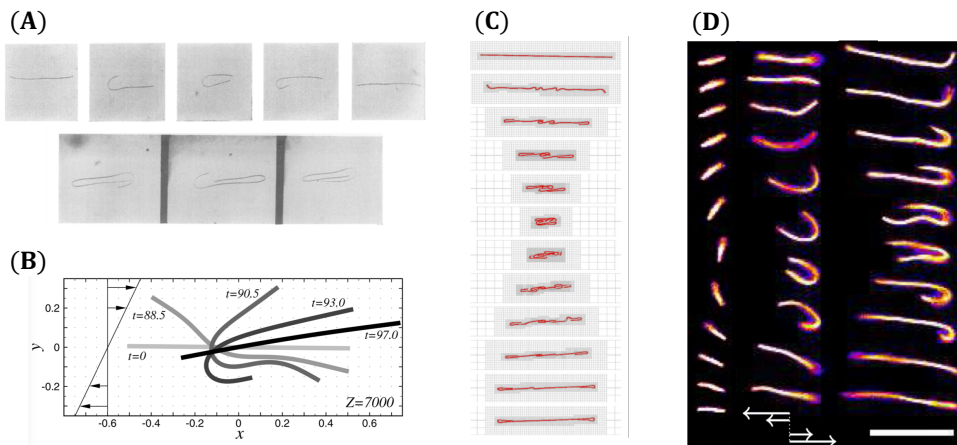


Figure 1.6: (A): Original experiment on the dynamics of millimetric elastic fibers in a Couette cell (Forgacs and Mason, 1959a) . (B): Superimposition of the configurations of flexible filaments in shear flow while rotating obtained from numerical simulations (Becker and Shelley, 2001). (C): Numerical simulations of a long flexible fiber in shear flow (Nguyen and Fauci, 2014). (D): Experimental studies of the dynamics of actin filaments in microfluidic channel (Harasim et al., 2013).

The first transition to buckling takes place at $\tilde{\eta} = 306.4$. This is twice the value $\tilde{\eta}_1 = 153.2$ found for straining flow, as the magnitude of the straining part in shear flow is proportional to only half of the magnitude of the shear flow. Experiments by (Harasim et al., 2013) using actin filaments in microscopic channel flows have investigated in detail the "snake" turn motions and were the first to describe and model this configuration as a tank-trading motion where a narrow bend travels along the filament whose two ends remain aligned with the flow (see Fig. 1.6(D)). Numerous investigations have observed the "snaking" dynamics numerically (Stockie and Green, 1998; Nguyen and Fauci, 2014; Delmotte et al., 2015).

1.2.2.2 Characteristic frequency dynamics

As already explained, a rigid rodlike particle in shear flow follows Jeffery orbits whose tumbling frequency is proportional to the shear rate, $f = \dot{\gamma}/2\pi(\epsilon + 1/\epsilon)$. The more slender the filament, the longer the filament stay aligned with the flow. When the rod orientation fluctuates due to Brownian forces, the tumbling is governed by two distinct phases separated by a critical orientation θ_p as showed in Fig. 1.7(A). In advective phase $\theta > \theta_p$, the dynamics of Brownian rod is still governed by the Jeffery orbit of a non-Brownian

rod. However, in the diffusive phase $\theta < \theta_p$, the dynamics is governed by the rotary diffusion (Kobayashi and Yamamoto, 2010). The peak probability in orientation distribution gives the critical angle θ_p . For a flexible Brownian filament, the advective phase is then determined by the snake motion with significant deformation (Harasim et al., 2013).

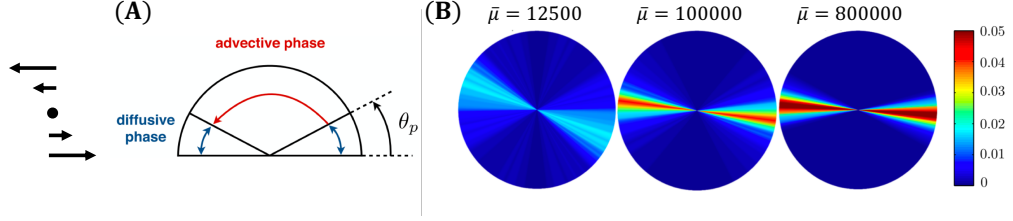


Figure 1.7: (A): Diffusive and advective phases of a tumbling event for a Brownian filament. (B): Polar probability density of the mean orientation of the filament from simulations at three different flow strengths. The shear flow is from right to left in the upper half and the opposite in the lower half (Harishankar, 2009).

The rotation dynamics of long chain polymer like DNA molecules for which $L \gg \ell_p$ have also been intensively studied (Perkins et al., 1997; Aust et al., 2002). Based on the probability distribution function (PDF) of the polymer orientation it is found that there is a shear-preferred peak frequency of tumbling dynamics as showed in Fig. 1.8(A). It has been suggested and experimentally confirmed that the scaled peak frequency $f_c \tau$ of a single Brownian chain with a characteristic relaxation time τ , fluctuating in a shear flow depends on the Weissenberg number, $Wi = \gamma \tau$, with a power law $Wi^{2/3}$, (Schroeder et al., 2005a,b; Gerashchenko and Steinberg, 2006; Winkler, 2006). Recent simulations focused on the other limit, for which $L \lesssim \ell_p$, propose a different scaling behavior $f_c \tau \sim Wi^{3/4}$ (Lang et al., 2014), and agree well with experimental results from (Harasim et al., 2013) (see Fig. 1.8(B)).

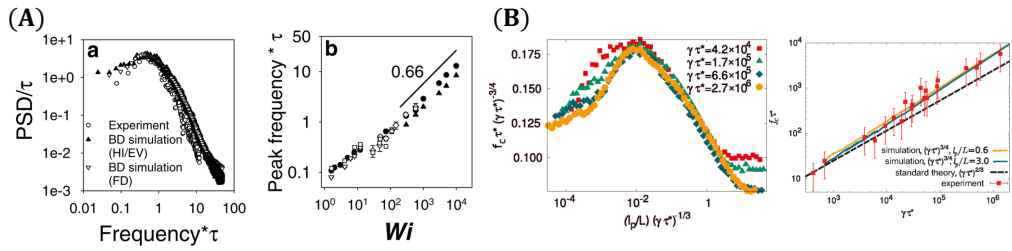


Figure 1.8: (A)-(left): Scaled Power spectral density of polymer orientation angle for DNA in steady shear flow for experiment and simulation at $Wi = 49$. (A)-(right): Scaling of peak frequencies as function of Wi of two DNA molecules with different length (Schroeder et al., 2005a). (B)-(left): Numerical work on dynamics of semiflexible polymer shows The rescaled tumbling frequency $f_c \tau Wi^{-3/4}$ is shown as a function of $(\ell_p/L) Wi^{-1/3}$. (B)-(right): Comparison of simulation results from (Lang et al., 2014) and experimental results from (Harasim et al., 2013) on the frequency scale between $f_c \tau$ and Wi .

1.2.3 From the microscopic to the macroscopic

Because of the presence of the particles and their dynamics in flow described in the previous section, complex suspensions present striking rheological properties from shear thinning and normal stress differences to viscoelastic instabilities (Shaqfeh, 1996; Wierenga and Philipse, 1998; Derakhshandeh et al., 2011; Butler and Snook, 2018) and turbulence (Morozov and van Saarloos, 2007) (see Fig. 1.9). Elucidating the physics behind the dynamics at the particle scale is the key to unraveling the mechanisms for the complex rheological behaviors (Bird et al., 1977). For instance, the studies of the dynamics of single flexible polymer like DNA, in shear flow shows coil-stretch transition cycles with shear rate dependent configuration evolution (Perkins et al., 1997; Smith et al., 1999). This microscopic unsteady dynamics has been related to the shear-dependent viscosity and normal stress differences, leading to rod climbing and Weissenberg effects (Doi and Edwards, 1988; Bird et al., 1977). Hence, after studying the microscopic properties of individual filament, it is essential to explore the bulk properties of suspensions made of those particles.

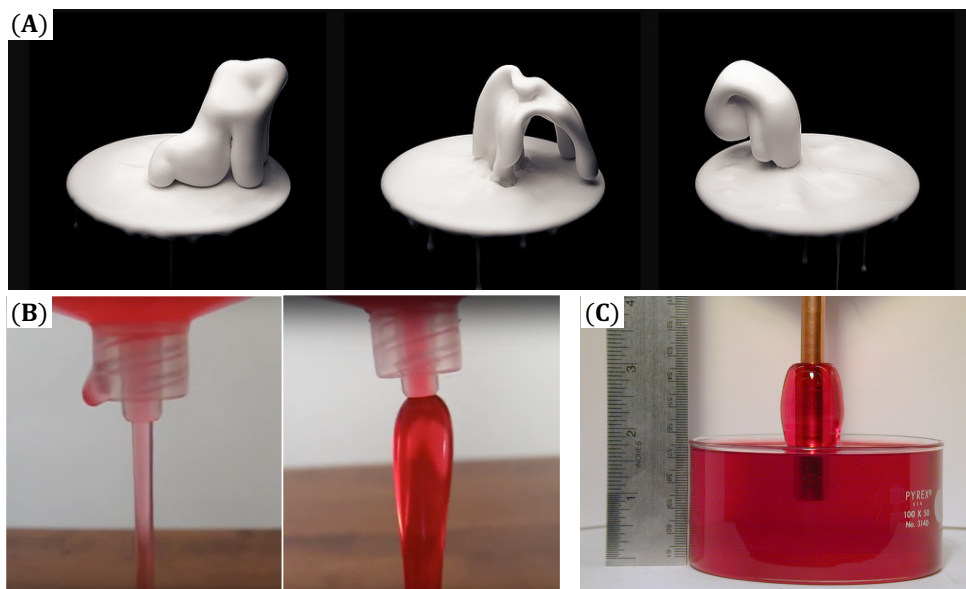


Figure 1.9: The behaviors of Non-Newtonian fluids. (A): Dynamic deformation snapshots of Oobleck (starch suspension) under sine wave (Bond, 2011). (B): Die swell in Newtonian and polymeric liquids (PSIDOT, 2007). (C): Rod climbing effect (McKinley, 2008).

In the dilute suspension regime, the influence of the concentration, aspect ratio, diameter and flexibility of the filaments on the viscous and elastic properties of the non-Brownian elastic fiber suspensions has been experimentally well studied in the work of (Goto et al., 1986). Importantly, this study identifies a sharp transition from zero to positive first normal stress differences beyond a critical shear rate. Numerical simulations then explained that elastic instabilities on the microscopic scale are primarily re-

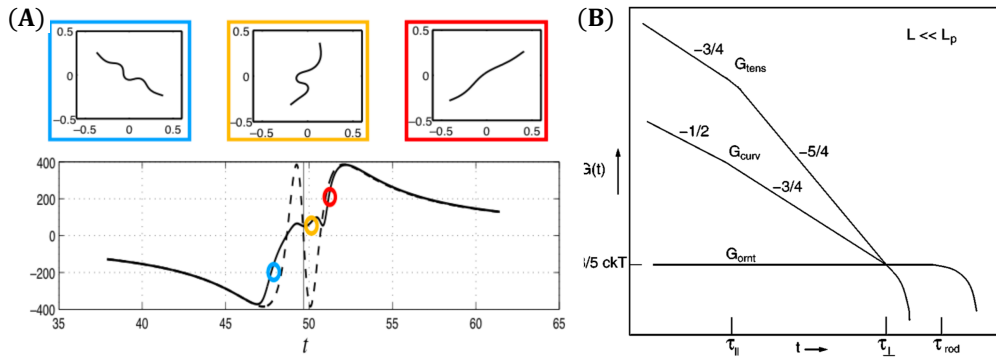


Figure 1.10: **(A)**: first normal stress difference caused by straight filament with dashed line and buckling filaments with solid line (corresponding shapes on the top) (Tornberg and Shelley, 2004). **(B)**: Asymptotic contributions of tensile, bending and thermal forces to shear modulus for semiflexible filaments $L \gg \ell_p$ (Shankar et al., 2002).

responsible for the onset of normal stress differences (Becker and Shelley, 2001; Tornberg and Shelley, 2004). Fig. 1.10(A) shows the comparison of the first normal stress differences between a rigid rod and a buckling flexible filament during one end-over-end rotation and the three corresponding configurations.

As the flexible filaments are Brownian, the effect of Brownian forces on their dynamics is quantified by the ratio between the contour length and the persistence length. When $L \gg \ell_p$, the filaments have coil-like configuration in the fluid. The frictional dissipation is reduced by the alignment of the molecules, leading to a decrease in the viscosity. This mechanism is at the origin of shear-thinning behavior, and sets in once the flow is sufficiently strong to extend the equilibrium conformation of the polymer. The linear viscoelastic behaviors of dilute suspension of polymers $L \leq \ell_p$ have been studied in the work of (Shankar et al., 2002). This work found that the relaxation modulus $\tilde{G}(t)$ in oscillatory shear flow exhibits three different regimes respectively mapped on the fastest tension relaxation timescale τ_{tens} , the intermediate bending relaxation timescale and the slowest rotary diffusion timescale τ_{rot} as showed in Fig. 1.10-(B).

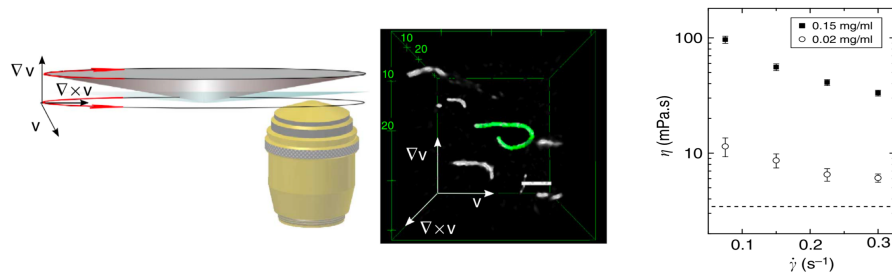


Figure 1.11: Experimental set combining a rheometer and confocal imaging to measure the shear viscosity of semi-dilute of actin filaments and corresponding configurations (Kirchenbuechler et al., 2014).

However, for filaments $L \sim \ell_p$ like actin filaments, the viscous and elastic properties of

their suspension still remains unclear, and the effect of filaments size, aspect ratio and configurational dynamics has not yet been investigated. Actin filaments is a model of semi-flexible polymer with $L \sim \ell_p$ and the properties of actin suspension have only recently been looked at, from dilute regime, where the configurational contribution of individual filament is dominant, to semi-dilute regime (Huang et al., 2012; Kirchenbuechler et al., 2014) where hydrodynamic interactions between filaments needs to be taken into account.

1.3 Conclusion and short description of this manuscript

In this thesis we decided to focus on the case of flexible and Brownian fiber in viscous flows and to investigate the interaction of individual fiber in controlled flow geometry as well as to study the properties of the suspension. We chose actin filaments as our model system: an actin filament is a biological fiber that results from the assembly of a protein, called G-actin, which is very abundant in cells and conserved in evolution. The persistence length of this micrometer-sized filament is comparable to its length and thus it behaves as a semi-flexible polymer, being globally straight but its shape is deformed by bending fluctuations. Details about actin filaments, their properties and how they can be assembled in a controlled way is described in Chapter 2. Actin filaments have been here studied in two different flow geometry addressing different questions. In Chapter 3 the behavior of a filament in pure shear flow is detailed and understood from experiments, theoretical modeling and numerical simulations. Different modes of deformation have been observed when the relative intensity of viscous forces and elastic forces is increased and the transitions between the modes are now fully understood. The Brownian forces have been shown to have no impact on the deformation modes but to broaden the transitions. Optimized hyperbolic geometries have been used in Chapter 4 to follow the behavior of long actin filaments in pure straining flows with long residence time allowing deformations to fully develop. Extensional flow suppresses transverse fluctuations while compressive flows induce buckling which can in certain conditions evolve towards a 3D helical shape. The suspension scale is explained in Chapter 5 which contains both the approach developed to synthesized suspensions with narrow length distributions and the first results obtained on shear-thinning effects. This thesis will be the basis for future works that are summarized in Chapter 6.

References

Aust, C., Hess, S., and Kröger, M. Rotation and deformation of a finitely extendable flexible polymer molecule in a steady shear flow. *Macromolecules*, 35(22):8621–8630, 2002.

- Becker, L. E. and Shelley, M. J. Instability of elastic filaments in shear flow yields first-normal-stress differences. *Physical Review Letters*, 87(19):198301, 2001.
- Bird, R. B., Armstrong, R. C., Hassager, O., and Curtiss, C. F. *Dynamics of polymeric liquids*, volume 1. Wiley New York, 1977.
- Bond, R. Oobleck under sine wave, 2011.
- Butler, J. E. and Snook, B. Microstructural dynamics and rheology of suspensions of rigid fibers. *Annual Review of Fluid Mechanics*, 50:299–318, 2018.
- Chelakkot, R., Winkler, R. G., and Gompper, G. Flow-induced helical coiling of semi-flexible polymers in structured microchannels. *Physical review letters*, 109(17):178101, 2012.
- Delmotte, B., Climent, E., and Plouraboué, F. A general formulation of bead models applied to flexible fibers and active filaments at low reynolds number. *Journal of Computational Physics*, 286:14–37, 2015.
- Derakhshandeh, B., Kerekes, R., Hatzikiriakos, S., and Bennington, C. Rheology of pulp fibre suspensions: A critical review. *Chemical Engineering Science*, 66(15):3460–3470, 2011.
- Doi, M. and Edwards, S. F. *The theory of polymer dynamics*, volume 73. oxford university press, 1988.
- Duprat, C. and Shore, H. A. *Fluid-Structure Interactions in Low-Reynolds-Number Flows*. Royal Society of Chemistry, 2015.
- Forgacs, O. and Mason, S. Particle motions in sheared suspensions: X. orbits of flexible threadlike particles. *Journal of Colloid Science*, 14(5):473–491, 1959a.
- Forgacs, O. and Mason, S. Particle motions in sheared suspensions: IX. spin and deformation of threadlike particles. *Journal of colloid science*, 14(5):457–472, 1959b.
- Gerashchenko, S. and Steinberg, V. Statistics of tumbling of a single polymer molecule in shear flow. *Physical review letters*, 96(3):038304, 2006.
- Goto, S., Nagazono, H., and Kato, H. The flow behavior of fiber suspensions in newtonian fluids and polymer solutions. *Rheologica acta*, 25(2):119–129, 1986.
- Guazzelli, E. and Morris, J. F. *A physical introduction to suspension dynamics*, volume 45. Cambridge University Press, 2011.
- Harasim, M., Wunderlich, B., Peleg, O., Kröger, M., and Bausch, A. R. Direct observation of the dynamics of semiflexible polymers in shear flow. *Physical review letters*, 110(10):108302, 2013.
- Harishankar, M. *Bending, Buckling, Tumbling, Trapping: Viscous Dynamics of Elastic Filaments*. PhD thesis, University of California, San Diego, 2009.

- Huang, C.-C., Gompper, G., and Winkler, R. G. Non-equilibrium relaxation and tumbling times of polymers in semidilute solution. *Journal of Physics: Condensed Matter*, 24(28):284131, 2012.
- Jeffery, G. B. The motion of ellipsoidal particles immersed in a viscous fluid. In *Proceedings of the Royal Society of London A: Mathematical, Physical and Engineering Sciences*, volume 102, pages 161–179. The Royal Society, 1922.
- Johnson, R. E. An improved slender-body theory for stokes flow. *Journal of Fluid Mechanics*, 99(2):411–431, 1980.
- Kantsler, V. and Goldstein, R. E. Fluctuations, dynamics, and the stretch-coil transition of single actin filaments in extensional flows. *Physical review letters*, 108(3):038103, 2012.
- Kirchenbuechler, I., Guu, D., Kurniawan, N. A., Koenderink, G. H., and Lettinga, M. P. Direct visualization of flow-induced conformational transitions of single actin filaments in entangled solutions. *Nature communications*, 5, 2014.
- Kobayashi, H. and Yamamoto, R. Tumbling motion of a single chain in shear flow: a crossover from brownian to non-brownian behavior. *Physical Review E*, 81(4):041807, 2010.
- Lang, P. S., Obermayer, B., and Frey, E. Dynamics of a semiflexible polymer or polymer ring in shear flow. *Physical Review E*, 89(2):022606, 2014.
- Lindner, A., Shelley, M. J., du Roure, O., and Nazockdast, E. Dynamics of flexible fibers in flows. *Annual Review of Fluid Mechanics*, 50(1), 2018.
- Manikantan, H. and Saintillan, D. Subdiffusive transport of fluctuating elastic filaments in cellular flows. *Physics of Fluids*, 25(7):073603, 2013.
- Manikantan, H. and Saintillan, D. Buckling transition of a semiflexible filament in extensional flow. *Physical Review E*, 92(4):041002, 2015.
- McKinley, G. Non-newtonian fluid dynamics research group, 2008.
- Mercader, C., Lucas, A., Derré, A., Zakri, C., Moisan, S., Maugey, M., and Poulin, P. Kinetics of fiber solidification. *Proceedings of the National Academy of Sciences*, 2010.
- Morozov, A. N. and van Saarloos, W. An introductory essay on subcritical instabilities and the transition to turbulence in visco-elastic parallel shear flows. *Phys. Rep.*, 447:112–143, 2007.
- Munk, T., Hallatschek, O., Wiggins, C. H., and Frey, E. Dynamics of semiflexible polymers in a flow field. *Physical Review E*, 74(4):041911, 2006.
- Nguyen, H. and Fauci, L. Hydrodynamics of diatom chains and semiflexible fibres. *Journal of The Royal Society Interface*, 11(96):20140314, 2014.

- Nunes, J. K., Sadlej, K., Tam, J. I., and Stone, H. A. Control of the length of microfibers. *Lab on a Chip*, 12(13):2301–2304, 2012.
- Perkins, T. T., Smith, D. E., and Chu, S. Single polymer dynamics in an elongational flow. *Science*, 276(5321):2016–2021, 1997.
- Powers, T. R. Dynamics of filaments and membranes in a viscous fluid. *Reviews of Modern Physics*, 82(2):1607, 2010.
- PSIDOT. The barus effect, 2007.
- Quennouz, N., Shelley, M., du Roure, O., and Lindner, A. Transport and buckling dynamics of an elastic fibre in a viscous cellular flow. *Journal of Fluid Mechanics*, 769:387–402, 2015.
- Schroeder, C. M., Babcock, H. P., Shaqfeh, E. S., and Chu, S. Observation of polymer conformation hysteresis in extensional flow. *Science*, 301:1515–1519, 2003.
- Schroeder, C. M., Teixeira, R. E., Shaqfeh, E. S., and Chu, S. Characteristic periodic motion of polymers in shear flow. *Physical review letters*, 95(1):018301, 2005a.
- Schroeder, C. M., Teixeira, R. E., Shaqfeh, E. S., and Chu, S. Dynamics of dna in the flow-gradient plane of steady shear flow: Observations and simulations. *Macromolecules*, 38(5):1967–1978, 2005b.
- Shankar, V., Pasquali, M., and Morse, D. C. Theory of linear viscoelasticity of semiflexible rods in dilute solution. *Journal of Rheology*, 46(5):1111–1154, 2002.
- Shaqfeh, E. S. G. Purely elastic instabilities in viscometric flows. *Annu. Rev. Fluid Mech.*, 28:129–185, 1996.
- Smith, D. E., Babcock, H. P., and Chu, S. Single-polymer dynamics in steady shear flow. *Science*, 283(5408):1724–1727, 1999.
- Stockie, J. M. and Green, S. I. Simulating the motion of flexible pulp fibres using the immersed boundary method. *Journal of Computational Physics*, 147(1):147–165, 1998.
- Strelnikova, N., Göllner, M., and Pfohl, T. Direct observation of alternating stretch-coil and coil-stretch transitions of semiflexible polymers in microstructured flow. *Macromolecular Chemistry and Physics*, 218(2):1600474, 2017.
- Tornberg, A.-K. and Shelley, M. J. Simulating the dynamics and interactions of flexible fibers in stokes flows. *Journal of Computational Physics*, 196(1):8–40, 2004.
- Wandersman, E., Quennouz, N., Fermigier, M., Lindner, A., and Du Roure, O. Buckled in translation. *Soft matter*, 6(22):5715–5719, 2010.
- Wierenga, A. M. and Philipse, A. P. Low-shear viscosity of isotropic dispersions of (brownian) rods and fibres; a review of theory and experiments. *Colloids and Surfaces A: Physicochemical and Engineering Aspects*, 137(1-3):355–372, 1998.

- Wiggins, C. H., Rivelino, D., Ott, A., and Goldstein, R. E. Trapping and wiggling: elastohydrodynamics of driven microfilaments. *Biophysical Journal*, 74(2):1043–1060, 1998.
- Winkler, R. G. Semiflexible polymers in shear flow. *Physical review letters*, 97(12):128301, 2006.
- Young, Y.-N. and Shelley, M. J. Stretch-coil transition and transport of fibers in cellular flows. *Physical review letters*, 99(5):058303, 2007.

Chapter 2

Actin as a flexible filament

Contents

2.1 Introduction	22
2.1.1 Actin in cells	22
2.1.2 Actin polymerization	23
2.1.3 Filaments characteristics	24
2.2 Method and materials	24
2.2.1 Polymerization protocol	24
2.2.2 Thin chamber with confinement	25
2.2.3 Image processing and shape reconstruction	26
2.3 Characteristics measurement	27
2.3.1 Brownian fluctuations	27
2.3.2 Persistence length ℓ_p	27
2.4 Summary	29
References	29

2.1 Introduction

2.1.1 Actin in cells

Actin is a major component of the cytoskeleton in most eukaryotic cells (Lodish et al., 1995). It is highly conserved in evolution and participates in many protein-protein interactions (Dominguez and Holmes, 2011). The ability to polymerize from monomeric (G-actin) to filamentous (F-actin) under the control of nucleotide hydrolysis and ions, as well as a large number of actin-binding proteins, make actin a critical player in many important cellular processes. A variety of structures of actin filaments can be observed in cells, like actin cortex, branched networks, arrays of parallel filaments, serving different functions including cell shape and cell motility (Pollard and Borisy, 2003; Pollard and Cooper, 2009), cell division (Garner et al., 2007), cell signaling (Dustin and Cooper, 2000; Calderwood et al., 2000), as well as the establishment and maintenance of cell junctions (Baum and Georgiou, 2011) as showed in Fig. 2.1.

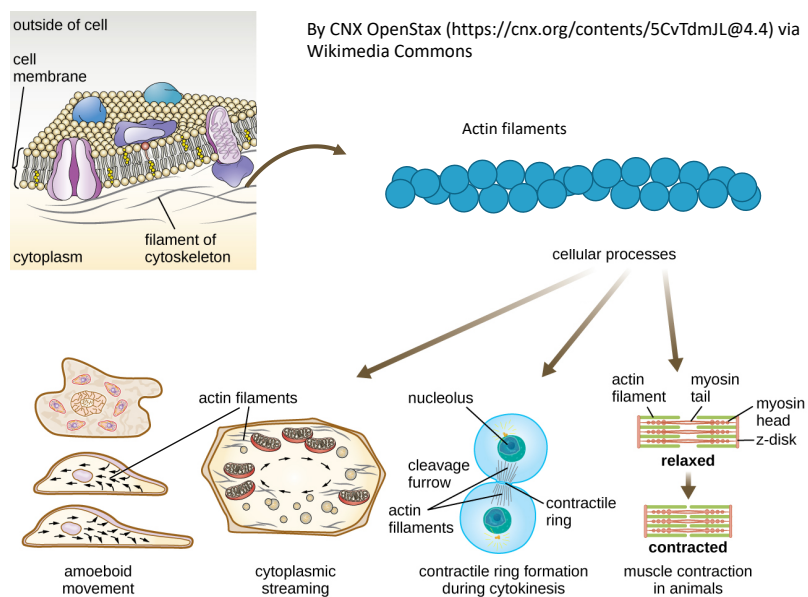


Figure 2.1: Actin filaments related different cellular processes

In those examples, actin filaments generate forces, deformation and movement. In brief, the actin cytoskeleton can generate pushing forces by polymerizing filaments against a surface (of the order of few picoNewtons) and generate contractile force through the actin of actomyosin (also typically in the range of picoNewtons for individual motor). Actin filament networks also undergo and transmit forces and their mechanical properties have been studied as a "passive" material (Kasza et al., 2007).

2.1.2 Actin polymerization

The monomer G-actin, 42 kDa globular protein, a diameter of approximate 5nm , has an nucleotide binding cleft which can host a molecule of ATP or ADP with a divalent cation as showed in Fig. 2.2(A), with an asymmetrical structure of a pointed end (-) and a barbed end (+) (Kabsch et al., 1990). When the concentration of monomers is high enough, at minimum $0.5\mu\text{M}$, random walked actin monomers start to spontaneously form nuclei consisting of 3 monomers called trimers by random collisions as showed in Fig. 2.2(B), in the presence of sufficient strength of ionic, typically tens of mM of KCl. In the pool of nucleotides in solution, G-actin can rapidly bind ATP with a high favor. The filaments begin to polymerize from the trimer at both sides with barbed ends pointing the same direction, giving to polymerized actin filaments a "polarity" (Otterbein et al., 2001), forming a right-handed double helical structure with a diameter around 8nm (Holmes et al., 1990; Pollard, 1986) as showed in Fig. 2.2(C).

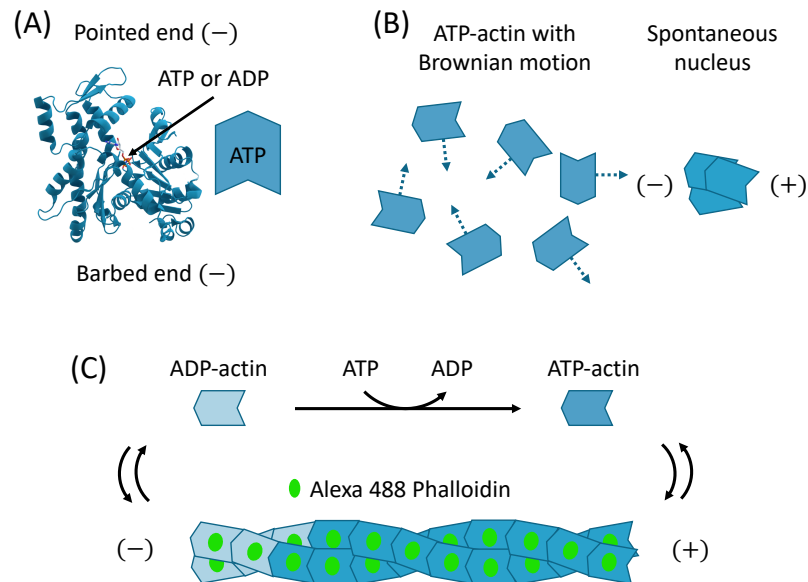


Figure 2.2: Polymerization of actin monomers into filaments: (A) Crystal structure of actin monomer (Otterbein et al., 2001). (B) Formation of spontaneous nucleus. (C) Polymerization of filaments with helical structure in the presence of Alexa 488 Phalloidin.

The growth rates at both ends depend on the concentration of monomers, the more concentrated actin monomers the faster they polymerize, which means the polymerization can be stopped by diluting solution below a certain concentration. In the filament, the subunit can also dissociate from filaments at both ends, faster at pointed end and slower at barbed end due to ATP hydrolysis to ADP. Fluorescent Phalloidin (Alexa 488 Invitrogen) is added here to visualize filaments and reduces the dissociation at both ends to cease, at the same time Phalloidin also reduces the association rate at the barbed end by about 50% (Sampath and Pollard, 1991). The concentration of Phalloidin should be maintained above 17nM to ensure Phalloidin can be replaced when it dissociation from

filaments(De La Cruz and Pollard, 1994). Since the polymerization starts from spontaneous nucleus sooner or later, when the polymerization stops at the same time, there are filaments with different lengths from few microns to hundreds of microns in solution. Over the pH range of 6.6 ~ 8.3, the pH has very little effect on the association rate at both ends (Sampath and Pollard, 1991). In the solution, DTT, DABCO and ascorbic acid can be added to avoid photobleaching and photodamage.

2.1.3 Filaments characteristics

Under thermal forces, individual actin filaments as a biopolymer exhibit significant thermal fluctuations around its intrinsic straight configuration, instead of completely straight or random coiled state. This gives a way to quantify the bending stiffness of actin filaments B as $B = \ell_p \times k_B T$ (Landau et al., 1980). Here $k_B = 1.38 \times 10^{-23} J \cdot K^{-1}$ is Boltzmann constant, T is Kelvin temperature. ℓ_p is the persistence length that is defined as the distance over which the tangential vectors start to become uncorrelated. Let us define the angle $\theta(s)$ is the unit tangent vector at arc length s along the polymer. The thermal bending of flexible polymers in bulk with three-dimensional motion results in the mean dot product (the cosine correlation function) between unit tangent vectors over certain distance falls off exponentially with the distance given by,

$$\overline{\langle \cos[\mathbf{t}_3(s+l) - \mathbf{t}_3(s)] \rangle} = \exp(-l/\ell_p) \quad (2.1)$$

where $\mathbf{t}_3(s)$ is the three-dimensional tangential vectors at arc length s (Landau et al., 1980). Informally, for pieces of the polymer that are much shorter than its persistence length, the molecule behaves rather like a rigid rod, for pieces of the polymer that are much longer than its persistence length, the properties can only be described statistically, while for pieces in between, they are regarded as semiflexible polymer where the polymer's length is comparable to its persistence length.

2.2 Method and materials

2.2.1 Polymerization protocol

The protocol for actin filament polymerization is well controlled and reproducible. Concentrated G-actin suspended in G-buffer are obtained from rabbit muscle and purified as protocol(Spudich and Watt, 1971), which are provided by Guillaume Romet-Lemonne and Antoine Jégou's research group in regulation of actin assembly dynamics at Institut Jacques Monod. Concentrated G-actin are placed into F-Buffer polymerization at a

final concentration of $1 \sim 5 \mu\text{M}$. At the same time, Alexa488 Fluorescent Phalloidin (Invitrogen) in two or three times molarity as G-actin is added to stabilize and visualize filaments (Dancker et al., 1975), ensuring that each monomer could be labelled. After one hour of polymerization in dark at room temperature 20°C , concentrated F-actin is stored at 4°C and in dark environment for experiments in the following week. For each experiment, concentrated filament suspension is diluted in F-buffer. To observe Brownian fluctuations of individual filaments, filament suspension is diluted to a final monomer concentration of $20 \sim 50 \text{ nM}$ to avoid interaction between filaments. Table 2.1 shows the compositions of the different buffers.

	G-buffer	F-buffer polymerization	F-buffer dilution
Tris-HCl PH=7.8	10mM	10mM	10mM
ATP	0.1mM	0.2mM	0.2mM
CaCl ₂	0.2mM	0.2mM	0.2mM
DTT	1mM	1mM	10mM
NaN ₃	0.01%		
MgCl ₂		1mM	1mM
KCl		100mM	100mM
EGTA		0.2mM	0.2mM
DABCO		0.15mM	0.15mM
Ascorbic acid			1mM
Sucrose			0~700(g/L)

Table 2.1: The compositions of different buffers

Sucrose concentration (g/L)	Rheometer 1st (mPa·s)	Rheometer 2nd (mPa·s)
400	4.5	4.8
500	7.3	7.8
600	12	15
700	28	30

Table 2.2: Viscosity of F-buffer varing with sucrose concentration

Sucrose with different concentrations are added to change the viscosity of the solutions. The viscosity of F-buffer dilution is measured twice by rheometer Anton Paar MCR 501 at 20°C with cone-plane 60-1 geometry as showed in table 2.2.

2.2.2 Thin chamber with confinement

Here we present the device to investigate the characteristics of actin filament, including the Brownian fluctuations of freely individual filaments, its bending rigidity quantified by its persistence length ℓ_p as $B = \ell_p \times k_B T$. To observe filaments, we need to keep filaments in the focal plane by constraining the movements and deformations of filaments in a thin

chamber with a height of $2\mu\text{m}$. We use a thick slide and a thin cover slip to build this quasi 2D chamber as showed in Fig. 2.3. Both slide and cover slip are immersed in 1% BSA for 10 minutes to avoid the sticking of the filaments to glass.

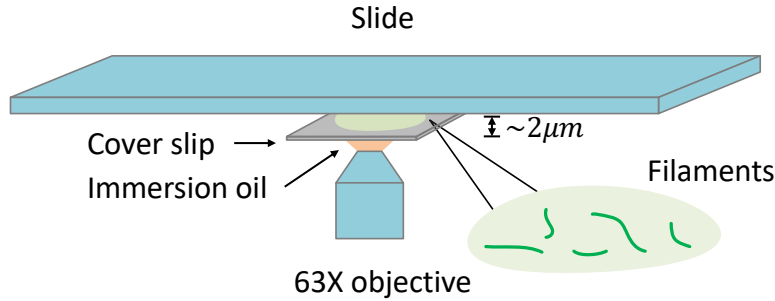


Figure 2.3: 2D confinement to observe the fluctuations of filaments in solution

Since the viscous drag force acting on filaments with a circular section of diameter d near a surface is proportional to $\ln(4h/d)^{-1}$ (Brennen and Winet, 1977), h is the height of the chamber. we add some rigid particles of a diameter of $2\mu\text{m}$ to keep the chamber a constant height.

2.2.3 Image processing and shape reconstruction

Images are captured by camera (HAMAMATSU ORCA flash 4.0LT) with an exposure time $\Delta t = 50\text{ms}$, and processed by Image J through Gaussian blur, threshold, noise reduction if it is necessary, skeletonize and reconstruct. Fig. 2.4 shows an example of image processing procedure from raw images to final reconstructed images of different configurations of filaments. Since filaments perform thermal bending during recording, several different spatial Fourier modes configurations are selected (m represents the mode number).

In the process, Gaussian blur is used first to reduce image noise by convolving each pixel of the image with a Gaussian function over a circular region of a given radius. In our processing, the value of radius varying from 0.5 to 3 depending on image quality. Afterwards, threshold and skeletonize function is used to obtain the centreline of filaments. At last, by extracting a set of filament coordinates from skeletonized images, a self-written MATLAB code are used to construct the centreline of filaments with sequential points along arc length s .

The lab written MATLAB code is compiled through the following steps:

1. Calculate the center of mass (x_c, y_c) ;
2. Search the farthest point from (x_c, y_c) , regarded as one of the ends (x_0, y_0) ;

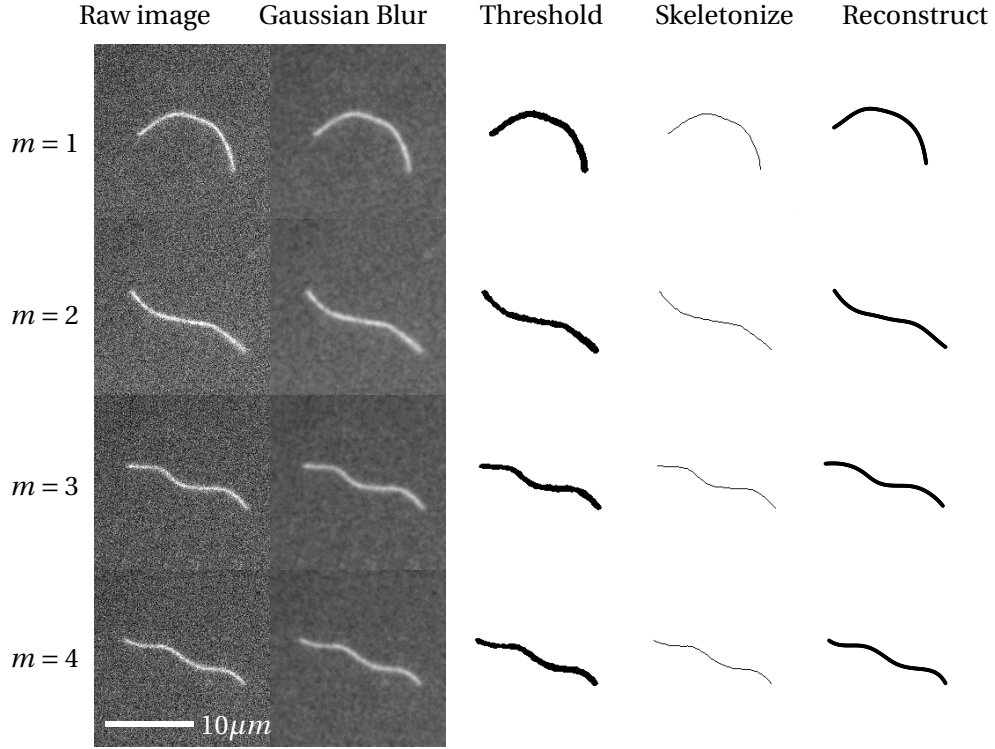


Figure 2.4: Image processing procedure of first four modes configurations

3. Starting from $(x_i, y_i)_{i=0}$, look for the nearest point from (x_i, y_i) as the next sequential point (x_{i+1}, y_{i+1}) with a radius of $1 \sim 2 \mu\text{m}$ until the whole filament has been described;
4. Based on those sequential points, B-spline function is used to get regularly spacial coordinates along an arc length interval $\Delta s = 0.5 \mu\text{m}$

2.3 Characteristics measurement

2.3.1 Brownian fluctuations

Here we present the investigation and analysis of Brownian fluctuations of freely individual actin filaments. Fig. 2.5 shows the configurations of filaments of length of $15 \mu\text{m}$ fluctuating in viscous buffer $\mu = 7 \text{ mPa}\cdot\text{s}$ within 20 s.

2.3.2 Persistence length ℓ_p

Based on the configurations of filaments with Brownian fluctuations, the persistence length can be measured at room temperature 20°C . Note that when the filament fluctuations occur in 2D, as it is the case in the experiments described here, the decay length is doubled (Gittes et al., 1993; Ott et al., 1993),

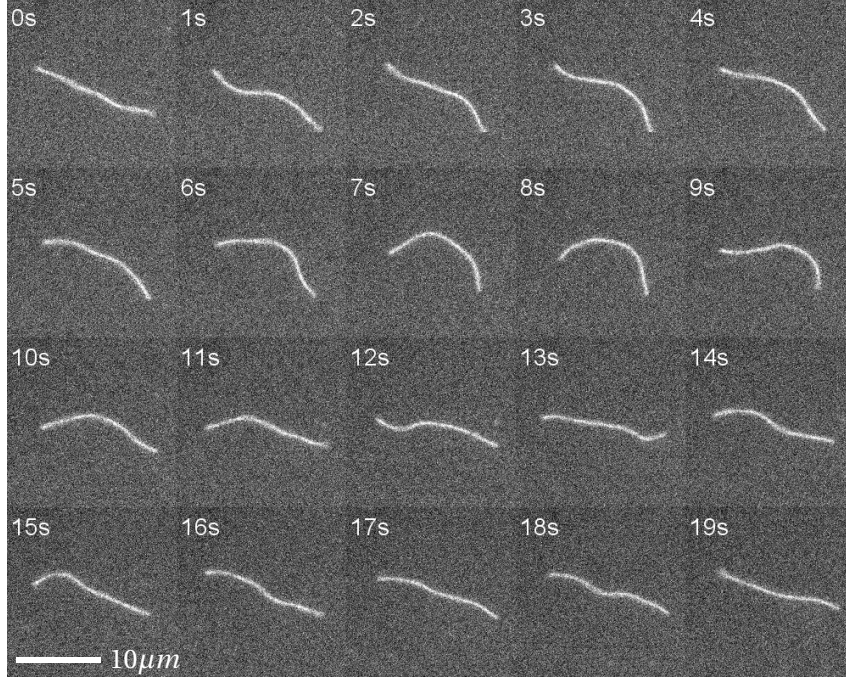


Figure 2.5: Brownian fluctuation of actin filaments in solution

$$\overline{\langle \cos[\mathbf{t}(s+l) - \mathbf{t}(s)] \rangle} = \exp(-l/2\ell_p) \quad (2.2)$$

where $\mathbf{t}(s)$ is the two-dimensional tangential vector at arc length s . The bar in Eqn. (2.2) denotes the spatial averaging within the same filament whereas the brackets denote the thermal averaging which includes many conformations of filaments. The discrete form of Eqn. (2.2) is give by,

$$\frac{1}{Num} \frac{1}{n} \sum_{j=1}^{Num} \sum_{i=1}^n \cos[\theta_j(s_i+l) - \theta_j(s_i)] = \exp(-l/2\ell_p) \quad (2.3)$$

where θ is the angle of tangential vector. Num is the number of the filaments considered, and n is the number of segments, l being the distance along the filament on which the correlation function is calculated.

Fig. 2.6(left) shows the cosine correlation function calculated according to Eqn. (2.3) in the case of $\mu = 1mP \cdot s$. We also measured the persistence length ℓ_p of filaments in different viscosities by varying the concentration of sucrose in the buffer as showed in Fig. 2.6(right). We derive a viscosity independent persistence length $\ell_p = 17 \pm 1 \mu m$ of Phalloidin stabilized actin filaments, which is in agreement with previous study(Gittes et al., 1993; Ott et al., 1993).

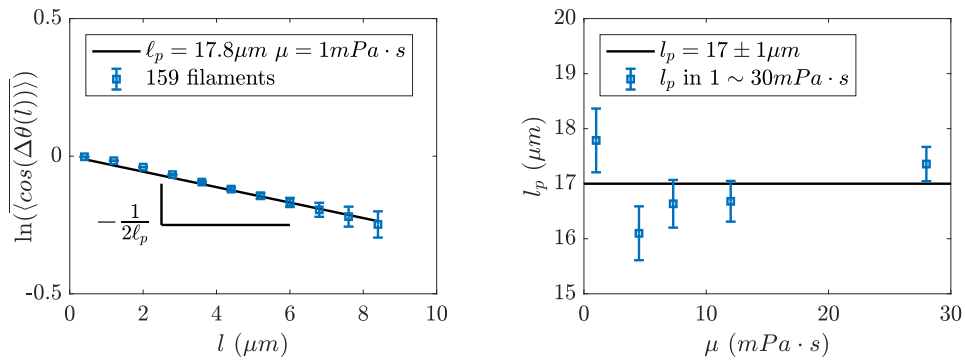


Figure 2.6: (left): Cosine correlation function of tangential vectors over a distance l . (right): Persistence length ℓ_p measured in different viscosities

2.4 Summary

In this chapter, we briefly introduced the functions of actin filaments in cells, the polymerization process of actin filaments with a controlled and reproducible protocol. Through confining the movements of filaments in a quasi two dimensional chamber, we observed the Brownian fluctuations of actin filaments in solutions with different viscosities by adding sucrose with different concentrations. We analyzed the configurations of fluctuating filaments through image processing and a lab written MATLAB code. We calculate the persistence length ℓ_p through the cosine correlation function of tangential vectors of different configurations. We find, as we expected, $\ell_p = 17 \pm 1 \mu\text{m}$, which is independent of the solutions viscosities as well as the concentration of sucrose in solution.

References

- Baum, B. and Georgiou, M. Dynamics of adherens junctions in epithelial establishment, maintenance, and remodeling. *The Journal of cell biology*, 192(6):907–917, 2011.
- Brennen, C. and Winet, H. Fluid mechanics of propulsion by cilia and flagella. *Annual Review of Fluid Mechanics*, 9(1):339–398, 1977.
- Calderwood, D. A., Shattil, S. J., and Ginsberg, M. H. Integrins and actin filaments: reciprocal regulation of cell adhesion and signaling. *Journal of Biological Chemistry*, 275(30):22607–22610, 2000.
- Dancker, P., Löw, I., Hasselbach, W., and Wieland, T. Interaction of actin with phalloidin: Polymerization and stabilization of f-actin. *Biochimica et Biophysica Acta (BBA)-Protein Structure*, 400(2):407–414, 1975.
- De La Cruz, E. M. and Pollard, T. D. Transient kinetic analysis of rhodamine phalloidin binding to actin filaments. *Biochemistry*, 33(48):14387–14392, 1994.

- Dominguez, R. and Holmes, K. C. Actin structure and function. 2011.
- Dustin, M. L. and Cooper, J. A. The immunological synapse and the actin cytoskeleton: molecular hardware for t cell signaling. *Nature immunology*, 1(1):23, 2000.
- Garner, E. C., Campbell, C. S., Weibel, D. B., and Mullins, R. D. Reconstitution of dna segregation driven by assembly of a prokaryotic actin homolog. *Science*, 315(5816): 1270–1274, 2007.
- Gittes, F., Mickey, B., Nettleton, J., and Howard, J. Flexural rigidity of microtubules and actin filaments measured from thermal fluctuations in shape. *Journal of Cell biology*, 120:923–923, 1993.
- Holmes, K. C., Popp, D., Gebhard, W., and Kabsch, W. Atomic model of the actin filament. *Nature*, 347(6288):44, 1990.
- Kabsch, W., Mannherz, H. G., Suck, D., Pai, E. F., and Holmes, K. C. Atomic structure of the actin: Dnase i complex. *Nature*, 347(6288):37, 1990.
- Kasza, K. E., Rowat, A. C., Liu, J., Angelini, T. E., Brangwynne, C. P., Koenderink, G. H., and Weitz, D. A. The cell as a material. *Current opinion in cell biology*, 19(1):101–107, 2007.
- Landau, L. D., Lifshitz, E. M., and Pitaevskii, L. Statistical physics, part i, 1980.
- Lodish, H., Berk, A., Zipursky, S. L., Matsudaira, P., Baltimore, D., Darnell, J., et al. *Molecular cell biology*, volume 3. WH Freeman New York, 1995.
- Ott, A., Magnasco, M., Simon, A., and Libchaber, A. Measurement of the persistence length of polymerized actin using fluorescence microscopy. *Physical Review E*, 48(3): R1642, 1993.
- Otterbein, L. R., Graceffa, P., and Dominguez, R. The crystal structure of uncomplexed actin in the adp state. *Science*, 293(5530):708–711, 2001.
- Pollard, T. D. Rate constants for the reactions of atp-and adp-actin with the ends of actin filaments. *The Journal of cell biology*, 103(6):2747–2754, 1986.
- Pollard, T. D. and Borisy, G. G. Cellular motility driven by assembly and disassembly of actin filaments. *Cell*, 112(4):453–465, 2003.
- Pollard, T. D. and Cooper, J. A. Actin, a central player in cell shape and movement. *Science*, 326(5957):1208–1212, 2009.
- Sampath, P. and Pollard, T. D. Effects of cytochalasin, phalloidin and ph on the elongation of actin filaments. *Biochemistry*, 30(7):1973–1980, 1991.
- Spudich, J. A. and Watt, S. The regulation of rabbit skeletal muscle contraction i. biochemical studies of the interaction of the tropomyosin-troponin complex with actin and the proteolytic fragments of myosin. *Journal of Biological Chemistry*, 246(15): 4866–4871, 1971.

Chapter 3

The dynamics of flexible filaments in shear flow

Contents

3.1 Introduction	32
3.2 Method and materials	32
3.2.1 Experimental setup	32
3.2.2 Microfluidic geometry	33
3.2.3 z correction program	35
3.2.4 Quantitative parameters	36
3.3 Numerical simulations	38
3.4 Morphological dynamics in shear flow	40
3.4.1 Rod-like tumbling	41
3.4.2 C shape buckling with global rotation	42
3.4.3 Snake turn dynamics	43
3.4.3.1 U snake turn	43
3.4.3.2 S snake turn	44
3.4.4 Complex dynamics	45
3.5 Transitions between different dynamics	46
3.5.1 Order parameters and phase diagram	46
3.5.2 The transition from C buckling to U snake turn	50
3.5.2.1 Dynamics model of initial state of U snake turn	50
3.5.2.2 Parameters and comparison between experiments, numerics and J shape model	55
3.6 Frequency dynamics in shear flow	56
3.7 Summary	58
References	59

3.1 Introduction

The classical case of a rigid rod-like particle in a shear flow is well understood since the work of Jeffery (Jeffery, 1922), who first described the periodic tumbling now known as Jeffery orbits occurring in shear flow. When flexibility becomes significant, viscous stresses applied onto the filament can overcome bending resistance and lead to structural instabilities reminiscent of Euler buckling of elastic beams (Young and Shelley, 2007; Kantsler and Goldstein, 2012). In shear flow, the combination of rotation and deformation leads to particularly rich dynamics (Forgacs and Mason, 1959; Nguyen and Fauci, 2014), which have yet to be fully characterized and understood.

Since $L \sim \ell_p$, actin filaments are a model system to study the effect of flexibility and Brownian fluctuations on the dynamics of filaments (Harasim et al., 2013; Kantsler and Goldstein, 2012), in terms of deformation and rotation. Here, bending energy and thermal fluctuations are of comparable magnitudes, while the energy associated with stretching is typically much larger due to the small diameter of the molecular filaments (Linder and Shelley, 2016). This distinguishes these filaments from long entropy-dominated polymers such as DNA in which chain bending plays little role. Here it is the subtle interplay of bending forces, thermal fluctuations and internal tension under viscous loading that instead dictates the dynamics and is known to result in a variety of complex phenomena under flow (Munk et al., 2006; Guglielmini et al., 2012; Manikantan and Saintillan, 2013, 2015).

In this chapter, we elucidate these dynamics in a simple shear flow by combining model experiments using actin filaments, numerical simulations and theoretical modeling. We combine fluorescent labeling techniques, microfluidic flow devices and an automated-stage microscopy apparatus to systematically identify deformation modes and conformational transitions. Our experimental results are compared to Brownian dynamics simulations that describe actin filaments as thermal inextensible Euler-Bernoulli beams whose hydrodynamics follow slender body theory (Tornberg and Shelley, 2004) and theoretical models. This work has been accepted for publication in Proceedings of the National Academy of Science (Liu et al., 2018).

3.2 Method and materials

3.2.1 Experimental setup

Fig. 3.1 displays the overall arrangement of all experimental devices, including a Zeiss microscope (Observer A1), a motorized stage (ASI MS-2000) with a $500\ \mu\text{m}$ piezo control along z and a Cellix ExiGo low pressure syringe pump. Through a combination of a specifically chosen microfluidic geometry, a high magnification objective (Zeiss Apoc-

hromat 63X/1.2NA with a long working distance $280\ \mu\text{m}$) and a motorized stage, we could directly observe the dynamics of filaments during their transport in flow. Images are captured by a digital camera (HAMAMATSU ORCA flash 4.0LT) with a frequency of 10Hz and an exposure time $\Delta t = 65\ \text{ms}$. A UV light filter cube No.44 is used to excite Alexa 488 labeled filaments.

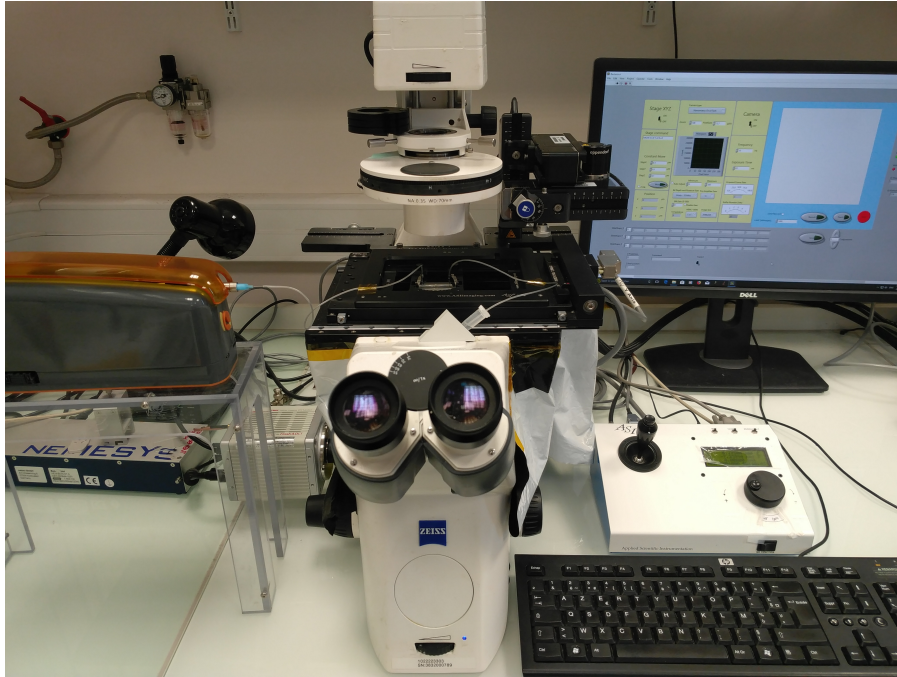


Figure 3.1: A picture of the experimental setup.

Filament suspensions used for the experiments have a final monomer concentration of $0.1\ \text{nM}$ to avoid interaction between filaments. $45.5\%(\text{w/v})$ sucrose is added to match the refractive index of the PDMS channel ($n=1.41$). The viscosity of the suspension is $5.6\ \text{mPa}\cdot\text{s}$ at 20°C , measured on a rheometer (Anton Paar MCR 501). The Phalloidin-stabilized filaments we considered here have a contour length L varying between $(4, 50)\ \mu\text{m}$ and a diameter of $d \sim 8\ \text{nm}$. By analysing the fluctuating shapes of the filaments, we measured the persistence length, as shown in chapter 2.3.2, to be $\ell_p = 17 \pm 1\ \mu\text{m}$ (Gittes et al., 1993), independent of the solvent viscosity.

3.2.2 Microfluidic geometry

The microfluidic channel used in experiments is a vertical Hele-Shaw cell in which we create a horizontal flow as illustrated in Fig. 3.2. In this figure, the light grey region is the chamber of the channel, the dark grey area indicates the focal plane, and the blue region is the motorized stage. The channel is designed to have a height $H = 500\ \mu\text{m}$, a width $W = 150\ \mu\text{m}$ and a length $L_{\text{channel}} = 30\ \text{mm}$, which is based on the factors discussed below.

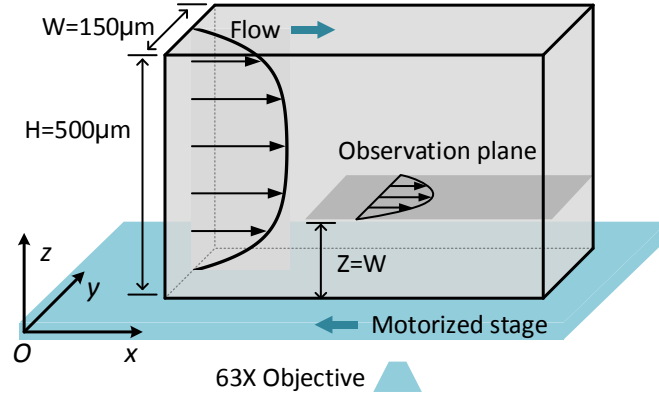


Figure 3.2: Sketch of the experimental device.

- The aspect ratio between height and width should be sufficiently large to provide a velocity plateau in the z direction near the channel centre for $z \gtrsim W$. In this region, the flow is nearly two-dimensional and the filaments are mainly deformed by the shear rate $\dot{\gamma}_y$ in the xOy plane.
- The width of the channel is much larger than the typical transverse length scale Δy of the deformed filaments, so that the shear can be approximated as constant over that length scale.
- To avoid wall-interaction effects and artifacts due to the change in sign of $\dot{\gamma}_y$ near the centreline as well as to satisfy $\dot{\gamma}_y \gg \dot{\gamma}_z$, we focus on trajectories of filaments transported in the blue region in Fig. 3.3.

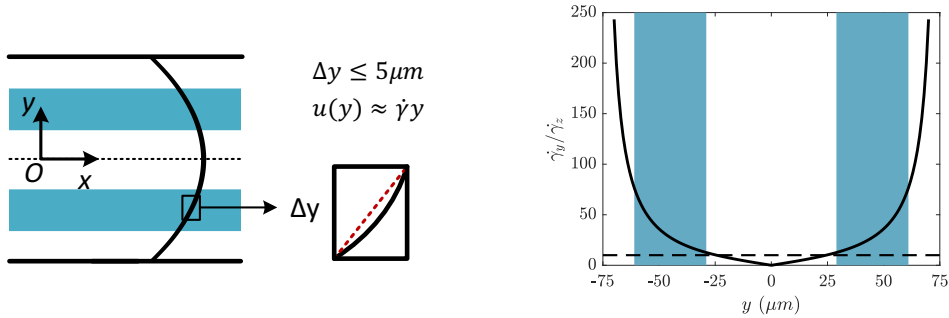


Figure 3.3: (Left) Linear approximation of the flow velocity in the observation plane. (Right) Solid line: The ratio of shear rates at $z = 150 \mu\text{m}$. Dashed line: $\dot{\gamma}_y/\dot{\gamma}_z = 10$.

We impose flow rates Q in the range $5 \sim 10 \text{ nl/s}$, so that filaments have average velocities $U_x \in 20 \sim 150 \mu\text{m/s}$ in the observation plane $z = 150 \mu\text{m}$. These velocities provide shear rates in the range of $0.5 \sim 10 \text{ s}^{-1}$ in the observation plane. The resulting velocity profile measured by particle tracking is compared to theoretical predictions as Eqn. (3.1) (White and Corfield, 2006).

$$\begin{aligned}
U_x(y, z) &= \frac{16a^2}{\mu\pi^3} \left(-\frac{dP}{dx} \right) \sum_{i=1,3,5,\dots}^{\infty} (-1)^{(i-1)/2} \left[1 - \frac{\cosh(i\pi y/2a)}{\cosh(i\pi b/2a)} \right] \times \frac{\cos(i\pi z/2a)}{i^3} \\
Q &= \frac{4ba^3}{3\mu} \left(-\frac{dP}{dx} \right) \left[1 - \frac{192a}{\pi^5 b} \sum_{i=1,3,5,\dots}^{\infty} \frac{\tanh(i\pi b/2a)}{i^5} \right] \\
-a \leq z \leq a, \quad -b \leq y \leq b
\end{aligned} \tag{3.1}$$

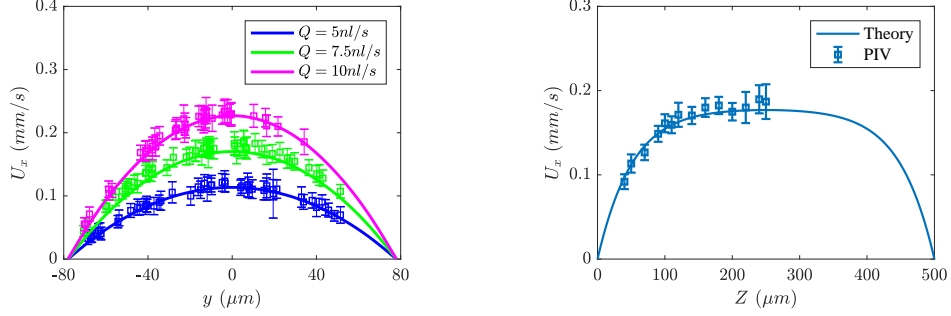


Figure 3.4: (Left) Velocity profiles of different flow rates in observation plane xOy . (Right) Velocity profile along z in the centre for a flow rate $Q = 7.5 \text{ nl/s}$. Solid lines of different colors are theoretical velocities and markers are the corresponding experimental measurements obtained through PIV.

Good agreement between particle velocity and theoretical flow velocity proves the stability of the flow imposed by our syringe pump and the precision of the z position measurement. Figure 3.4 shows velocity profiles in the observation plane xOy ($z = 150 \mu\text{m}$) for different flow rates (a) and the velocity profile in the centre xOz plane respectively, compared to PIV measurements. We estimate the corresponding Reynolds number of the filaments in flow to be of the order $\text{Re} \sim 10^{-4}$.

3.2.3 z correction program

The microchannel is sealed with a thin slide of size $40 \text{ mm} \times 24 \text{ mm}$ with a thickness of 0.17 mm . Since the slide is thin, over a distance of the length of channel 30 mm , the slide is not perfectly flat and usually bends slightly. The bending of the slide can be caused by both the deformation of the PDMS channel while its bounding to the slide and the pulling force exerted by the oil immersion objective. This bending effect causes typical variations of $50 \sim 80 \mu\text{m}$ of the z position of the channel over the whole channel length. The camera combined with the $63\times$ objective provides a visual field of $200 \mu\text{m} \times 200 \mu\text{m}$ size. Filaments have a mean velocity $\sim 100 \mu\text{m}$. In order to directly observe the dynamics of filaments during their transport, we need to follow the filaments during transport in the channel. Due to the influence of bending, when we track the filaments, we will lose filaments from the focal plane because the depth of field of the objective is very small, about $1 \sim 2 \mu\text{m}$. To solve this problem, we programmed the motorized stage to adjust

the z displacement automatically following the bent shape of the slide depending on the current position. To do so, we built a z displacement correction Labview program to keep filaments in the focal plane.

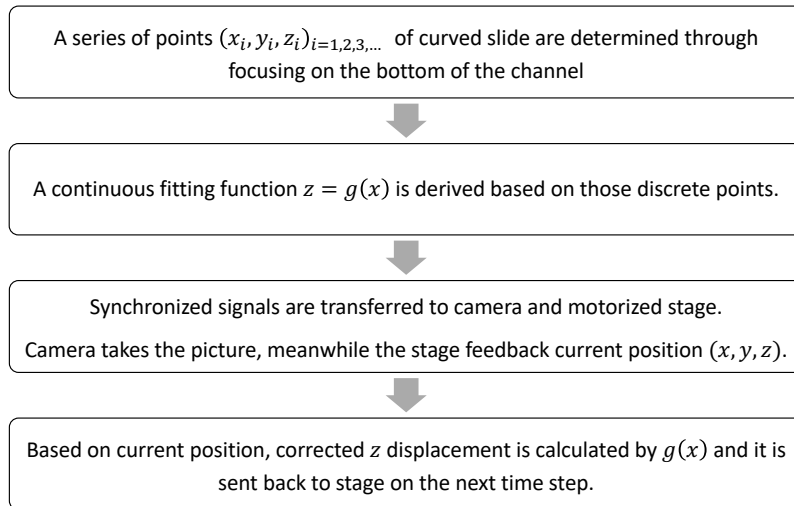


Figure 3.5: Operation flow chart of Labview program.

Figure 3.5 is the operation flow chart of the Labview program. After setting the origin of the coordinates, a continuous fitting function of the bent slide is obtained from a series of discrete points measured by focusing on the bottom of the channel while moving along the channel. An external trigger is used to send synchronized signals with commands to camera and stage. As soon as the signal arrives, the camera will take pictures, meanwhile the stage will send back the current position. The command sent to the stage corrects the z displacement, calculated based on the x position derived from the previous time step. The calibration of the z displacement needs to be done each time a channel is mounted onto the stage. As the bend of the channel is calibrated through focusing on the bottom of the channel, a vector of (x_i, y_i, z_i) needs to be filled in the red frame in Fig. 3.6, which is the interface of the Labview program. The correction of the z displacement only works when the "Track Z" switch is on. A correction of the y displacement could also work through the same way if necessary, but has not been used here.

3.2.4 Quantitative parameters

We characterize the temporal evolution of the filament shapes quantitatively with selected parameters. In order to describe the overall shape and orientation of the filament, we introduce the gyration tensor, or the second mass moment, as expressed in Eqn. (3.2).

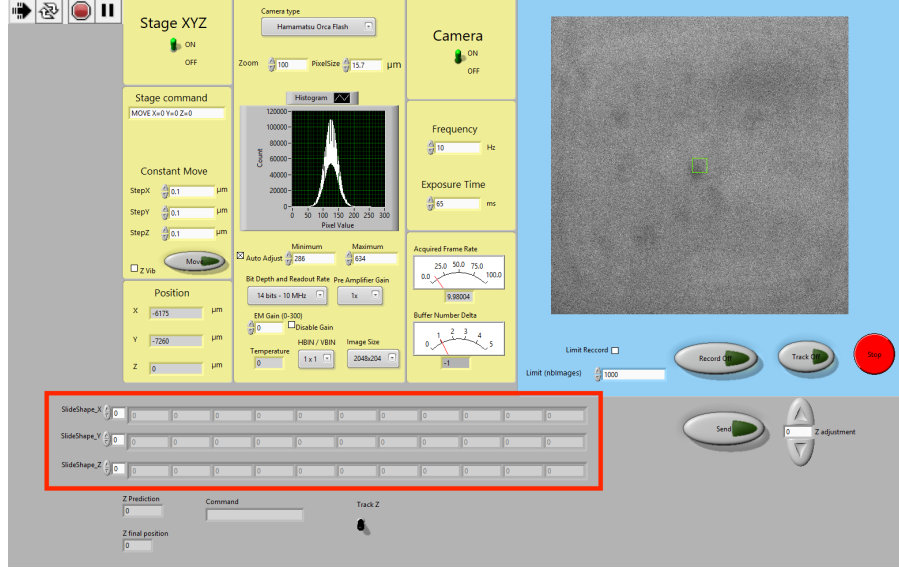


Figure 3.6: The interface of the Labview program.

$$G_{ij}(t) = \frac{1}{L} \int_0^L [r_i(s, t) - \bar{r}_i(t)][r_j(s, t) - \bar{r}_j(t)] ds, \quad (3.2)$$

where $\mathbf{r}(s, t)$ is a two-dimensional parametric representation of the filament centreline with arc length $s \in [0, L]$ in the flow-gradient plane, and $\bar{\mathbf{r}}(t)$ is the instantaneous centre-of-mass position.

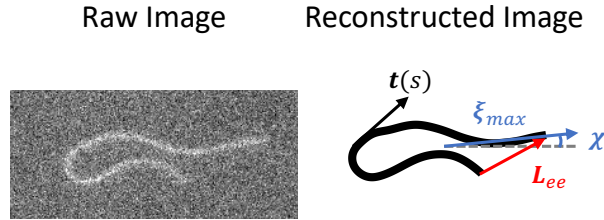


Figure 3.7: Raw image and reconstructed image with corresponding parameters.

Figure 3.7 shows an example of a raw image and reconstructed filament of one configuration as well as the corresponding parameters: L_{ee} (red) is the end-to-end vector, $\mathbf{t}(s)$ (black) is the tangential vector, $\boldsymbol{\xi}_{max}$ (blue) is the eigenvector corresponding to the largest eigenvalue of the gyration tensor of the filament. The angle χ between the mean filament orientation and the flow direction is provided by the eigenvectors of G_{ij} , while its eigenvalues (λ_1, λ_2) can be combined to define a sphericity parameter $\omega = 1 - 4\lambda_1\lambda_2/(\lambda_1 + \lambda_2)^2$ quantifying the filament anisotropy: $\omega \approx 0$. For nearly isotropic configurations ($\lambda_1 \approx \lambda_2$), and $\omega \approx 1$ for nearly straight shapes ($\lambda_1 \gg \lambda_2 \approx 0$). Other relevant measures of the filament conformation are the scaled end-to-end distance $L_{ee}(t)/L = |\mathbf{r}(L, t) - \mathbf{r}(0, t)|/L$, whose departures from its maximum value of 1 are indicative of bent

or folded shapes, and the total bending energy $E(t) = \frac{B}{2} \int_0^L \kappa^2(s, t) ds$, which is an integrated measure of the filament curvature $\kappa(s, t) = |\partial \mathbf{t}(s) / \partial s|$.

3.3 Numerical simulations

We collaborated with Brato Chakrabarti and David Saintillan from UC San Diego, who performed numerical simulations. In close collaboration we advanced together to understand the typical dynamics of flexible filaments in shear flow observed both in experiments and simulations. To probe the dynamics of flexible filaments in shear flow, flexible filaments are modeled as inextensible Euler-Bernoulli beams and non-local slender-body hydrodynamics is used to capture drag anisotropy and hydrodynamic interactions (Tornberg and Shelley, 2004; Manikantan and Saintillan, 2013). Brownian fluctuations are included and satisfy the fluctuation dissipation theorem.

Due to the slenderness of these filaments (aspect ratio $\epsilon \equiv d/L \ll 1$), we opt to describe them as space curves parameterized by arc length $s \in [0, L]$, with Lagrangian marker $\mathbf{r}(s, t)$ denoting the position of any point along the centreline. Noting that the ratio of the energy associated with stretching to that of bending of a filament scales as $E_{str}/E_{bend} \sim (L/d)^2 \sim 10^6$. We thus assume local filament inextensibility which results in a metric constraint on the Lagrangian marker: $\mathbf{r}_s \cdot \mathbf{r}_s = 1$, where indices denote partial differentiation and $\mathbf{r}_s = \hat{\mathbf{t}}$ is the local tangent vector. The bending energy of a filament with contour length L is given by:

$$E = \frac{B}{2} \int_0^L |\mathbf{r}_{ss}|^2 ds, \quad (3.3)$$

where B is the bending rigidity of the filament, which is given by its persistence length $B = \ell_p \times k_B T$. The Phalloidin stabilized actin filaments considered here have a persistence length of $\ell_p = 17 \pm 1 \mu\text{m}$ as measured in section 2.3.2. The hydrodynamics of filaments in an imposed flow $\mathbf{U}(\mathbf{r}) = \dot{\gamma} y$ are described by non-local slender-body theory (Johnson, 1980; Tornberg and Shelley, 2004) as

$$8\pi\mu(\mathbf{r}_t - \mathbf{U}(\mathbf{r})) = -\Lambda[\mathbf{f}](s) - K[\mathbf{f}](s), \quad (3.4)$$

with

$$\Lambda[\mathbf{f}] = [-c(\mathbf{I} + \mathbf{r}_s \mathbf{r}_s) + 2(\mathbf{I} - \mathbf{r}_s \mathbf{r}_s)] \cdot \mathbf{f}(s), \quad (3.5)$$

$$K[\mathbf{f}] = \int_0^L \left(\frac{\mathbf{I} + \hat{\mathbf{R}}\hat{\mathbf{R}}}{|\hat{\mathbf{R}}|} \mathbf{f}(s') - \frac{\mathbf{I} + \mathbf{r}_s \mathbf{r}_s}{|s - s'|} \mathbf{f}(s) \right) ds'. \quad (3.6)$$

Here, μ is the suspending fluid viscosity, $\hat{\mathbf{R}} = \mathbf{r}(s) - \mathbf{r}(s')$, and $c = \ln(e^2/e)$ is a geometric parameter. Λ is a local mobility operator that accounts for drag anisotropy, while the

integral operator K captures the effect of hydrodynamic interactions between different parts of the filament. The force per unit length $\mathbf{f}(s)$ has contributions from bending and tension forces as well as Brownian forces:

$$\mathbf{f}(s, t) = B\mathbf{r}_{ssss} - (\sigma(s)\mathbf{r}_s)_s + \mathbf{f}^{br}, \quad (3.7)$$

where $\sigma(s)$ is the Lagrange multiplier that enforces the constraint of inextensibility and can be interpreted as the internal tension. The Brownian force density \mathbf{f}^{br} obeys the fluctuation-dissipation theorem (Munk et al., 2006; Manikantan and Saintillan, 2013):

$$\langle \mathbf{f}^{br}(s, t) \rangle = 0, \quad (3.8)$$

$$\langle \mathbf{f}^{br}(s, t) \mathbf{f}^{br}(s', t') \rangle = 2k_B T \Lambda^{-1} \delta(s - s') \delta(t - t'). \quad (3.9)$$

Since the filament is freely suspended, we apply force free and moment free boundary conditions at both filament ends, which translate to: $\mathbf{r}_{ss}|_{s=0,L} = 0$, $\mathbf{r}_{sss}|_{s=0,L} = 0$, $\sigma(s)|_{s=0,L} = 0$. We non-dimensionalize the governing equations by scaling spatial variables with L , time by the characteristic relaxation time $8\pi\mu L^4/B$, the external flow by $L\dot{\gamma}$, deterministic forces by the bending force scale B/L^2 and Brownian fluctuations by $\sqrt{L/\ell_p B/L^2}$ (Manikantan and Saintillan, 2013; Munk et al., 2006). The dimensionless equations are given as follows:

$$\mathbf{r}_t = \bar{\mu} \mathbf{U}(\mathbf{r}(s, t)) - \Lambda[\mathbf{f}](s) - K[\mathbf{f}](s), \quad (3.10)$$

$$\mathbf{f} = \mathbf{r}_{ssss} - (\sigma(s)\mathbf{r}_s)_s + \sqrt{L/\ell_p} \boldsymbol{\zeta}, \quad (3.11)$$

These equations show three dimensionless parameters governing the dynamics in this case. First, the elasto-viscous number $\bar{\mu}$ compares the characteristic time scale for elastic relaxation of a bending mode to the time scale of the imposed flow, and is defined in terms of the solvent viscosity μ , applied shear rate $\dot{\gamma}$, length of filaments L and bending rigidity B as $\bar{\mu} = 8\pi\mu\dot{\gamma}L^4/B$. It can be viewed as a dimensionless measure of flow strength and exhibits a strong dependence on the filament contour length. Second, the ratio of the filament persistence length ℓ_p and the contour length L characterizes the importance of transverse fluctuations due to thermal motion, with the limit of $\ell_p/L \rightarrow \infty$ describing rigid Brownian fibers. Third, the anisotropic drag coefficients along the filament involve a geometric parameter $c = -\ln(\epsilon^2 e)$ capturing the effect of slenderness, where $\epsilon = d/L$. The random vector $\boldsymbol{\zeta}$ is uncorrelated in space and time and drawn from a Gaussian distribution with zero mean and unit variance. Equations (3.10)–(3.11) are nu-

merically integrated in time using an implicit-explicit time-stepping method that treats the stiff linear terms coming from bending elasticity implicitly and non-linear terms explicitly. At every time step, the unknown tensions are obtained by solution of an auxiliary dense linear system that can be derived from the inextensibility condition: $\mathbf{r}_{tS} \cdot \mathbf{r}_S = 0$. Further details of the numerical method can be found in (Tornberg and Shelley, 2004; Manikantan and Saintillan, 2013). As experiments only consider quasi-2D trajectories involving dynamics in the focal plane, simulations performed in 2D are indeed found in better agreement than those in 3D. Hence, all simulations presented here were carried out in two-dimensions using $N = 64$ points along the arc length of the filament. Typical time steps for the simulations were of the order of $\Delta t \sim 10^{-10} - 10^{-12}$.

3.4 Morphological dynamics in shear flow

Shear flow can be decomposed into a rotational and a straining part as shown in Fig. 3.8. Hence, when we study flexible filaments in shear flow, of particular interest are filament deformation and periodic rotation. We first describe the observation and analysis of the configurational dynamics.

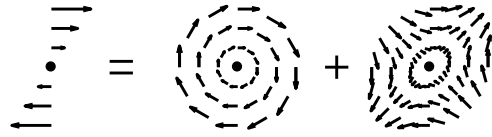


Figure 3.8: The decomposition of shear flow into a rotational and a straining part.

As we mentioned in the previous section, there are three independent dimensionless parameters governing the filament dynamics in this problem, l_p/L , elasto-viscous number $\bar{\mu}$ and slenderness c . In the experiments, the local shear rate $\dot{\gamma}$ experienced by the filaments can be determined by both the flow strength and the position of filaments in the observation plane. By varying L and $\dot{\gamma}$, we have systematically explored the filament dynamics over several decades of the elasto-viscous number and we have observed a variety of filament configurations as shown in Figure 3.9.

From top to bottom, we can see that the dynamics change from tumbling without deformation to significant bending with a flat shape from top to bottom, here named with "**Rod-like tumbling**", "**C shape buckling**", "**U snake turn**" and "**S snake turn**" respectively. As the dynamics vary from one type of morphology to another, the evolution of the local deformation along the arc length over time is quite different as shown in Fig. 3.10, (a) tumbling without significant deformation, (b) one stationary bending part suddenly appears and disappears in the middle, (c) one localized curvature appears at one end and propagates to the other end and (d) two localized bending parts appear at two ends

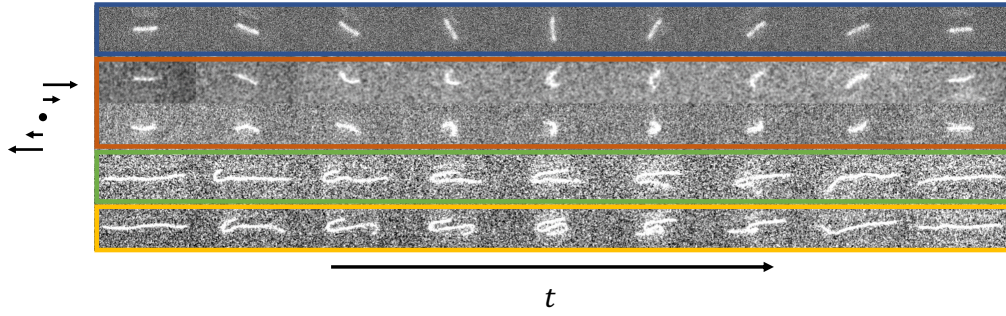


Figure 3.9: Typical dynamics of filaments in shear flow observed in experiments.

and are transported towards the middle. All those cases mentioned here are observed and investigated both in experiments and simulations with an excellent agreement and will be analysed and discussed one by one in the following sections.

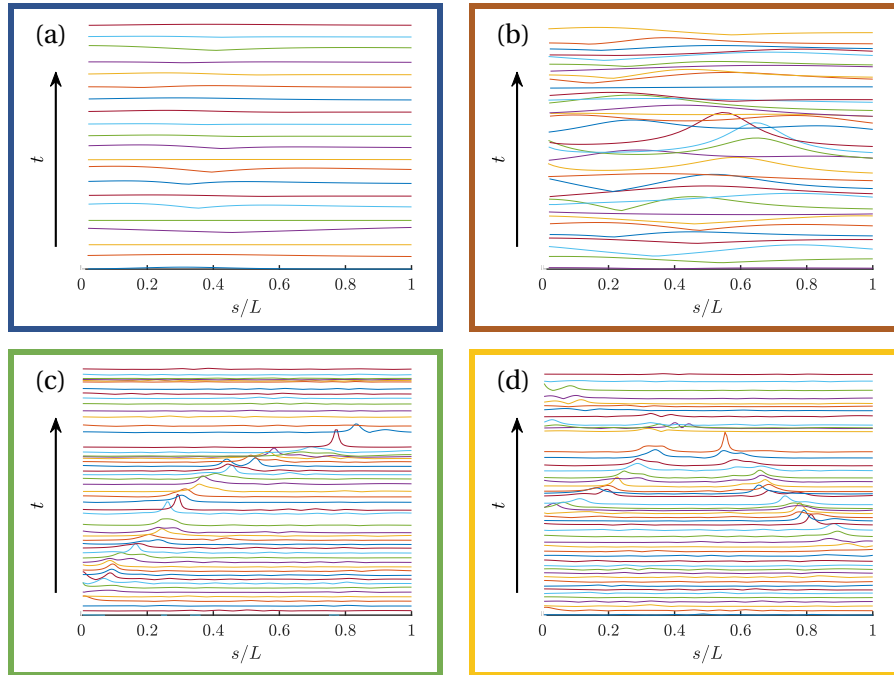


Figure 3.10: Local curvatures propagating along the arc length over time. Each color line represents the curvature along the arc length at different time steps. Colour frames indicate the type of dynamics: (a) Rod-like tumbling, (b) *C* shape buckling, (c) *U* snake turn, (d) *S* snake turn.

3.4.1 Rod-like tumbling

The first dynamics we observe is the rod-like tumbling of short filaments experiencing relatively small shear rates, leading to a small elasto-viscous number. In this case, filaments look always straight without any visible Brownian shape fluctuations and the

filaments are found to tumble without any significant deformation as shown in Fig. 3.11, comparing experimental and numerical result.

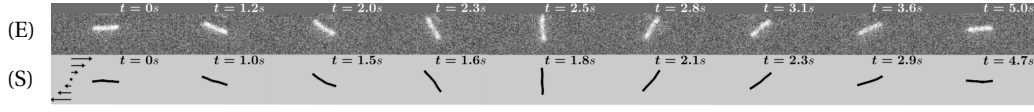


Figure 3.11: Temporal evolution of the filament performing rod-like tumbling in planar shear over one period of motion, comparing experimental images (E) to simulations (S). $\ell_p/L = 3.75$, $\bar{\mu} = 2.9 \times 10^3$

Fig. 3.12 gives a quantitative description of the rod-like tumbling behaviour. During the tumbling, filaments remain nearly straight with $\omega \approx 1$, $L_{ee}/L \approx 1$ and $E \approx 0$ while the mean angle χ quasi-periodically varies between $[-\pi/2, \pi/2]$ over the course of each tumble. The lack of experimental data during $\Delta\dot{\gamma}t \approx 30$ is due to a temporary loss of focus caused by Brownian orientation diffusion induced tumbling in xOz plane.

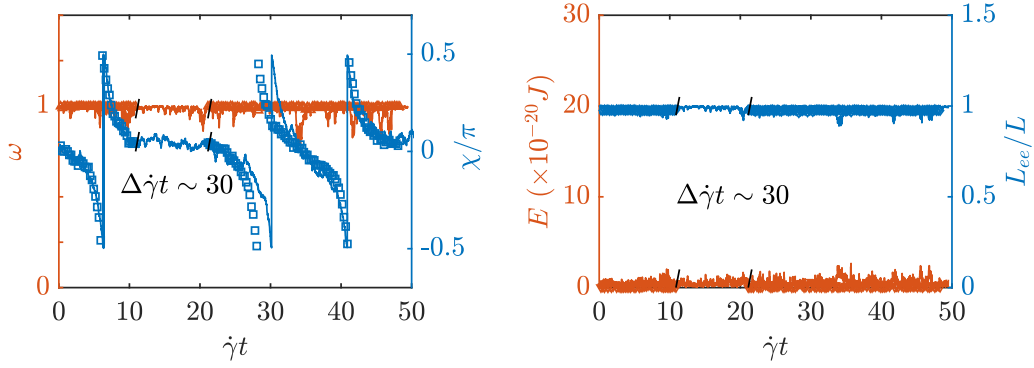


Figure 3.12: The evolution of parameters of a filament performing rod-like tumbling, including the sphericity parameter ω , mean angle χ with respect to the flow direction, bending energy E and scaled end-to-end distance L_{ee}/L over a few periods of motion. Symbols are measurements from experiments and the solid lines are from simulations.

3.4.2 C shape buckling with global rotation

When increasing the elasto-viscous number $\bar{\mu}$, another type of dynamics appears as shown in Fig. 3.13. As filaments rotate, they enter the compressive quadrant of the shear flow, and compressive viscous forces may overcome bending rigidity and drive a structural instability towards a characteristic C shaped configuration.

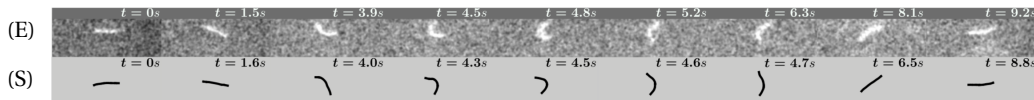


Figure 3.13: Temporal evolution of the filament performing C shaped buckling in planar shear over one period of motion, comparing experimental images (E) to simulations (S). $\ell_p/L = 2.9$, $\bar{\mu} = 3.9 \times 10^3$

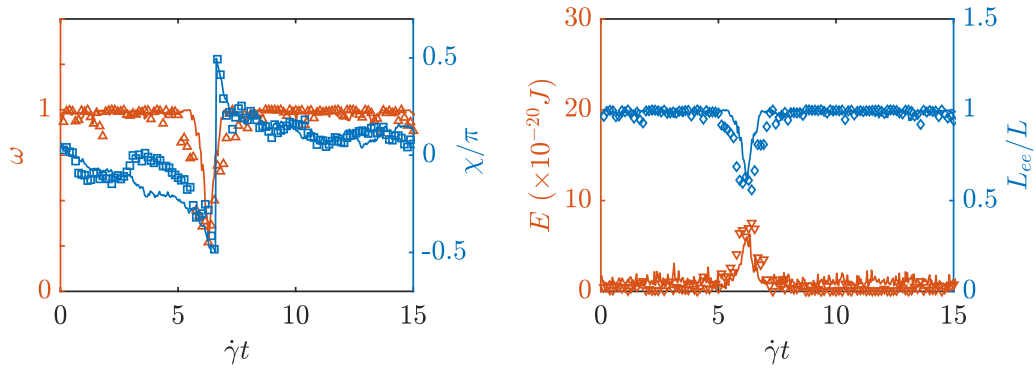


Figure 3.14: The evolution of parameters of a filament performing C shaped buckling dynamics, including the sphericity parameter ω , mean angle χ with respect to the flow direction, bending energy E and scaled end-to-end distance L_{ee}/L over a few periods of motion. Symbols are measurements from experiments and the solid lines are from simulations.

By analogy with Euler beams, we term this deformation mode "global buckling" as it occurs over the full length of the filament. Since it is buckling instability, the filament has the possibility to buckle in two directions with a C or a inverse C shape as shown in Fig. 3.9 and 3.13. During one end over end rotation, the mean orientation angle χ reaches $-\pi/2$ and $\pi/2$, other quantities, including compactness parameter ω and bending energy E as well as scaled end-to-end distance L_{ee}/L , start to deviate from their baseline as the filament start to buckle at $\chi \approx -\pi/2$. After reaching a maximum or minimum value, the parameters return to their baseline as the filament straightens again. Whether the bending energy E has a significant increase or not provides a quantitative measure to distinguish tumbling motion and C buckling.

3.4.3 Snake turn dynamics

3.4.3.1 U snake turn

As we continue increasing the length of the filaments or the strength of the flow, filaments show strongly bent configurations during the rotation, which we call U snake turns. During those turns, filaments strongly deform into hairpin like shapes and remain roughly aligned with the flow direction while a curvature wave initiates at one end of the filament and propagates towards the other end as shown in Fig. 3.15.

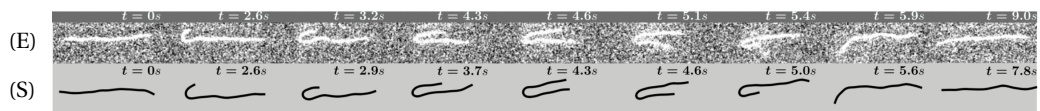


Figure 3.15: Temporal evolution of the filament performing a U snake turn in planar shear over one period of motion, comparing experimental images (E) to simulations (S). $\ell_p/L = 0.83$, $\bar{\mu} = 2,0 \times 10^6$.

During a U snake turn, as shown in Fig. 3.16, the deformations are also significant but the angle χ only weakly deviates from 0, as the filament remains roughly aligned with the flow direction and executes a tank-treading motion rather than an actual tumble. Whether the angle $|\chi|$ reaches $\pi/2$ or not provides a simple criterion for distinguishing C buckling and U snake turns in both experiments and simulations. Other hallmarks of U turns are the very small variation of bending energy during a turn, which exhibits a nearly constant plateau while the localized bend in the filament shape travels from one end to the other, and a strong minimum in the end-to-end distance $L_{ee}(t)$, which reaches nearly zero halfway through the turn when the filament is symmetrically folded. These snake turns are similar to the snaking motions previously observed with non-Brownian flexible fibers (Forgacs and Mason, 1959) and Brownian flexible filaments (Harasim et al., 2013).

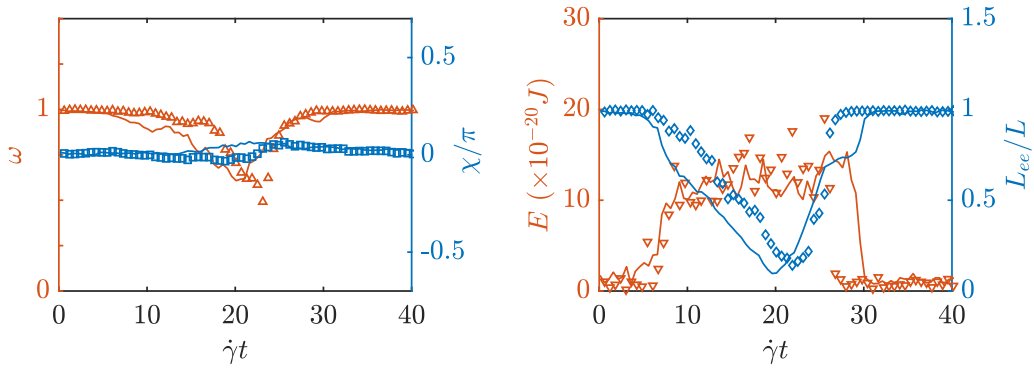


Figure 3.16: The evolution of parameters of a filament performing U snake turns, including the sphericity parameter ω , mean angle χ with respect to the flow direction, bending energy E and scaled end-to-end distance L_{ee}/L over a few periods of motion. Symbols are measurements from experiments and the solid lines are from simulations.

3.4.3.2 S snake turn

At yet higher values of $\bar{\mu}$, an S shape snake turn emerges, with similarities to the U turn. Here the two ends are both curled, which involves two opposing curvature waves emanating successively from both ends and approaching each other, followed by releasing of the two bending parts under extension with a straight final shape as shown in Fig. 3.17. It can also happen that the two ends start to curl at the same time as observed for other examples. Note that the filament shown here is the same filament shown in Fig. 3.15, which means that at a sufficiently high $\bar{\mu}$, both U snake turn and S snake turn can occur for a given filament in different turns.

During an S turn, as shown in Fig. 3.18, the angle χ is only slightly varying around 0, representing a relatively flat configuration. As the two ends start to curve independently, the bending energy corresponds to almost twice of the bending energy of a U turn in both experiments and simulations. When two bending parts encounter each other there is a

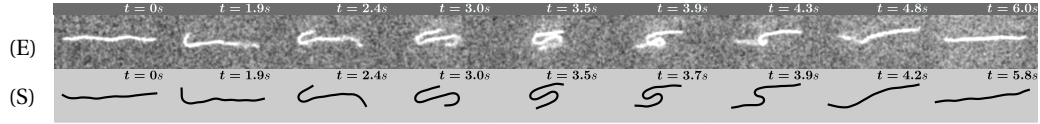


Figure 3.17: Temporal evolution of the filament performing a S snake turn in planar shear over one period of motion, comparing experimental images (E) to simulations (S). $\ell_p/L = 0.83$, $\bar{\mu} = 2,0 \times 10^6$.

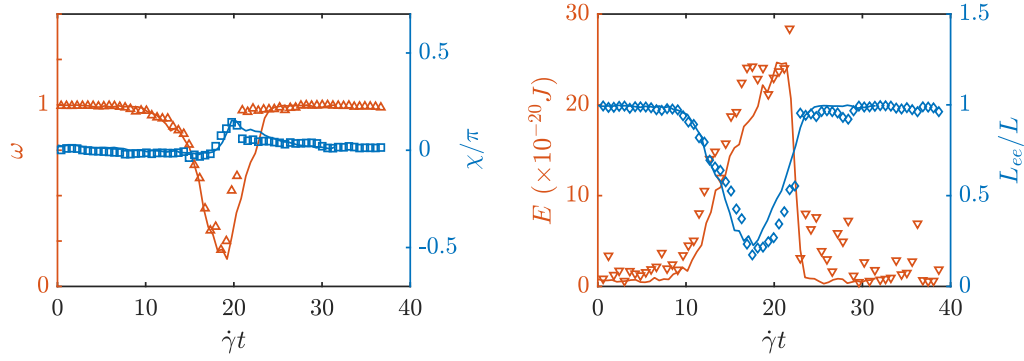


Figure 3.18: The evolution of parameters of a filament performing S snake turn dynamics, including the sphericity parameter ω , mean angle χ with respect to the flow direction, bending energy E and scaled end-to-end distance L_{ee}/L over a few periods of motion. Symbols are measurements from experiments and the solid lines are from simulations.

sharp increase in bending energy, which is also the most compact state with a minimum value of sphericity ω and L_{ee}/L .

3.4.4 Complex dynamics

Increasing the elasto-viscous number $\bar{\mu}$ further, allows us to observe more complex dynamics as shown in Fig. 3.19. The filaments starts in a rather straight shape with only weak fluctuations, as the extensional part of the shear flow suppresses the Brownian fluctuations as the filament aligns with the extensional quadrant (the first snapshot). As soon as the filaments experience compression (the second and third snapshots), higher modes of buckling are observed as well as snaking motions of the two ends. Note that the snaking motion of two ends sets in before the higher mode buckling of centre part of the filament. As two ends are getting closer and closer under compression, filaments can show complex coiled states and are the stretched again when experiencing extension. This behaviour is reminiscent to the coil-stretch behaviour of DNA molecules (Perkins et al., 1997; Schroeder et al., 2003).

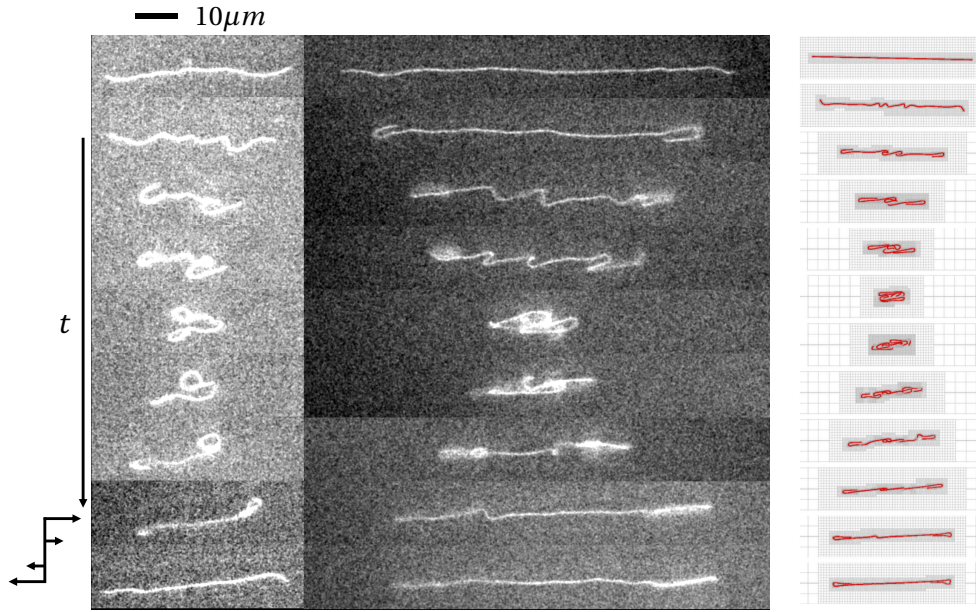


Figure 3.19: Complex configurations of long filaments under shear comparing experimental results and simulations results [Nguyen and Fauci \(2014\)](#).

3.5 Transitions between different dynamics

3.5.1 Order parameters and phase diagram

The descriptive understanding of the dynamics allows us to investigate the evolution of the different filament characteristics as well as the transitions between different deformation regimes with increasing elasto-viscous number $\bar{\mu}$. The dependence on $\bar{\mu}$ of the maximum bending energy E and minimum value of the sphericity parameter ω over one or several periods of motion is shown in Fig. 3.20, in which each marker represents the dynamics of one filament observed during one end-over-end rotation both in experiments and simulations. In experiments, control parameters are the length of the filament L and local shear rate $\dot{\gamma}$, used to obtain the elasto-viscous number. In the simulations, the value of the governing parameters l_p/L and $\bar{\mu}$ are chosen to correspond to the experimental values. In the case of rod-like tumbling and U turns, the maximum bending energy is calculated as an average over the whole period or the plateau regime respectively.

In the rod-like tumbling regime, deformations are negligible, as evidenced by the nearly constant values of $\max(E) \approx 0$ and $\min(\omega) \approx 1$. After the onset of buckling, however, the maximum bending energy starts increasing monotonically with $\bar{\mu}$ as viscous stresses cause increasingly stronger bending of the filament. This increased bending is accompanied by a decrease in ω as bending shapes become increasingly isotropic, finally reaching $\min(\omega) \approx 0$ for strongly buckled and rounded shapes. Interestingly, the transition to

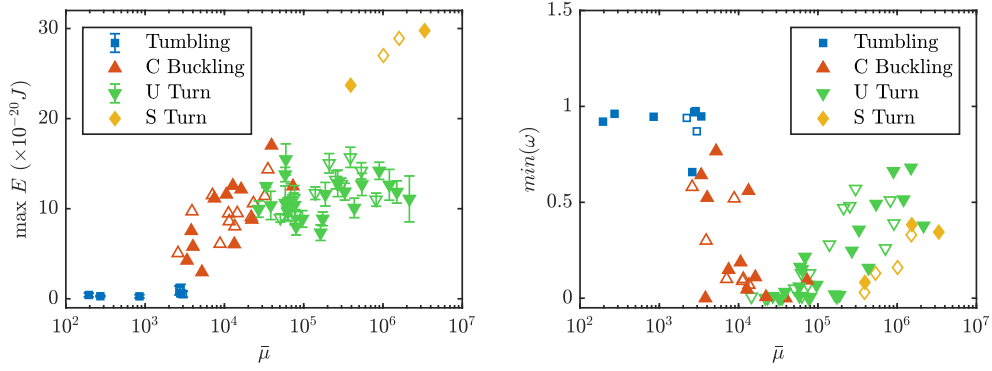


Figure 3.20: The evolution of the maximum bending energy E (left) and the minimum value of the sphericity parameter ω (right) as a function of the elasto-viscous number $\bar{\mu}$ in the different regimes. Full symbols are experimental results; open symbols are simulation results.

U turns is marked by a plateau of the bending energy, which subsequently increases only very weakly with $\bar{\mu}$. This plateau is indicative of the emergence of strongly bent configurations where the elastic energy becomes localized in the sharp folds, and suggests that the curvature of the folds during U turns depends only weakly on flow strength. The parameter ω also starts increasing again after the onset of U turns, as the filaments adopt hairpin shapes that become increasingly anisotropic. In the regime of S turns, the maximum bending energy is approximately twice that of U turns, as bending deformations now become localized in two sharp folds instead of one. At the same time, filaments have more compact configurations due to the two curved parts, $\min(\omega)$ is always smaller, compared to U turns.

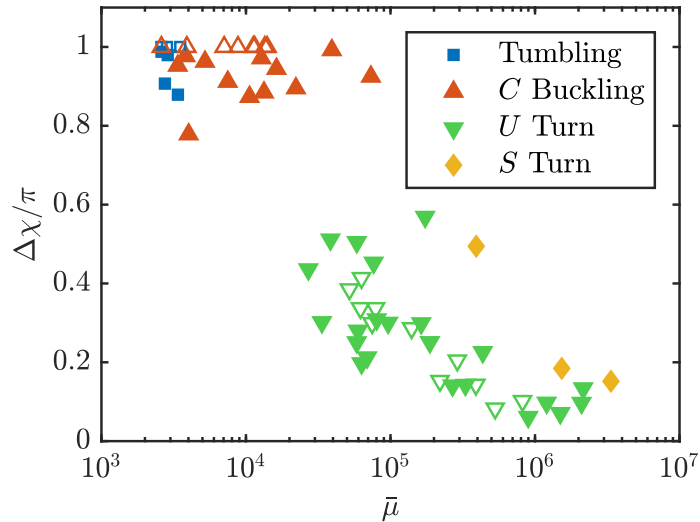


Figure 3.21: $\Delta\chi/\pi = (\max(\chi) - \min(\chi))/\pi$ as a function of $\bar{\mu}$.

Orientation dynamics are summarized in Fig. 3.21, showing the range of the mean angle χ , $\Delta\chi = \chi_{\max} - \chi_{\min}$, over one period of motion. During a rod-like tumbling or C buckling

event, the principal axis of the gyration tensor rotates continuously and as a result $\Delta\chi = \pi$. The scatter in the experimental data in these cases is simply a result of the finite frame rate. During U turns and S turns, however, the filament no longer performs tumbles but instead remains aligned with the flow direction as it undergoes its snaking motion, resulting in $\Delta\chi < \pi$. This explains the discontinuity in the data of Fig. 3.21, where C and U turns stand apart. As $\bar{\mu}$ increases beyond the transition, we find that $\Delta\chi \rightarrow 0$ suggesting that bent configurations remain aligned with the flow direction.

With increasing values of $\bar{\mu}$ spanning several decades, our experiments and simulations have uncovered several dynamical regimes: rod-like tumbling regime, C shape buckling regime and snake turn regime including U turn and S turn, and grey transitional regimes as shown in Fig. 3.22 as a phase diagram in the $(\bar{\mu}/c, \ell_p/L)$ parameter space. Each marker from experiments represents the dynamics of one filament observed during one end-over-end rotation, however, each marker in simulations includes the dynamics of one filament during multiple end-over-end rotation. Then a transition region appears when two different dynamics are observed for the same filament. The gray regime in simulations reflects the fact that one filament can perform different dynamics in different periods, directly represented with a gray symbol. In experiments, in the range of elasto-viscous number $\bar{\mu} \in 10^3 \sim 10^4$, both C buckling and U snake turn can be observed, which gives the transitional regime in experiments.

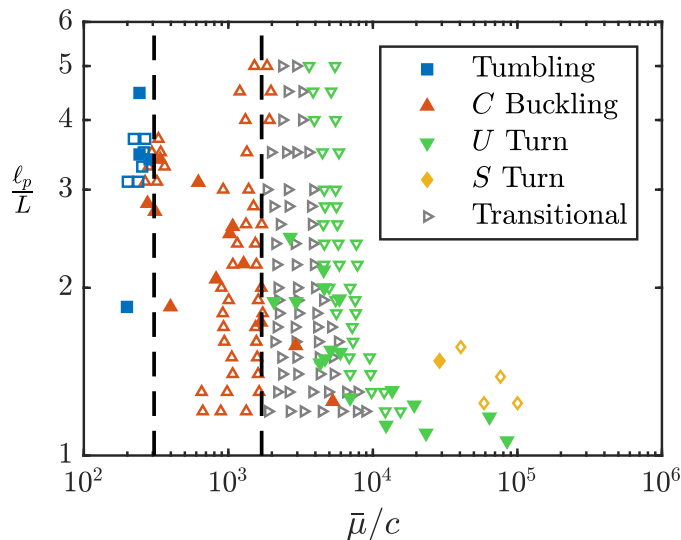


Figure 3.22: Phase chart indicating the different regimes in the $(\bar{\mu}/c, \ell_p/L)$ parameter space. The dashed black lines show the theoretical transitions from stability analysis and U turn dynamics analysis, full symbols are experiments, open symbols are simulations.

The transitions appear to be largely independent of ℓ_p/L . Here $c = -\ln(\epsilon^2 e)$, where $\epsilon = d/L$, is a geometric parameter that captures the effect of slenderness of the filament and c is a logarithm correction due to slenderness. The first transition at $\bar{\mu}_c^{(1)}/c \approx 306.4$ from rod-like tumbling motion to C buckling has received much attention in the past, primarily in the case of non-Brownian filaments ($\ell_p/L \gg 1$) (Becker and Shelley, 2001;

Nguyen and Fauci, 2014; Tornberg and Shelley, 2004). However, here we observed this transition for the first time experimentally in shear flow. This limit is amenable to a linear stability analysis (Becker and Shelley, 2001), which predicts a supercritical pitchfork bifurcation when compressive viscous stresses exerted along the filament as it rotates into the compressional quadrant of the flow are sufficiently strong to induce buckling. The critical value of first buckling mode in shear flow $\bar{\mu}_c^{(1)}/c = 306.4$ is twice the value for linear straining flow 153.2 as shown in Fig 1.2. This is because the straining part of the shear flow is characterized by $\dot{\gamma}/2$. Thermal fluctuations do not significantly alter this threshold, but instead result in a blurring of the transition (Baczynski et al., 2007; Kantsler and Goldstein, 2012; Manikantan and Saintillan, 2015), and in the vicinity of the transition both tumbling and C buckling can be observed for a given value of $\bar{\mu}$. When Brownian motion is strong, i.e. for low values of ℓ_p/L , it becomes challenging to differentiate deformations caused by viscous buckling vs fluctuations, and thus the distinction between the two regimes becomes irrelevant.

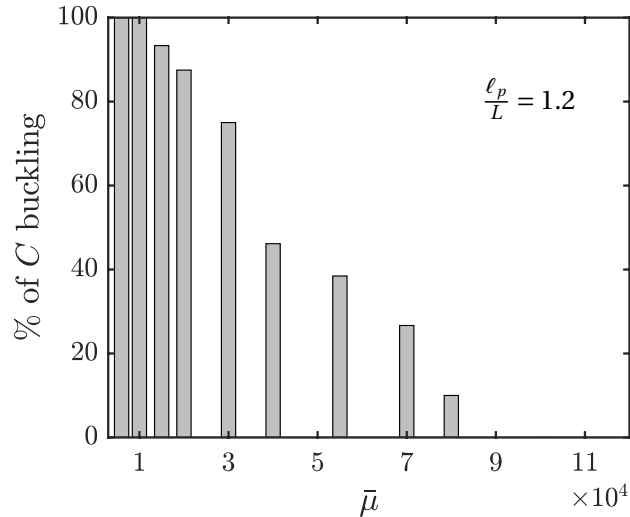


Figure 3.23: Percentage of C buckling events as a function of $\bar{\mu}$ near the transition from C buckling to U turns. The probability is estimated over 10 distinct turns. The results shown are for $\ell_p/L = 1.2$.

Upon increasing $\bar{\mu}/c$, the second conformational transition from C shaped filaments to elongated hairpin-like U turns undergoing snaking motions occurs. The appearance of U turns (shown in green in Fig. 3.22) occurs above a critical value $\bar{\mu}_c^{(2)}/c \approx 1700$ that is again largely independent of ℓ_p/L . However, the transition is not sharp, and near the critical value both shapes can be observed simultaneously as indicated by the gray points. In fact, a single filament in the transitional regime will typically execute both types of turns, switching stochastically between them.

In a similar fashion as for the transition from tumbling to C buckling, thermal fluctuations have a blurring effect, and in the vicinity of $\bar{\mu}_c^{(2)}/c$ both C and U turns can occur over multiple tumbling events. This stochastic transitional regime (marked by gray symbols in Fig. 3.22) increases in width as ℓ_p/L decreases, and is characterized more precisely

in Fig. 3.23. The transitional regime can be characterized by the probability of observing either shape, which can be estimated from simulations and is shown in Fig. 3.23 as a function of $\bar{\mu}$ for a fixed value of $\ell_p/L = 1.2$. As expected, we find that the probability of C buckling continuously decreases from 1 to 0 as $\bar{\mu}$ is varied across the transition and at the same time, the probability of U turns increase from 0 to 1. Similar stochastic transitions have been reported for the onset of buckling in compressional flows (Kantsler and Goldstein, 2012; Manikantan and Saintillan, 2015).

3.5.2 The transition from C buckling to U snake turn

3.5.2.1 Dynamics model of initial state of U snake turn

The transition from C buckling towards snaking dynamics has not previously been characterized. Our attempt at understanding its mechanism focuses on the onset of a U turn. The initiation of a U turn in both experiments and simulations involves the formation of a J -shaped configuration which is tilted with respect to the flow direction and is a precursor to the U snake turn as visible in Fig. 3.15 and also illustrated in Fig. 3.24. From Fig. 3.24-(A), we can see the filament evolves from being aligned with the flow to a tilt J shape. It also shows that the J configuration developed from a global buckling shape at a small tilt angle. To further elucidate the transition to U turns, we seek a simplified model of the J configuration shown in Fig. 3.25-(B). The J shape consists of a semi-circle of radius R connected to a straight arm with a tilt angle ϕ with the flow direction and the whole filament has a snaking velocity V_{snake} along the tangential direction.

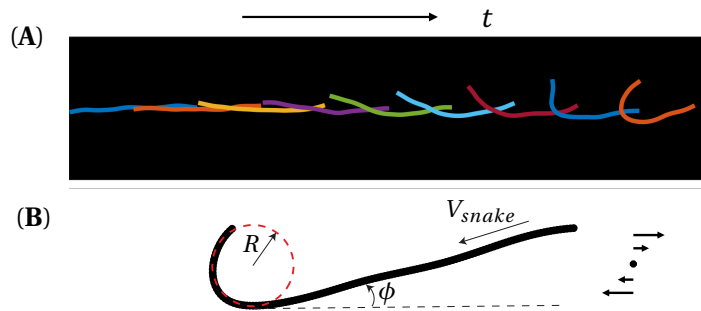


Figure 3.24: (A) A typical J shape before the initiation of a U turn taken from an experimental image. (B) The bent part is approximated by a semicircle of radius R ; the straight part has a tilt angle of ϕ with the direction of the flow and there is an axial velocity V_{snake} .

By satisfying filament inextensibility as well as force and torque balances, and by balancing viscous dissipation in the fluid with the work of bending forces, we are able to solve for model parameters such as R and ϕ . A key aspect of the model is that consistent solutions for these parameters can only be obtained above a critical elasto-viscous number, and this solvability criterion thus provides a threshold $\bar{\mu}_c^{(2)}/c \approx 1700$ below which the J shape ceases to exist. The theoretical prediction for $\bar{\mu}_c^{(2)}/c$ based on this argument is de-

picted by the dashed line in the phase chart of Fig. 3.22 and is in good agreement with both simulations and experiments.

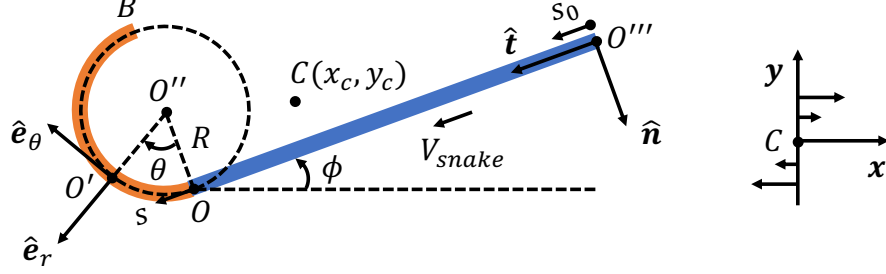


Figure 3.25: Theoretical model of the J configuration. The bent part is approximated by a semi-circle of radius R . There is a snaking velocity, V_{snake} along the contour of the shape. The straight part of the configuration has a tilt angle of ϕ with the direction of the flow.

To model the dynamics of the J configuration, we also introduce different coordinates xOy , $\hat{i}O\hat{n}$ and $\hat{e}_\theta O\hat{e}_r$ for convenience in calculations as shown in Fig. 3.25 and the following notations:

- $T^{(1)} \equiv$ velocity of the straight arm in the tangential direction \hat{t} .
- $v_\perp^{AO} \equiv$ velocity of the straight arm in the normal direction \hat{n} .
- $T(\theta) \equiv$ velocity of the semi-circle along \hat{e}_θ .
- $v_\perp^{OB} \equiv$ velocity of the semi-circle in the \hat{e}_r direction.
- $C(x_c, y_c) \equiv$ filament center of mass.
- $(x, y) \equiv$ global coordinate axes centered at O .
- $l \equiv$ length of the straight arm, also given by: $l = L - \pi R$ where L is the filament contour length.

Note that the assumption of a semi-circular shape for the bend leads to some inconsistencies. In particular, it is not possible to satisfy the force and moment free boundary conditions at point B . Adding a second straight arm emanating from B would allow circumventing this issue, and the model we present here is justified in the limit of the length of that second arm becoming zero. Additional inconsistencies also arise at point O , where not all derivatives of the filament shape are zero. These assumptions are necessary to make analytical progress, and we will see *a posteriori* that the model produces results that are in good agreement with experimental and simulation data.

With the definitions above, the relative velocity between the fluid and the straight arm in the tangential and normal directions can be expressed as:

$$v_\parallel^{rel} = T^{(1)} + \dot{\gamma} [(l - s_0) \sin \phi - y_c] \cos \phi, \quad (3.12)$$

$$v_\perp^{rel} = v_\perp^{AO}(s_0) - \dot{\gamma} [(l - s_0) \sin \phi - y_c] \sin \phi \quad (3.13)$$

As there are no forces acting in the normal direction inside the straight arm, we set $v_{\perp}^{rel} = 0$ which yields

$$v_{\perp}^{AO}(s_0) = \dot{\gamma} [(l - s_0) \sin \phi - y_c] \sin \phi. \quad (3.14)$$

In the tangential direction, the internal tension $\sigma(s)$ induces an elastic force density $\mathbf{f}(s) = \sigma_s \hat{\mathbf{t}}$. This force density is balanced against viscous stresses using resistive force theory as $-\sigma_s = c_{\parallel} v_{\parallel}^{rel}$, which can be integrated using the force free boundary condition at point O''' to yield

$$\begin{aligned} \sigma(s_0) = & -c_{\parallel} T^{(1)} s_0 \\ & + c_{\parallel} \dot{\gamma} [(l s_0 - \frac{1}{2} s_0^2) \sin \phi - y_c s_0] \cos \phi. \end{aligned} \quad (3.15)$$

We have introduced the coefficient of resistance per unit length in the tangential direction, which is expressed as

$$c_{\parallel} \approx \frac{2\pi\mu}{\log(2L/d)} \quad (3.16)$$

and we similarly define $c_{\perp} \approx 2c_{\parallel}$ as the resistance coefficient for transverse motion.

We analyze the kinematics and force balance on the semi-circular arc in a similar fashion and first express the relative velocities along the arc as

$$v_{\parallel}^{rel} = T + \underbrace{v_f \cos(\theta - \phi)}_{v_{\parallel}^f}, \quad (3.17)$$

$$v_{\perp}^{rel} = v_{\perp}^{OB} + \underbrace{v_f \sin(\theta - \phi)}_{v_{\perp}^f}, \quad (3.18)$$

where $v_f = \dot{\gamma} R [\cos \phi - \cos(\theta - \phi)] - \dot{\gamma} y_c$. Seeking a balance between elastic and viscous forces in the tangential and normal directions, we obtain:

$$-\frac{1}{R} \frac{d\sigma}{d\theta} = c_{\parallel} v_{\parallel}^{rel}, \quad (3.19)$$

$$\frac{\sigma}{R} + \frac{B}{R^3} = c_{\perp} v_{\perp}^{rel}. \quad (3.20)$$

The constraint of inextensibility introduces a kinematic relation between the Lagrangian velocities in the tangential and perpendicular directions everywhere along the arc OB , and provides the condition:

$$\frac{dT}{d\theta} + v_{\perp}^{OB} = 0. \quad (3.21)$$

Equations (3.17)–(3.21) can be combined to yield a second-order non-homogeneous

ODE for $v_{\perp}^{OB}(\theta)$:

$$2\frac{d^2 v_{\perp}^{OB}}{d\theta^2} - v_{\perp}^{OB} = 2\frac{d^2 v_{\perp}^f}{d\theta^2} + \frac{d^2 v_{\parallel}^f}{d\theta^2}. \quad (3.22)$$

This ODE can be solved analytically subject to continuity of the velocity at point O and to the tension-free boundary condition at point B :

$$v_{\perp}^{OB}(\theta) = C_1 \cosh(\lambda\theta) + C_2 \sinh(\lambda\theta) + \sum_{n=1,2} [\alpha_n \cos(n\theta) + \beta_n \sin(n\theta)], \quad (3.23)$$

where $\lambda = 1/\sqrt{2}$ and

$$C_1 = \frac{\dot{\gamma}R \sin 2\phi}{18}, \quad (3.24)$$

$$C_2 = \frac{B}{c_{\perp}R^3 \sinh(\pi\lambda)} - \frac{\dot{\gamma}R}{18} \sin 2\phi \tanh\left(\frac{\pi\lambda}{2}\right), \quad (3.25)$$

$$\alpha_1 = \dot{\gamma}(y_c - R \cos \phi) \sin \phi, \quad \alpha_2 = -\frac{5}{9}\dot{\gamma}R \sin 2\phi, \quad (3.26)$$

$$\beta_1 = -\dot{\gamma}(y_c - R \cos \phi) \cos \phi, \quad \beta_2 = \frac{5}{9}\dot{\gamma}R \cos 2\phi. \quad (3.27)$$

From v_{\perp}^{OB} , the tangential velocity along the bend is easily inferred as

$$T = v_{\parallel}^f - 2\left(\frac{dv_{\perp}^{OB}}{d\theta} - \frac{dv_{\perp}^f}{d\theta}\right). \quad (3.28)$$

Seeking continuity of tangential velocity and internal tension at point O we obtain two distinct expressions for the tangential velocity $T^{(1)}$ of the straight arm:

$$T^{(1)} = -\frac{2B\lambda}{c_{\perp}R^3 \sinh(\pi\lambda)} + \dot{\gamma}y_c \cos \phi - \frac{2}{9}\dot{\gamma}R \cos 2\phi + \frac{\dot{\gamma}R\lambda}{9} \sin 2\phi \tanh\left(\frac{\pi\lambda}{2}\right), \quad (3.29)$$

$$T^{(1)} = \frac{B}{c_{\parallel}R^2 l} - \frac{\dot{\gamma}l}{4} \sin 2\phi + \dot{\gamma}y_c \cos \phi. \quad (3.30)$$

Interestingly, (3.30) can be shown to also satisfy the torque balance on the filament.

For consistency, we require that Eqn. (3.29) and Eqn. (3.30) be equal. Note, however, that both R and ϕ remain unknown at this point. We therefore seek a third condition based on dissipation arguments similar to those used to explain the tank-treading motion of vesicles (Rioual et al., 2004). Over the course of an infinitesimal time interval δt during a U turn, a length of $\delta L \equiv V_{snake}\delta t$ that was initially straight becomes bent into the semi-circular curve of radius R , where V_{snake} is the snaking velocity. During the same time, the small amount of length becomes straight on the other side of the bend. The amount of work required to bend the straight part can be estimated as the change in its elastic

energy:

$$\delta E = \frac{B}{2} \frac{V_{snake} \delta t}{R^2}. \quad (3.31)$$

This work is provided by viscous stresses acting along the entire filament, and is given by

$$\delta W = \int_L \delta \mathbf{r} \cdot \mathbf{f}_H ds = \delta t \int_L \dot{\mathbf{r}} \cdot \mathbf{f}_H ds, \quad (3.32)$$

where $\mathbf{f}_H = -[c_{\parallel} \mathbf{t}\mathbf{t} + c_{\perp} (\mathbf{I} - \mathbf{t}\mathbf{t})] \cdot \mathbf{v}^{rel}$ is the hydrodynamic force density along the filament and $\dot{\mathbf{r}}$ is the velocity of the corresponding material point. The detailed expression for the integral in Eqn.(3.32) is cumbersome and therefore omitted here. Equating δE and δW and identifying the snaking velocity with the tangential velocity $T^{(1)}$ of the straight arm in the J shape, we obtain the additional condition

$$\frac{BT^{(1)}}{2R^2} = \int_L \dot{\mathbf{r}} \cdot \mathbf{f}_H ds. \quad (3.33)$$

It is possible to recombine (3.29), (3.30) and (3.33) to form two equations for the unknowns R and ϕ . These two equations are then solved numerically using a Newton search algorithm. The equations essentially specify two curves in the (ϕ, R) plane, and a solution only exists when the curves intersect. For a given aspect ratio of the filament, we find that there exists a critical value of $\bar{\mu}$ below which the curves do not intersect. This suggests that below this value J -shapes can no longer form and therefore U turns cannot occur. The theoretically calculated value is plotted as a dashed line in Fig. 3.22 and provides a very good estimate for the onset of U turns.

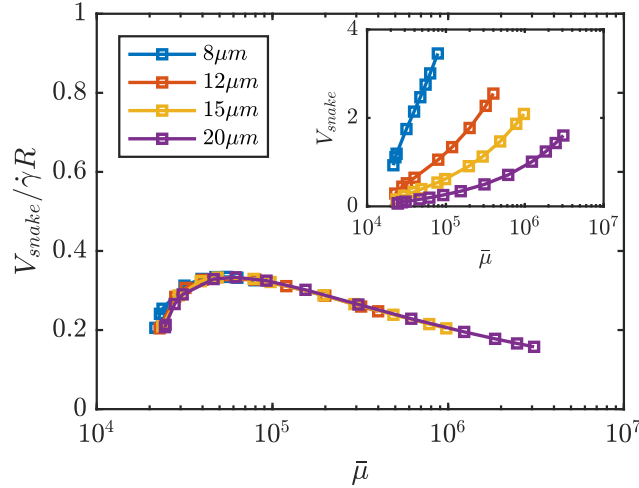


Figure 3.26: Snaking velocity V_{snake} scaled by $\dot{\gamma}R$, the product of shear rate and semi-circle radius, as a function of elasto-viscous number $\bar{\mu}$ as predicted by our theoretical model. Inset: V_{snake} as function of $\bar{\mu}$ with different contour lengths.

The model also provides the theoretical snaking velocity for the straight segment OO''' . The snaking velocities for different filaments with varying lengths is plotted in the inset of the Fig. 3.26 as a function of elasto-viscous number. After scaling with the product

of the radius of the bending segment R and the shear rate $\dot{\gamma}$, all the data for different filament lengths collapse onto a master curve that only depends weakly on $\bar{\mu}$ in Fig. 3.26. This collapse therefore confirms that the relevant dynamic length and time scales during the snaking motion are R and $\dot{\gamma}^{-1}$, respectively.

3.5.2.2 Parameters and comparison between experiments, numerics and J shape model

Our theoretical model approximates the J shape by a straight segment and a semi-circular arc. In this idealized configuration, the curvature is zero along the straight segment and then constant at $1/R$ over a length of πR . After a J shape is initiated as discussed at the end of section 3.5.2.1, the curvature of the folded region remains nearly constant in time as suggested by the plateau in the bending energy as shown before in Fig. 3.16. This provides a strong basis for approximating the bending part of the filament as a semi-circle of radius R from the average bending energy $\langle E \rangle$, which gives $R = B\pi/2\langle E \rangle$, B is bending rigidity.

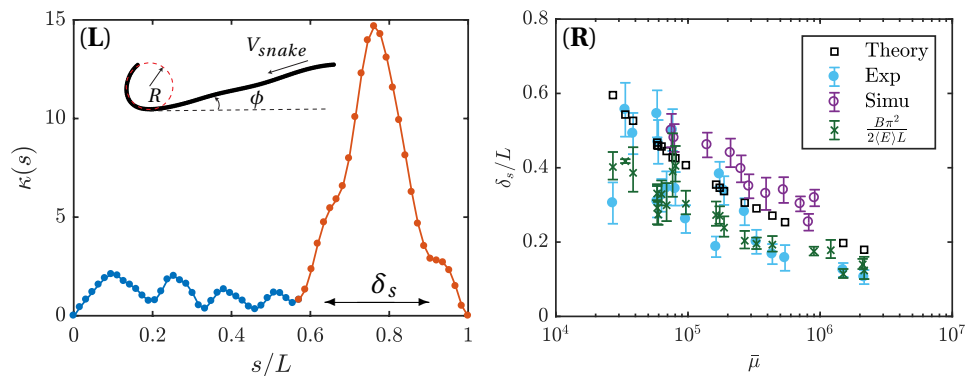


Figure 3.27: (L): Variation of curvature κ along the filament centerline for a typical J shape chosen from a simulation. The length marked as δ_s provides an estimate for the arclength of the bent portion. (R): Comparison of measurements of the length of the bending portion normalized by L vs the elasto-viscous number $\bar{\mu}$ during a U turn.

In experiments and simulations, however, the curvature varies smoothly and must reach zero at $s = 0, L$ due to the boundary conditions. A typical curvature profile from a simulation is shown in Fig. 3.27(L). In order to estimate the radius R in a way that is consistent with the model, we measure the arclength δ_s over which the curvature increases from zero at $s = L$ and decreases again to reach nearly zero. The comparison between scaled bending length from theoretical estimation, bending energy estimation, experiment and simulation measurements show similar trends but weakly differ quantitatively in Fig. 3.27(R).

We further characterize the dynamics during U -turns, for which our theoretical model also provides predictions. The filament orientation at the onset of a U turn is characterized in Fig. 3.28(L), showing the tilt angle ϕ formed by the straight arm of the J shape with

respect to the flow direction as a function of $\bar{\mu}$. Our theoretical model for dynamics of the J shape also provides the value of ϕ , which shows excellent agreement with experimental measurements. In both cases, the tilt angle decreases with the increasing flow strength due to increased alignment by the flow, also seen in Fig. 3.21. For very long filaments, in the limit of large $\bar{\mu}$, accurate measurements of the tilt angle become challenging due to shape fluctuations, hence the increased scatter in the data.

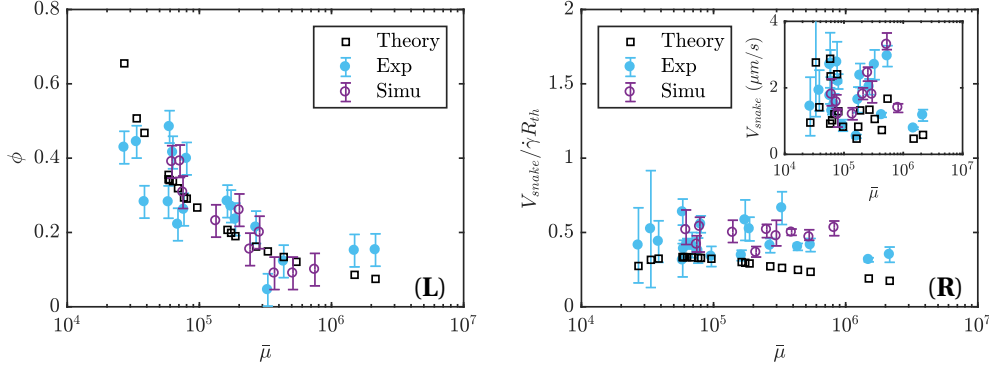


Figure 3.28: (L) Theoretical predictions compared with experiments and simulations on the tilt angle of the J shape with the direction of flow. (R) Snaking velocity rescaled with $\dot{\gamma} R_{th}$ plotted against $\bar{\mu}$ comparing experiments, simulations and theory; here R_{th} is theoretically predicted radius.

The rotation of the end-to-end vector during the U turn results primarily from snaking or tank-treading of the filament along its arc length, unlike the global rotation that dominates the tumbling and C buckling regimes. While the snaking velocity is not constant during a turn, its average value can be quantitatively measured using time derivative of L_{ee} , which provides $\dot{L}_{ee} = 2V_{snake}$. The relevant dynamic length and time scales during this snaking motion are therefore the radius of curvature R of the bent segment and shear rate $\dot{\gamma}$ respectively. This is also suggested by our theory, which indeed collapses all the data shown in Fig. 3.26. Good qualitative agreement, comparing the results from both experiments and simulations, scaled with the product of shear rate and theoretically predicted value of R , is shown in Fig. 3.28(R).

3.6 Frequency dynamics in shear flow

Jeffery orbits have a periodic rotational motion with a period of $2\pi(\epsilon + 1/\epsilon)/\dot{\gamma}$, here $\epsilon = d/L$, which comes from the theoretical solution of the rotation of the ellipsoid's principal axis as shown in Eq. 3.34.

$$\tan\theta = \epsilon \tan\left[-\frac{\dot{\gamma}t}{\epsilon + 1/\epsilon}\right] \quad (3.34)$$

Here θ is the orientation of the ellipsoid. When the rigid ellipsoid becomes a flexible and Brownian filament, it is subject to orientation diffusion and to shape fluctuations from thermal forces and to deformation due to viscous forces. We use the gyration angle χ to present the orientation of the flexible filaments. The time evolution of the scaled gyration angle χ/π of one experiment gives the periodical rotation of the filaments as shown in Fig. 3.29(L). The filament performs C shape buckling during multiple periods. Fig. 3.29(R) shows the corresponding probability distributions of the scaled orientation angle χ/π .

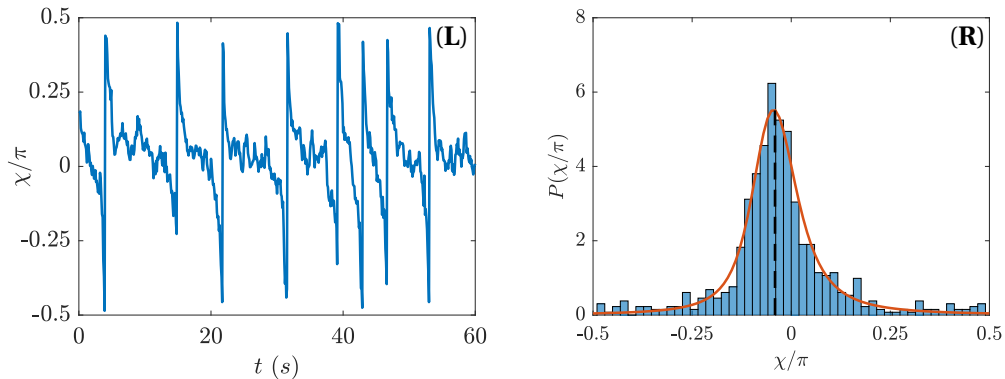


Figure 3.29: (L): The periodically varying of the scaled mean orientation χ/π . (R): The probability distribution of scaled mean orientation $\chi\pi$ during multiple rotations. The filament performs tumbling and buckling during the multiple rotations.

Fig. 3.29 shows the varying of orientation of a filament performing C buckling with a length of $5\mu m$, experienced shear rate $\dot{\gamma} = 2.7s$. Due to Brownian effects, the frequency dynamics of flexible filaments contain two regimes: during the diffusion phase τ_{diff} the frequency dynamics are characterized by orientation diffusion, during the advective phase τ_{adv} the frequency dynamics are governed by the typical morphological dynamics (Harasim et al., 2013). The two phases are separated by a critical angle ϕ_c . According to the work of (Kobayashi and Yamamoto, 2010), the center of the peak in the probability density function of orientation distribution is in good approximation with the critical angle ϕ_c , so that the most probable angle for the filament orientation is slightly "above" the fully aligned state.

The rotation frequency is given by $f = 1/2\tau_{rot}$, τ_{rot} is the reciprocal of the period and can be measured from the period of varying angle χ . We can derive the frequency of the end over end rotation for different filaments based on our experimental results. Fig. 3.30 shows the scaled frequency of different morphological dynamics with bending relaxation time as a function of $\bar{\mu}/c$, the governing dimensionless number of morphological dynamics. However, the best fit to our experimental data gives a scaling law of $f\tau \sim (\bar{\mu}/c)^{6/7}$, which is slightly different from the classical law $f\tau \sim (\bar{\mu}/c)^{2/3}$ for Brownian rods (Kobayashi and Yamamoto, 2010) and flexible filaments (Harasim et al., 2013) as well as from the revised scaling law $f\tau \sim (\bar{\mu}/c)^{3/4}$ based on a local buckling hypothesis (Lang et al., 2014). Note that our experimental results are based on a limited number

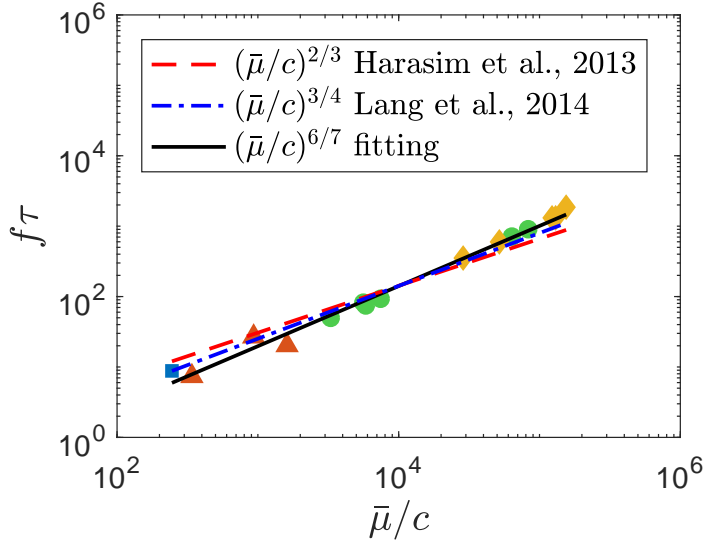


Figure 3.30: Frequency scaling for a limited number of rotations. The tumbling frequency f is non-dimensionalized by the relaxation time $\tau = 8\pi\mu L^4/Bc$, where μ is viscosity, L is the length of the filament, B is bending rigidity and $c = -\ln(e^2/e)$ is the slenderness.

of rotations which brings a certain degree of uncertainty.

3.7 Summary

Using Phalloidin stabilized actin filaments as a model polymer, we have systematically studied and analyzed the dynamics of elastic Brownian filaments in simple shear flow as well as the evolution and conformational transitions between dynamics as the elasto-viscous number is increased. Our experimental measurements were shown to be in excellent agreement with a computational model describing the filaments as fluctuating elastic rods with slender body hydrodynamics. By varying the filament contour length and the applied shear rate, we performed a broad exploration of the parameter space and confirmed the existence of a sequence of transitions, from rod-like tumbling to elastic buckling to snaking motions. While snaking motions had been previously observed in a number of experimental configurations, the existence of a C buckling regime had not been confirmed clearly. This is due to the fact that C buckling is only visible over a limited range of elasto-viscous numbers and occurs only in simple shear flow, challenging to realize experimentally. We shown that both transitions are primarily governed by $\bar{\mu}/c$. Brownian fluctuations do not modify the thresholds but tend to blur the transitions by allowing distinct dynamics to coexist over certain ranges of $\bar{\mu}$.

While the first transition from tumbling to buckling had been previously described as a supercritical linear buckling instability (Becker and Shelley, 2001), the transition from buckling to snaking was heretofore unexplained. Using a simple analytical model for the dynamics of the J shape that is the precursor to snaking turns, we were able to obtain a

theoretical prediction for the threshold elasto-viscous number above which snake turns become possible. The model did not take thermal noise into account, but highlighted the subtle role played by compression and tension during the onset of the turn. We also observed and analyzed the frequency dynamics of flexible filaments, comparing our results to previous studies. Our analysis and model lay the groundwork for illuminating a wide range of other complex phenomena in polymer solutions, from their rheological response in flow and dynamics in semi-dilute solutions (Kirchenbuechler et al., 2014; Huber et al., 2014) to migration under confinement to the microfluidic control of filament dynamics.

References

- Baczynski, K., Lipowsky, R., and Kierfeld, J. Stretching of buckled filaments by thermal fluctuations. *Physical Review E*, 76(6):061914, 2007.
- Becker, L. E. and Shelley, M. J. Instability of elastic filaments in shear flow yields first-normal-stress differences. *Physical Review Letters*, 87(19):198301, 2001.
- Forgacs, O. and Mason, S. Particle motions in sheared suspensions: X. orbits of flexible threadlike particles. *Journal of Colloid Science*, 14(5):473–491, 1959.
- Gittes, F., Mickey, B., Nettleton, J., and Howard, J. Flexural rigidity of microtubules and actin filaments measured from thermal fluctuations in shape. *Journal of Cell biology*, 120:923–923, 1993.
- Guglielmini, L., Kushwaha, A., Shaqfeh, E., and Stone, H. Buckling transitions of an elastic filament in a viscous stagnation point flow. *Phys. Fluids*, 24:123601, 2012.
- Harasim, M., Wunderlich, B., Peleg, O., Kröger, M., and Bausch, A. R. Direct observation of the dynamics of semiflexible polymers in shear flow. *Physical review letters*, 110(10):108302, 2013.
- Huber, B., Harasim, M., Wunderlich, B., Kröger, M., and Bausch, A. R. Microscopic origin of the non-newtonian viscosity of semiflexible polymer solutions in the semidilute regime. *ACS Macro Letters*, 3(2):136–140, 2014.
- Jeffery, G. B. The motion of ellipsoidal particles immersed in a viscous fluid. In *Proceedings of the Royal Society of London A: Mathematical, Physical and Engineering Sciences*, volume 102, pages 161–179. The Royal Society, 1922.
- Johnson, R. E. An improved slender-body theory for Stokes flow. *J. Fluid Mech.*, 99:411–431, 1980.
- Kantsler, V. and Goldstein, R. E. Fluctuations, dynamics, and the stretch-coil transition of single actin filaments in extensional flows. *Physical review letters*, 108(3):038103, 2012.

- Kirchenbuechler, I., Guu, D., Kurniawan, N. A., Koenderink, G. H., and Lettinga, M. P. Direct visualization of flow-induced conformational transitions of single actin filaments in entangled solutions. *Nature communications*, 5, 2014.
- Kobayashi, H. and Yamamoto, R. Tumbling motion of a single chain in shear flow: a crossover from brownian to non-brownian behavior. *Physical Review E*, 81(4):041807, 2010.
- Lang, P. S., Obermayer, B., and Frey, E. Dynamics of a semiflexible polymer or polymer ring in shear flow. *Physical Review E*, 89(2):022606, 2014.
- Linder, A. and Shelley, M. Elastic fibers in flows,. In *Fluid-Structure Interactions in Low-Reynolds-Number Flows*, pages 168–192. The Royal Society of Chemistry, 2016.
- Liu, Y., Chakrabarti, B., Saintillan, D., Lindner, A., and Roure, O. d. Tumbling, buckling, snaking: Morphological transitions of elastic filaments in shear flow. *arXiv preprint arXiv:1803.10979*, 2018.
- Manikantan, H. and Saintillan, D. Subdiffusive transport of fluctuating elastic filaments in cellular flows. *Physics of Fluids*, 25(7):073603, 2013.
- Manikantan, H. and Saintillan, D. Buckling transition of a semiflexible filament in extensional flow. *Physical Review E*, 92(4):041002, 2015.
- Munk, T., Hallatschek, O., Wiggins, C. H., and Frey, E. Dynamics of semiflexible polymers in a flow field. *Physical Review E*, 74(4):041911, 2006.
- Nguyen, H. and Fauci, L. Hydrodynamics of diatom chains and semiflexible fibres. *Journal of The Royal Society Interface*, 11(96):20140314, 2014.
- Perkins, T. T., Smith, D. E., and Chu, S. Single polymer dynamics in an elongational flow. *Science*, 276(5321):2016–2021, 1997.
- Rioual, F., Biben, T., and Misbah, C. Analytical analysis of a vesicle tumbling under a shear flow. *Physical Review E*, 69(6):061914, 2004.
- Schroeder, C. M., Babcock, H. P., Shaqfeh, E. S., and Chu, S. Observation of polymer conformation hysteresis in extensional flow. *Science*, 301:1515–1519, 2003.
- Tornberg, A.-K. and Shelley, M. J. Simulating the dynamics and interactions of flexible fibers in stokes flows. *Journal of Computational Physics*, 196(1):8–40, 2004.
- White, F. M. and Corfield, I. *Viscous fluid flow*, volume 3. McGraw-Hill New York, 2006.
- Young, Y.-N. and Shelley, M. J. Stretch-coil transition and transport of fibers in cellular flows. *Physical review letters*, 99(5):058303, 2007.

Chapter 4

The dynamics of flexible filaments in straining flow

Contents

4.1 Introduction	62
4.2 Microfluidic device for linear straining flow	63
4.2.1 Optimized hyperbolic channel	63
4.2.2 Experimental Implementation	67
4.3 Filament dynamics	70
4.3.1 Experimental observations	70
4.3.2 Suppression of Brownian fluctuations in extensional flow	73
4.3.3 Buckling and helical coiling under compression	74
4.4 Summary	76
4.5 Discussion and outlook	77
References	78

4.1 Introduction

In the previous chapter we have investigated the dynamics of flexible filaments in shear flow. We have shown that the particularly rich dynamics observed result from the combination of the rotational and straining components of the shear flow. Investigating filament dynamics in a linear straining flow might allow for a simpler and more detailed analysis of some of the dynamics observed, as for example the threshold of the buckling instability or the suppression of Brownian fluctuations. While conceptually a linear straining flow seems the natural starting point for the investigation of the dynamics of flexible filaments, its experimental realization is not straight forward. Shear flows are however naturally encountered in laboratory experiments and applications and have thus been presented first in this manuscript.

Some previous experiments have been performed on the dynamics of flexible filaments in microscopic or macroscopic straining flows using stagnation point flows or cellular arrays. In these flows compressive and extensional quadrants exist and dynamics can thus be investigated under compression and extension. The main focus of these studies has been on the successive buckling modes observed in the compressive part, but (Kantsler and Goldstein, 2012) have also investigated the suppression of Brownian fluctuations for filaments in the extensional part. The disadvantage of these experiments is the limited residence time of the filaments in well controlled flow conditions. In the microfluidic experiment (Kantsler and Goldstein, 2012) an actin filament has been held fixed at a stagnation point in a microfluidic channel, requiring very precise flow and pressure control at the inlets and outlets. Due to reorientation of the filament at the stagnation point, a filament first experiences compression and then extension in a typical experiment. When transported in a cellular vortex array, an array of stagnation points, as investigated by (Quennouz et al., 2015) in a macroscopic set-up, filaments are transported through the flow experiencing alternatively compression and extensions. While this gives rise to very interesting transport dynamics, residence times in the compressive or extensional quadrants are again short.

Here we aim at investigating the dynamics of actin filaments when transported in linear straining flows under compression and extension with reasonably long residence times. To do so, we will implement a microfluidic flow geometry using a channel design given by a numerical optimization by (Zografos et al., 2016). We will develop a specific tracking algorithm to follow filaments during their transport to obtain good quality images. Using this novel set-up we will investigate the filament dynamics under extension and compression in very well defined flow conditions. Suppression of Brownian fluctuations of the filament will be investigated in extensional flow as a function of filament properties and applied strain rate, whereas filament buckling dynamics will be investigated in the compressive flow.

4.2 Microfluidic device for linear straining flow

A number of microfluidic studies have investigated the dynamics of microscopic objects as filaments, bubbles or red blood cells, using simply a channel with a constriction (Mercader et al., 2010; Nunes et al., 2013; Brosseau et al., 2014; Mancuso and Ristenpart, 2017; Strelnikova et al., 2017). The acceleration/deceleration of the fluid when entering or exiting the constriction leads to extensional/compressive components in the flow field (Rothstein and McKinley, 2001). However the extension rate in these geometries is not well controlled and varies during the transport of particles through the constriction (Oliveira et al.).

Mathematically a pure straining flow corresponds to a hyperbolic flow and in numerical simulations, changing the background flow from shear flow to a straining flow is simple to implement. However due to the no slip boundary condition at the walls of microfluidic channels it is not enough to simply fabricate a hyperbolic geometry for the experiments. In addition a contracting or diverging channel is continuously changing aspect ratio and as a consequence the three dimensional flow profile, adding to the complexity of the flow.

Here we will benefit from numerical work on optimized hyperbolic channel geometries by (Zografos et al., 2016). Optimization has been used previously to design microfluidic flow geometries for the determination of extensional viscosities of non-Newtonian (Galindo-Rosales et al., 2013; Haward, 2016) in two dimensional geometries. In their work (Zografos et al., 2016) optimize three dimensional channel geometries to obtain a constant extension/compression rate on the center line of their channels. Their design is thus perfectly adapted to our requirements and will be described in the next section.

4.2.1 Optimized hyperbolic channel

The optimized hyperbolic channel has symmetric converging and diverging parts to create both extensional and compressive flow. As mentioned before, pure straining flow is only obtained at the centerline of the channel, with respect to both the channel width and the channel height. In order to guide filaments to be transported along the centerline with respect to the channel width, we combine a flow focusing device with the hyperbolic channel as shown in Fig. 4.1. The flow focusing device has three branches which have the same width as the converging part downstream. To observe only filaments transported at mid-height in the channel we work with a high magnification objective with a small focal depth.

Tuning the ratio of the flow rates between the two side branches Q_1 , Q_2 and the middle branch Q_3 allows to focus the inner fluid into a narrow strip. When the flow rates sat-

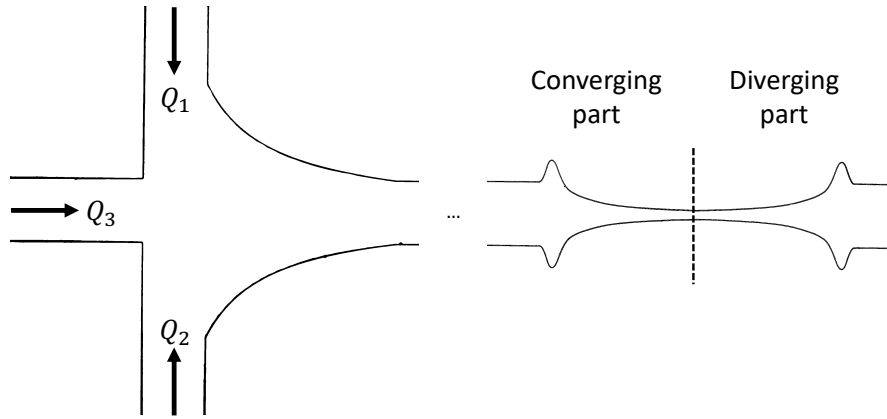


Figure 4.1: The geometry of the microfluidic channel (processed experimental image). The left part corresponds to the flow focusing device, the right part to the hyperbolic channel. The connection between parts is a straight part with a length of 5mm to let filaments relax after flow focusing.

isfy $Q_1 = Q_2 \geq 10Q_3$, the inner fluid can be focused in the middle of the channel with a width of approximately $40\mu\text{m}$. The fluid injected into the two side branches is driven by one syringe pump unit (Low Pressure Syringe Pump neMESYS 290N) with a double syringe holder to achieve identical flow rates. As described in chapter 3, actin filaments are polymerized in monomer concentration $1\mu\text{M}$, and then 40X diluted in F-buffer with 45.5%(w/v) sucrose. The dilute suspension is injected in the middle whereas the F-buffer with 45.5%(w/v) sucrose is injected through the side branches.

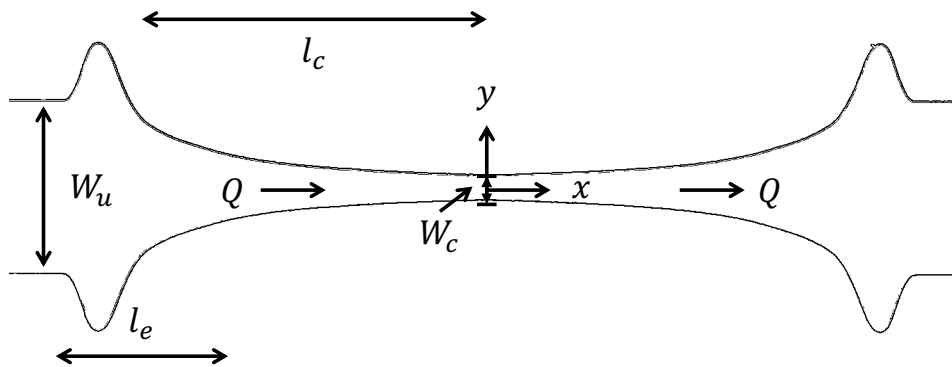


Figure 4.2: The top view of the optimized hyperbolic channel with the upstream part width $W_u = 800\mu\text{m}$, the contraction part width $W_c = 100\mu\text{m}$, the height of the channel $H = 100\mu\text{m}$, geometry parameters $n_1 = l_c/W_u = 2$ and $n_2 = 1$ (processed experimental image of microfluidic device).

The inlet and outlet parts of the hyperbolic channel have a width of W_u with an average velocity $\bar{u}_u = Q/(W_u H)$ and maximum velocity u_u at the centerline as shown in Fig. 4.2, H is the height of the channel. The throat has a width of W_c with a maximum velocity

u_c . In the converging part, there is a smooth transition region with a length of $l_e = n_2 W_u$, in which the extension rate varies linearly from zero to the maximum. After the transition regime, there is a region with a constant strain rate with a length of $l_c - l_e/2$, here $l_c = n_1 W_u$. n_1 and n_2 are the control parameters of channel geometry. The diverging part has a symmetric and opposite strain rate distribution. The shapes of the optimized hyperbolic channels vary depending on the height of the channel H , the width of inlet W_u , the width of contraction W_c , n_1 and n_2 . The configurations of several geometries are provided by Zografos Konstantinos from the group of Monica Oliveira at the University of Strathclyde, Glasgow, UK.

Hyperbolic channels have been optimized for different target velocity and strain rate profiles. Figure 4.3 shows the scaled velocity and scaled strain rate as a function of scaled displacement of an optimized hyperbolic channel with a smooth transition region, compared to those for a channel with a sharp transition region. After a constant velocity, there is a nonlinear acceleration in velocity providing a linear increase in strain rate, followed by a linear acceleration in velocity providing a constant positive strain rate. Similarly, the diverging part contains a constant negative strain rate and a linear increase in strain rate.

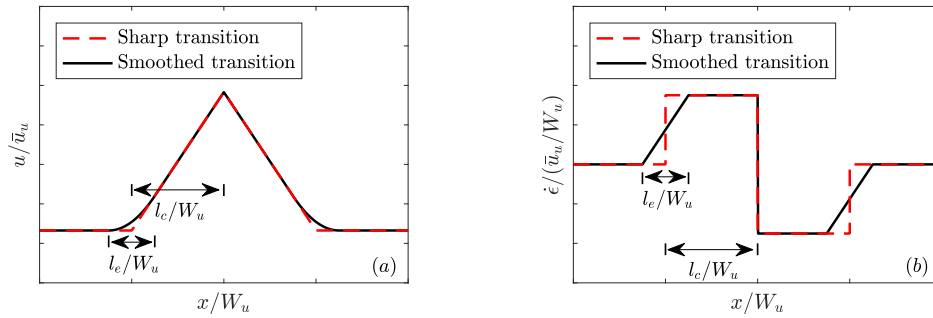


Figure 4.3: Ideal velocity profile (a) and extension rate profile (b) along the centreline of the flow

The velocity profile of the hyperbolic channel with smooth transitions as a function of position $u = g(x)$ is given by Eqn. (4.1). All symbols with tilde represent dimensionless velocities on the centerline, with $\tilde{x} = x/W_u$, $\tilde{u}_c = u_c/\bar{u}_u$ and $\tilde{u}_u = u_u/\bar{u}_u$, where \bar{u}_u is the average upstream velocity. The dimensionless parameters f_1 and f_2 are given by $f_1 = (\tilde{u}_c - \tilde{u}_u)/n_1$ and $f_2 = (\tilde{u}_c - \tilde{u}_u)/2n_1 n_2$ respectively.

$$\tilde{u} = \begin{cases} \tilde{u}_u & \text{if } \tilde{x} \leq -n_1 - \frac{n_2}{2} \\ f_2 \left[\tilde{x} + n_1 + \frac{n_2}{2} \right]^2 + \tilde{u}_u & \text{if } -n_1 - \frac{n_2}{2} < \tilde{x} < -n_1 + \frac{n_2}{2} \\ f_1 \tilde{x} + \tilde{u}_c & \text{if } -n_1 + \frac{n_2}{2} \leq \tilde{x} \leq 0 \\ -f_1 \tilde{x} + \tilde{u}_c & \text{if } 0 \leq \tilde{x} \leq n_1 - \frac{n_2}{2} \\ f_2 \left[\tilde{x} - n_1 - \frac{n_2}{2} \right]^2 + \tilde{u}_u & \text{if } n_1 - \frac{n_2}{2} \leq \tilde{x} \leq n_1 + \frac{n_2}{2} \\ \tilde{u}_u & \text{if } \tilde{x} \geq n_1 + \frac{n_2}{2} \end{cases} \quad (4.1)$$

The resulting normalized extension rate profiles corresponding to Eqn. (4.2) are given by $\dot{\epsilon} = \partial \tilde{u} / \partial \tilde{x}$

$$\dot{\epsilon} / (\tilde{u}_u / W_u) = \begin{cases} 0 & \text{if } \tilde{x} \leq -n_1 - \frac{n_2}{2} \\ 2f_2 \left[\tilde{x} + n_1 + \frac{n_2}{2} \right]^2 & \text{if } -n_1 - \frac{n_2}{2} < \tilde{x} < -n_1 + \frac{n_2}{2} \\ f_1 & \text{if } -n_1 + \frac{n_2}{2} \leq \tilde{x} \leq 0 \\ -f_1 & \text{if } 0 \leq \tilde{x} \leq n_1 - \frac{n_2}{2} \\ 2f_2 \left[\tilde{x} - n_1 - \frac{n_2}{2} \right]^2 & \text{if } n_1 - \frac{n_2}{2} \leq \tilde{x} \leq n_1 + \frac{n_2}{2} \\ 0 & \text{if } \tilde{x} \geq n_1 + \frac{n_2}{2} \end{cases} \quad (4.2)$$

Note that the length of the constant strain rate region is $l_{\text{homo}} = l_c - l_e/2$. Through varying the dimensions of the geometry and the flow rate Q , we can obtain extensional/compressive flows with different ranges of strain rates. Table 4.1 shows the dimensions of different optimized geometries and the corresponding parameters, like strain rate or residence time for a given flow rate $Q = 5.5 \text{ nl/s}$.

In our experiments, we will only use GeomA and GeomB. These geometries have the smallest u_c , which makes visual observations in the channel easier and together with a large l_{homo} this leads to long residence times. Furthermore they have the largest channel height and the shear occurring slightly above or below the mid-height of the channel can thus be neglected here.

Table 4.2 shows the actual geometries used in experiments. It can be seen that small deviations from the desired geometries occur during the lithography process, in particular the width of the constriction is typically slightly too large. This is due to multiple reasons in the experimental realization, the imperfection of the mask, the imperfect alignment of the UV light and the polymerization time of photoresists (Weibel et al., 2007). It is worth to note that in the following we use these real dimensions, the height and width upstream and in the constriction to calculate u_u and u_c and then to get the velocity profile along the centre streamline through Eqn. (4.1). To this purpose we use the formula of

	GeomA	GeomB	GeomC	GeomD
W_u (μm)	800	800	400	200
W_c (μm)	100	100	50	25
H (μm)	100	100	100	100
n_1	4	2	2	2
n_2	1	1	1	1
l_c (μm)	3200	1600	800	400
l_e (μm)	800	800	400	200
l_{homo} (μm)	2800	1200	600	300
Q (nl/s)	5.5	5.5	5.5	5.5
u_u ($\mu m/s$)	111.9	111.9	244.8	602.3
u_c ($\mu m/s$)	1152.9	1152.9	1367.9	2273.6
$\dot{\epsilon}$ (s^{-1})	0.325	0.651	1.404	4.178
$t_{\text{residence}}$ (s)	2.42	1.04	0.43	0.13

Table 4.1: The dimensions of different optimized hyperbolic channels.

White (White and Corfield, 2006) for flow in rectangular channels. Note that the velocity profiles for the real experimental geometries differ only slightly from the target profiles of the optimized geometries. PIV measurements are planned to confirm the agreement between the calculated velocity profile and the real flow velocity on the center line, but we expect good agreement to be found. Note that later on we will show an example of a comparison between the calculated flow velocity and data obtained from a filament transported in a channel, and good agreement is obtained (see Fig. 4.8). In the following we will refer to the calculated velocity profile simply as velocity profile.

	A2	B1	B2	B3
W_u	789.4 μm	784.5 μm	789.6 μm	787.4 μm
W_c	107.7 μm	104.6 μm	106.6 μm	105.5 μm
H	100.2 μm	97.5 μm	99.5 μm	97.5 μm

Table 4.2: The actual dimensions of the experimental geometries.

4.2.2 Experimental Implementation

Most of the previous studies on the dynamics of flexible particles in extensional or compressive micro-flows (Mancuso and Ristenpart, 2017; Strelnikova et al., 2017) have been performed with a fast camera and thus a short exposure time and at a fixed location of the channel. However, the imaging of our actin filaments requires a long exposure time, up to fifty milliseconds, to insure a good image quality. In addition, we want to be able to follow our filaments during transport in the hyperbolic channels. In order to observe the filament dynamics without blur, caused by the long exposure time, a precise tracking system is necessary and important. As we did in chapter 3, we continue to use a motor-

ized stage to track the filaments. However, tracking a filament transported in a velocity field with an acceleration and a deceleration is much more demanding, especially when the range of velocities spans from $\mu\text{m/s}$ to mm/s .

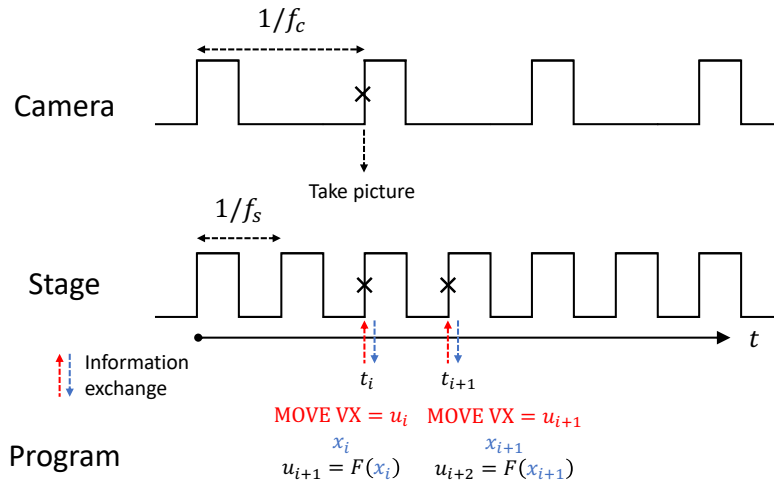


Figure 4.4: The diagram of pulses and information exchange of the Labview program.

In the following we describe the Labview program we wrote to control the stage moving with an acceleration and deceleration as closely as possible to the flow velocity of the centre streamline at the mid-height of the channel. The main challenge is to optimize the signals to be sent to the stage, taking into account the limitations of the experimental system. The tracking method has been developed in cooperation with the lab engineer Thierry Darnige and Joana Fidalgo, PhD student at University of Strathclyde.

The basic principle of the Labview program is shown in Figure 4.4. The Labview program sends synchronized signals to the camera with a frequency of $f_c = 10\text{Hz}$ and to the stage with a frequency of $f_s = 20\text{Hz}$. At each time step t_i , the camera takes a picture when receiving the pulse signal. When the signal is received by the stage controller, the stage controller commands the stage to move with a certain velocity u_i , calculated based on the stage position at the previous time step. Meanwhile, the stage sends feedback of the current position x_i , which is then used to calculate u_{i+1} , the velocity of the stage at the next time step.

Now we describe how to get the function $u = F(x)$ which is used to calculate the velocities from the stage displacements. A piecewise linear function $\tilde{F}(x)$ can be first derived from the flow velocity function given by Eqn. (4.1). The piecewise linear function needs to have more points during the transition regime since the velocity is not linear. It turns out that it is not sufficient to use the piecewise linear function directly derived from the flow velocity profile, as experimental constraints need to be taken into account. To this respect a self-written Mathematica code, considering a software delay of $1/f_s$, a hardware delay $\approx 8\text{ms}$ and the discrete nature of the stage speed, is used to simulate the movement of the stage taking into account all experimental constraints mentioned above.

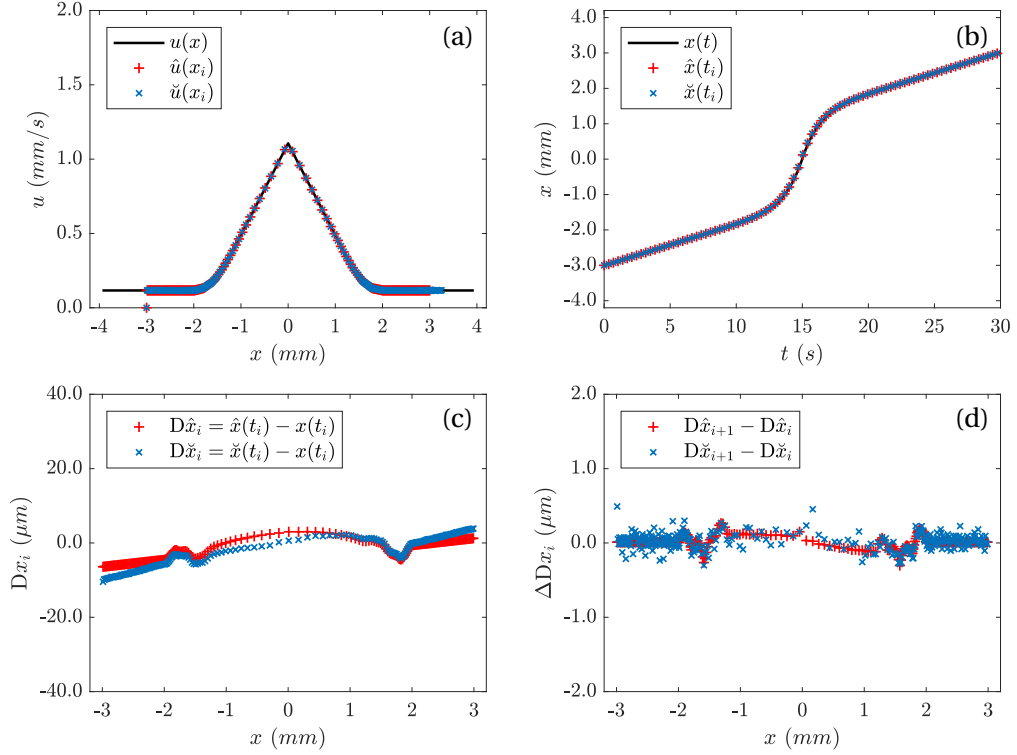


Figure 4.5: (a) Comparison between flow velocity $u(x)$ (black line), Mathematica code simulated stage velocity $\hat{u}(x_i)$ (red "+") and actual velocity of the stage $\check{u}(x_i)$ (blue "x"). (b) Comparison between flow displacement $x(t)$ (black line), Mathematica code simulated stage displacement $\hat{x}(t_i)$ (red "+") and actual displacement of the stage $\check{x}(t_i)$ (blue "x"). (c): The difference in displacement Dx between the flow and predicted stage motion (red "+") as well as the difference between flow and actual stage motion (blue "x"). (d): Image blur during exposure time due to the velocity difference between the flow and predicted stage motion (red "+") and actual stage motion (blue "x").

Hence we have the theoretical flow velocity $u(x)$ and Mathematica code simulated stage velocity \hat{u}_i as a function of position. We also have the time dependent displacement of the flow $x(t)$ and the simulated stage displacement $\hat{x}(t_i)$. For the flow, the displacement as a function of time is obtained through solving the ordinary differential equation $\dot{x} = g(x)$ with the initial condition $x(t = 0) = x_0$, which is the starting point of the stage. $D\hat{x}(t_i) = \hat{x}(t_i) - x(t_i)$ gives the difference in displacement between flow and simulated stage at the time step t_i . The image blur during the exposure time $\delta t = 50\text{ms}$ due to the velocity differences is given by $D\hat{x}(t_{i+1}) - D\hat{x}(t_i) = (\hat{x}(t_{i+1}) - x(t_{i+1})) - (\hat{x}(t_i) - x(t_i))$, which is the difference in displacement between flow and simulated stage during the time $t \in [t_i, t_{i+1}]$. Note that the frequency of the stage signal is 20Hz . While a small difference in displacement is necessary to keep the filament in the image frame, a small difference in velocity is required to keep the blur on the image small. Hence the Mathematica code minimizes the difference in displacement Dx as well as the image blur ΔDx_i to get the good approximation of the function $F(x)$.

We can measure the actual movement of the stage $\check{x}(t_i)$ using the good approximation of

$F(x)$ and the Labview program. The comparison between flow and the actual movement of the stage is used to verify the simulation of the moving stage as shown in Fig. 4.5. Fig. 4.5(a)&(b) show the actual velocity and displacement of the stage compared to Mathematica code simulated stage and flow. Fig.4.5-(c)&(d) show the differences in displacement and the image blur between simulated stage, actual moving stage and flow.

Manual adjustments can be made to the tracking program when tracking filaments transported in the channel. These small adjustments might be necessary due to small differences between the real flow profile and the calculated flow profile used to optimize the tracking program.

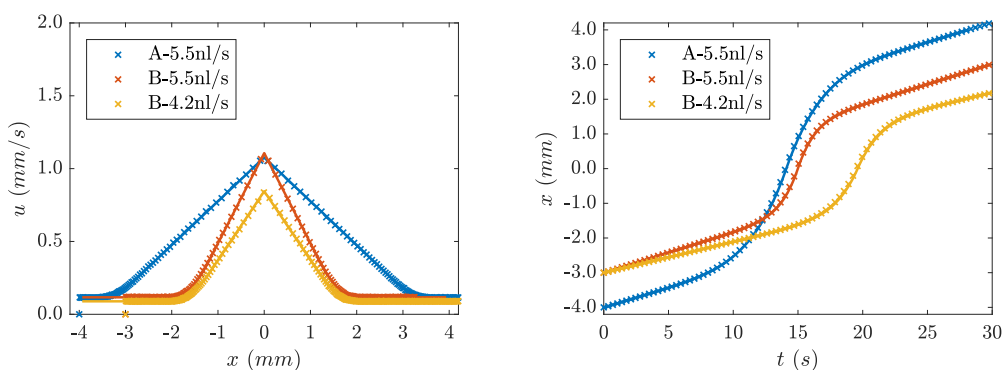


Figure 4.6: (Left): Velocity as a function of position. (Right): Displacement as a function of time. The markers represent the real movement of the stage, and the lines are the corresponding calculated flow profiles. Capital letters represent different geometries as shown in table 4.1.

Fig. 4.6 shows real stage movements compared to flow profiles for different channel geometries and flow rates as used in the following. Good agreement is observed.

Using the hyperbolic channels together with the flow focussing and the Labview tracking program, we can now directly observe actin filaments as they are transported in hyperbolic flow in very well controlled flow conditions. Filaments experience linearly varying strain as well as constant extension and compression rates in different parts of the channel.

4.3 Filament dynamics

4.3.1 Experimental observations

The configurational dynamics of three filaments with different contour lengths as they are transported in hyperbolic channels are shown in Fig. 4.7. The lengths are $L_{(a)} = 12.2\mu\text{m}$, $L_{(b)} = 27.4\mu\text{m}$ and $L_{(c)} = 57.8\mu\text{m}$. The maximum strain rates they experience are $\dot{\epsilon}_{(a)} = 0.34\text{s}^{-1}$, $\dot{\epsilon}_{(b)} = 0.61\text{s}^{-1}$, $\dot{\epsilon}_{(c)} = 0.65\text{s}^{-1}$.

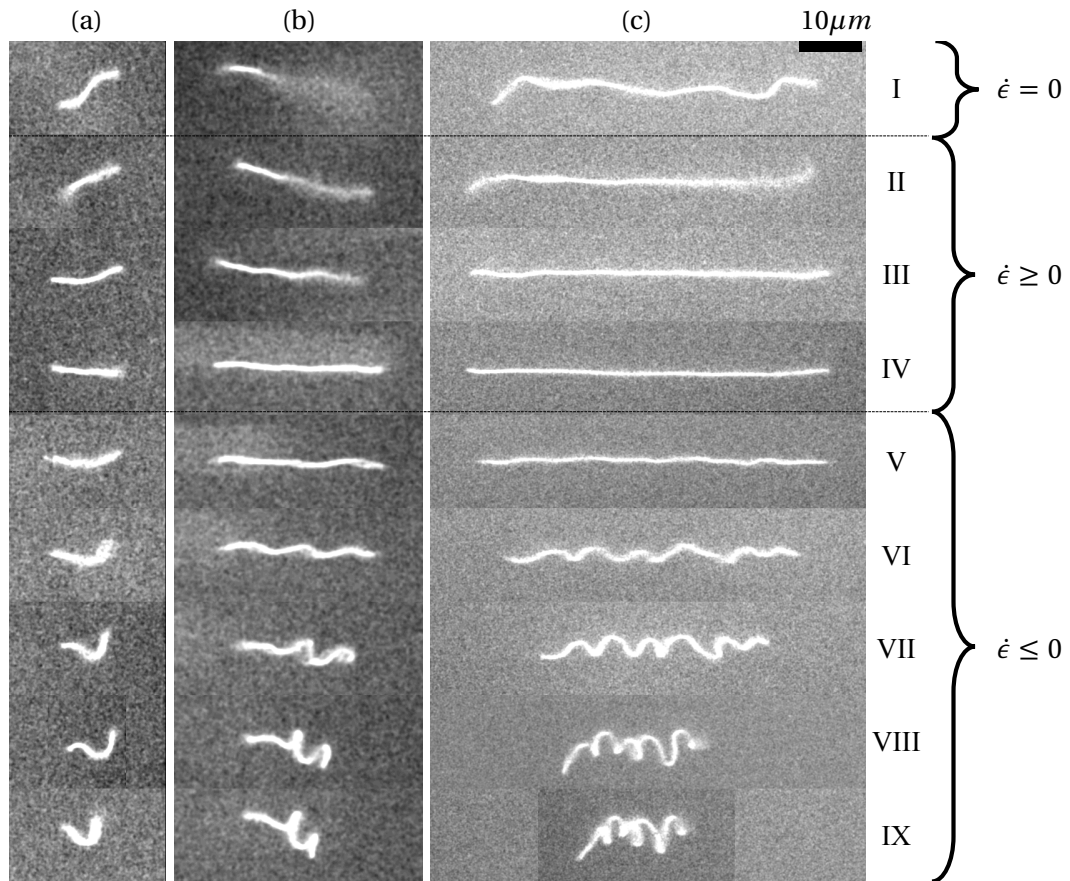


Figure 4.7: The temporal configurations of three different filaments in hyperbolic channels. The lengths are $12.2\mu m$, $27.4\mu m$, $57.8\mu m$ respectively. The maximum strain rates they experience are $0.34s^{-1}$, $0.61s^{-1}$, $0.65s^{-1}$ respectively. The governing parameter $\bar{\mu}/c$ they experiences during maximum strain rate are 1.1×10^3 , 4.5×10^4 , 8.8×10^5 respectively. Positive strain rate represents extensional flow, negative strain rate represents compressive flow.

From top to bottom, as Roman numbers increase, the filaments are transported through regions without strain, extensional flow and compressive flow. The filaments fluctuate or rotate freely in the region without strain (I). They are stretched by the flow leading to a suppression of fluctuations and an orientation towards the flow direction while the strain rate increases linearly (II, III) until fully stretched and aligned filaments are observed in the region of maximum homogeneous extension (IV). Different buckling modes (V, VI) are observed in the region of maximum homogeneous compression followed by increased bending and coiling while the filaments continue to be compressed as can be seen in rows (VII, VIII, IX).

During filament transport, Brownian fluctuation occur in three dimensions, and our observations are the projection of a three dimensional shape into the thin layer of the focal plane. For example, the first image of the snapshots (b) shows strong fluctuations out of the focal plane. However, as the filaments enter the extensional flow region, viscous

forces stretch the filaments and thermal fluctuations become suppressed. The whole filament then lies inside the focal plane.

Fig. 4.8 shows the snapshots of a long filament and the corresponding quantitative analysis. The actual velocity of the filaments while transported in the flow is calculated based on the displacement of the center of mass (Fig. 4.8 (a)). The end to end distance L_{ee} and the transverse amplitude of fluctuations a_{\perp} are used to quantify the evolving shape over time. The transverse amplitude of fluctuations a_{\perp} is measured as shown in Fig. 4.9. Note that the origin and physical meaning of these measured quantities are very different in the extensional part and in the compressive part as will be discussed below. At the beginning of the hyperbolic channel, the filament fluctuates freely and plateau values are observed for the scaled transverse fluctuations a_{\perp}/L and the scaled end to end distance L_{ee}/L (Fig. 4.8 (b)). As the filament enters the extensional flow, fluctuations start to be suppressed, as can be seen by the decrease of a_{\perp}/L and the increase in L_{ee}/L with

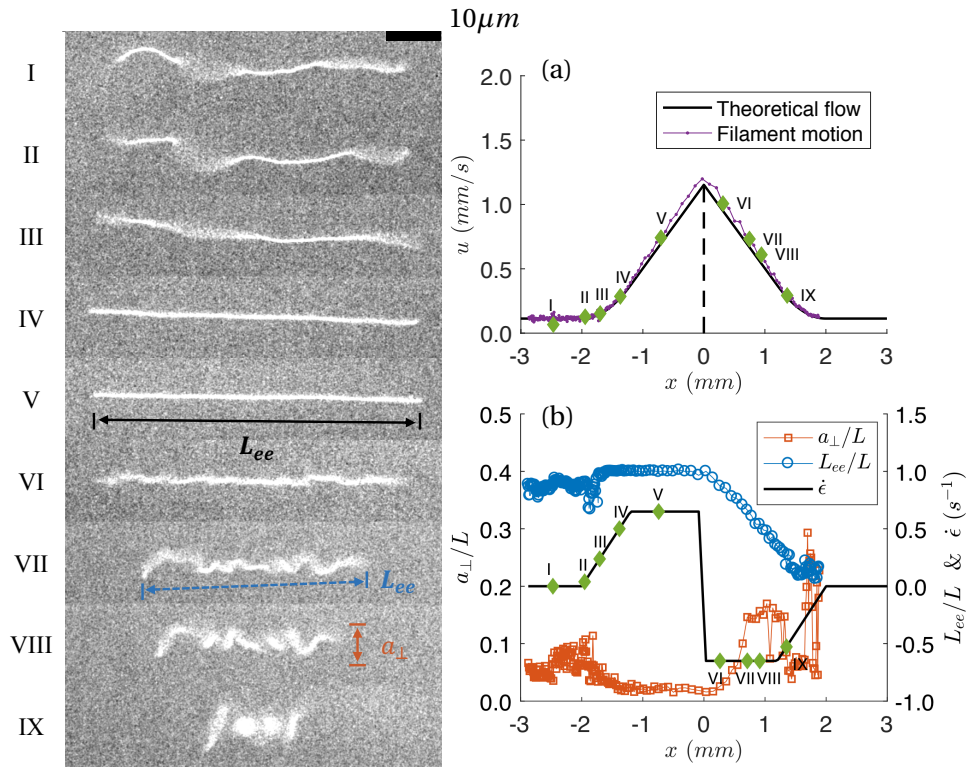


Figure 4.8: The temporal configurations of a filament in a hyperbolic channel and the corresponding measured quantities. (a) Comparison of velocities between calculated flow profile and actual velocity of the filament. (b) Evolution of the parameters a_{\perp}/L and L_{ee}/L as well as the strain rate.

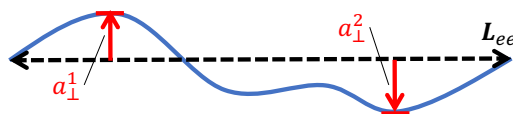


Figure 4.9: Measurement of the transverse amplitude a_{\perp} .

position until constant values are obtained again when the filament enters the region of constant strain rate. After crossing the throat of the channel, the filament performs buckling with high modes under homogeneous compression. Here the decrease of L_{ee}/L and the increase of a_{\perp}/L are measures of the filament deformation. The filament continues to be deformed and to coil in the following region of non-homogeneous compression. Note that the measurements of a_{\perp}/L are very noisy due to the three dimensional nature of the filament shapes.

Based on these observations and analyses, two interesting questions can be asked. How are transverse Brownian fluctuations suppressed by extensional flow and what are the characteristics of the deformed filament shapes formed in the compressive flow. These questions will be addressed in the following sections.

4.3.2 Suppression of Brownian fluctuations in extensional flow

In the extensional regime, $\dot{\epsilon} > 0$, there are two important forces at play: Brownian forces $\sim k_B T/L$ and viscous drag forces $\sim 2\pi\mu\dot{\epsilon}L^2/c$. Let's define the Peclet number P_e to be the ratio between Brownian and viscous forces, $P_e = 2\pi\mu\dot{\epsilon}_m L^3/k_B Tc$. Fig. 4.10-(left) shows $\langle L_{ee}/L \rangle$ as a function of the Peclet number. Here, symbols correspond to average values over the period where each filament experiences homogeneous extension (regime V Fig. 4.8(b)). Fig. 4.10-(left) shows that for most of our experiments $\langle L_{ee}/L \rangle$ has reached one and within our experimental resolution all filaments appear completely stretched. Only for one data point $\langle L_{ee}/L \rangle$ has not yet reached one. At the current stage we can thus not precisely determine the suppression of thermal fluctuations with increasing P_e number. More experiments, at smaller extension rates and also further analysis in the regime with increasing strain rate are planned. Another possibility is to look at the average of the transverse fluctuations (Fig. 4.10-(right)). However, a large scatter of data is observed, making a conclusion is difficult at this stage.

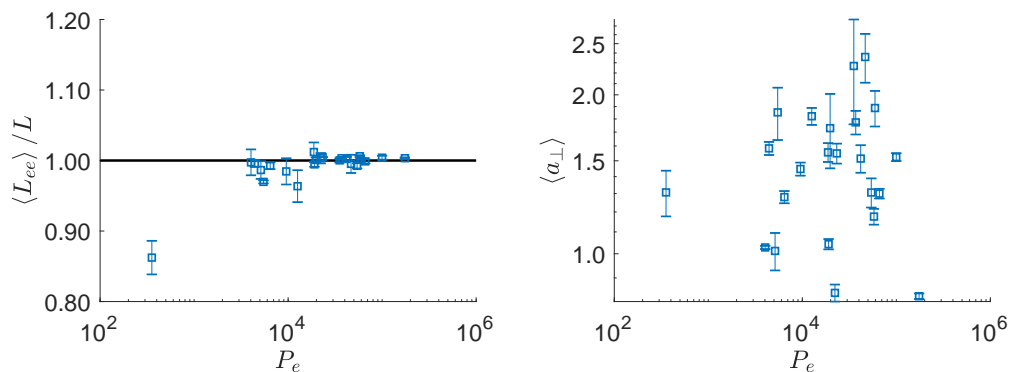


Figure 4.10: (left): The average scaled end to end distance as a function of Peclet number. (right): The average amplitude of transverse fluctuations as a function of Peclet number.

We now attempt to compare our preliminary data to findings in the literature. The

stretching of a flexible Brownian filament in an elongational flow has first been characterized in the work of (Kantsler and Goldstein, 2012) theoretically and experimentally using actin filaments at stagnation points. Numerical verification followed in the work of (Harishankar, 2009). Both groups introduce the dimensionless group Σ that is a ratio of tensile forces to elastic force, defined as

$$\Sigma = \frac{2\mu\dot{\epsilon}L^4}{\pi^3 Bc} \quad (4.3)$$

and which is proportional to our elasto-viscous number through $\Sigma = \bar{\mu}/4\pi^4 c$. The scaled filament end fluctuation variance $\overline{V_e \ell_p}/L^3$ is used to quantify the Brownian fluctuations. More details can be found in Appendix A. Here we only present a comparison between the different literature results and our data as shown in Fig. 4.11. Increasing flow strength leads to larger tension along the filaments, resulting in smaller amplitudes of the end point fluctuations. The work by (Kantsler and Goldstein, 2012) and (Harishankar, 2009) show a similar trend but there is a difference of the order of $O(10^1)$ in the scaled filament end point fluctuations, which requires further verification. Our data seem to roughly follow the overall trend, but the scatter of the data makes a clear statement difficult at this stage. It is worth to note that our experiments are performed at higher tensions compared to the experiments by (Kantsler and Goldstein, 2012) and might thus represent an interesting complementation of their observations. Further experiments and analysis are planned.

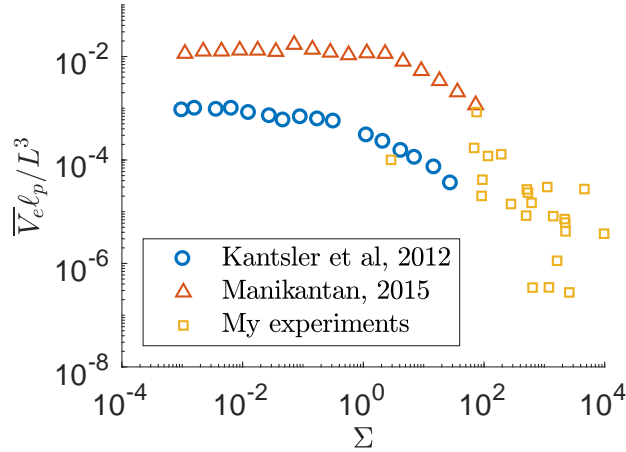


Figure 4.11: Scaled filament end point fluctuations as a function of scaled tension.

4.3.3 Buckling and helical coiling under compression

After crossing the throat of the channel, the filaments enter the compressive flow region, $\dot{\epsilon} < 0$, and filaments start to experience compressive flow. When viscous forces acting

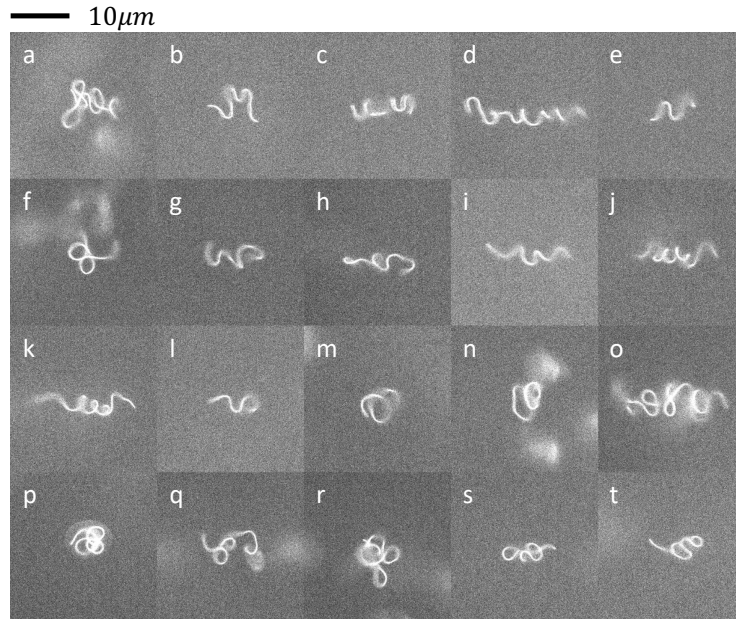


Figure 4.12: Complex three dimension coiling structures of different filaments under compression. Brownian fluctuations and different in lengths and strain rates make the configurations are diverse and complex.

on the filaments overcome its bending resistance, structural instabilities are observed as shown in Fig. 4.7(VI). From linear stability analysis described in chapter 1.2.1, we know that when $\bar{\mu}/c$ crosses successive thresholds, filaments can buckle with increasing buckling modes. Here, once buckling has occurred filaments continue to be transported in compressive flow and viscous forces continue to deform the filaments. Precise visual inspection (Fig. 4.7(VII-IX)) reveals that the formed structures represent three dimensional shapes, that correspond in most cases to helical structures. It is remarkable that a simple straining flow can transform a mostly two dimensional object into a three dimensional object with a chiral structure. Such helix formation has indeed been predicted numerically for flexible and Brownian filaments in a non-homogeneous compressive flow (Chelakkot et al., 2012) but has to our knowledge not yet been identified in experiments. Fig. 4.12 shows the complex shapes observed for different filaments in the last parts of the compressive flow region. Different parts of one filament can form helix structures with opposite chiralities, that together with Brownian fluctuations can lead to complex coil structures and even knots. Fig. 4.12-(d,e,k,q) show clearly partial or complete helical structures. Fig. 4.12-(a,o,p,r) show complex shapes for very long and thus very flexible filaments. Fig. 4.12-(p) shows an example of a filament that has spontaneously formed a knot. Numerical simulations have predicted that very flexible filaments can form knots in steady shear flow, however only for very specific initial conditions (Kuei et al., 2015). To our knowledge, once again such a knot formation has not been observed experimentally before. We are currently characterizing the properties of the formed shapes as a function of the control parameters of the system in more detail.

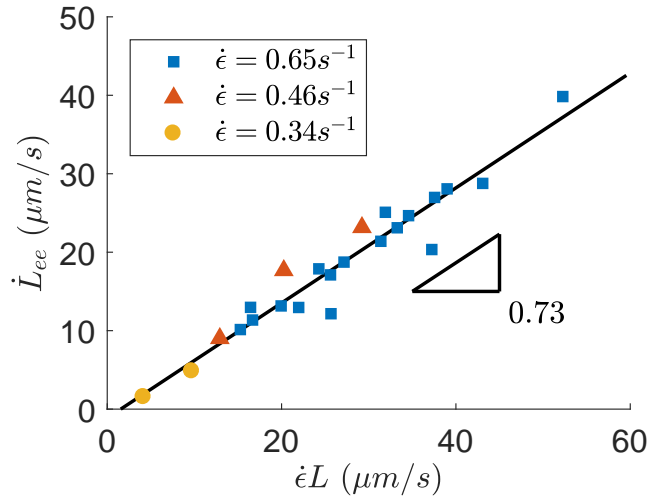


Figure 4.13: The time derivative of the end to end distance as function of $\dot{\epsilon}L$ in the homogeneous compression part of the channel.

During the process of buckling and coiling we can measure the time variation of the end to end distance. As shown in Fig 4.13, \dot{L}_{ee} is proportional to $\dot{\epsilon}L$, which is the relative velocity between the two fluid elements situated at the two ends of a filament. A slope of 1 would correspond to a deformation of the filament by the flow without any resistance. The slope 0.73 shows thus the ability to resist viscous forces after buckling and during the process of coiling. The exact meaning of this value still needs to be understood.

4.4 Summary

In this chapter, we used an optimized hyperbolic channel to implement a pure staining flow in a microfluidic device. Our aim was to obtain constant strain rates together with long residence times. We built an experimental set-up where a microfluidic flow geometry with a very well controlled flow profile has been combined with a sophisticated tracking algorithm. A Labview program controls the motorized stage to follow as precisely as possible the experimental flow field and thus allows us to follow individual filaments during transport in the hyperbolic contraction and expansion device. Note that a linear straining flow requires linear increase/decrease of the flow velocity with channel position asking for specific requirements in the programming of the stage displacement.

With our set-up we have directly observed the dynamics of flexible Brownian filaments during their transport in an extensional and a compressive flow. We observed distinct dynamics for positive and negative strain rates. Under extension we observed filament stretching and suppression of thermal shape fluctuations. The time evolution of the observed configurations were quantitatively analyzed through the variation of the end to end distance L_{ee} and the amplitude of transverse fluctuations a_{\perp} . We analyzed our preliminary data as a function of a Peclet number and we have also compared them to

previous results in the literature represented as a function of a dimensionless tension Σ (Kantsler and Goldstein, 2012) (Harishankar, 2009). Our experimental results seem to follow the same trend as observed in literature, but for the moment the large scatter in our measurements does not permit a clear conclusion. Further experiments and analysis is planned.

Under compression high buckling modes of the flexible filaments have been observed. During transport through the compressive flow regime we have discovered the formation of three dimensional structures, often with a helical shape. This transition from a quasi two dimensional shape to a three dimensional object with chirality had been predicted numerically (Chelakkot et al., 2012), but had not been identified in experiments yet. In addition, we have also observed the formation of knots. The question whether in linear flows knots can be formed by flexible filaments is an open question in the community and only recently has such a knot formation been predicted by numerical simulations, using very specific initial conditions (Kuei et al., 2015). The analysis of the precise properties of these structures is still ongoing.

4.5 Discussion and outlook

In this chapter we have described our results on the dynamics of flexible Brownian filaments in optimized hyperbolic channels. Several questions remain open on the dynamics under extension as well as under compression.

First, our results on the suppression of Brownian fluctuations under shear are in reasonable agreement with literature results, but a clearer understanding still needs to be found. In particular, the results from literature do not seem to agree with each other. While results from theoretical and experimental work in (Kantsler and Goldstein, 2012) are in good agreements, recent theoretical and numerical results given by (Harishankar, 2009) have a difference in the dimensionless fluctuation amplitude $\bar{V}_e \ell_p / L^3$ with nearly an order of magnitude. For the moment the scatter on our experimental results does not allow us to confirm either of the two models, but we hope to get more precise information by performing additional experiments in the future. In addition, most of our experiments are in a slightly different range of control parameters compared to previous experiments and could thus be an interesting addition to the existing results.

While our observations reveal very clearly the formation of three dimensional helical structures in the compressive part of the flow, the mechanism of this transition remains still to be understood. Numerical work by (Chelakkot et al., 2012) attributes the formation of the three dimensional structures to the existence of Brownian fluctuations and a non-homogeneous compression field (Fig. 4.14(A)). However, experimental work by (Mercader et al., 2010) seem to show the formation of a helical structure of a millimetric filament entering a compressive flow in a circular flow device (Fig. 4.14(B)). The authors

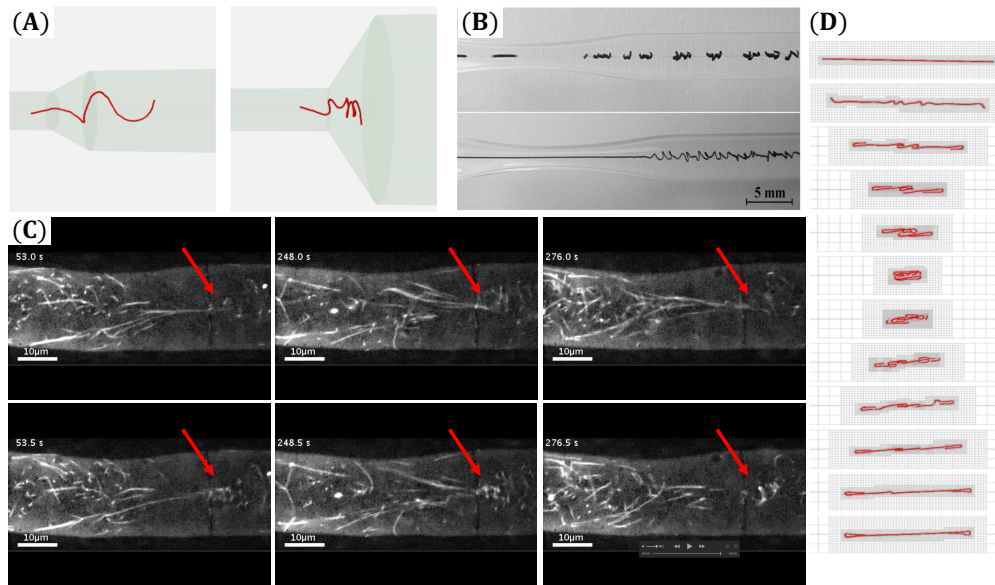


Figure 4.14: **(A)**: Numerical study of flow induced helical coiling of Brownian filaments in a diverging channel (Chelakkot et al., 2012). **(B)**: The solidification of synthetic wet-spun fibers in converging and diverging channel (Mercader et al., 2010). **(C)**: Buckling of microtubules with helical structure when they passing through a septal pore (Pieuchot et al., 2015). **(D)**: Complex configuration in three dimension of a long flexible filament in shear flow (Nguyen and Fauci, 2014).

do not discuss the helix formation, but visual inspection of their images seems to indicate structures similar to those observed in our experiments. Brownian fluctuations thus seem not to be a necessary ingredient. A common point between the numerical simulations and the experimental geometry is the three dimensional nature of the compressive flow. It might be possible that in such a flow transversal buckling modes couple in three dimensions (Shelley et al.) leading to the observed structures. For a better understanding a three dimensional linear stability analysis would need to be performed. In our flow geometry the three dimensional nature of the flow might result from the shear component present in the direction of the height of the channel that might be experienced by parts of the filaments that deform away from the centerline. Let us also note, that even under shear very flexible filaments seem to form three dimensional structures as can be observed in the numerical simulations of (Nguyen and Fauci, 2014) (Fig. 4.14(D)). And finally let us point out that the situation studied here as a model experiment has relevance to biological applications and might help to understand the behavior of microtubules passing through septal pores when cytoplasm flows directionally from cell to cell (Pieuchot et al., 2015) (Fig. 4.14(C)).

References

- Brosseau, Q., Vrignon, J., and Baret, J.-C. Microfluidic dynamic interfacial tensiometry (μ dit). *Soft matter*, 10(17):3066–3076, 2014.
- Chelakkot, R., Winkler, R. G., and Gompper, G. Flow-induced helical coiling of semi-flexible polymers in structured microchannels. *Physical review letters*, 109(17):178101, 2012.
- Galindo-Rosales, F. J., Alves, M., and Oliveira, M. S. Microdevices for extensional rheometry of low viscosity elastic liquids: a review. *Microfluidics and Nanofluidics*, 14(1-2): 1–19, 2013.
- Harishankar, M. *Bending, Buckling, Tumbling, Trapping: Viscous Dynamics of Elastic Filaments*. PhD thesis, University of California, San Diego, 2009.
- Haward, S. Microfluidic extensional rheometry using stagnation point flow. *Biomicrofluidics*, 10(4):043401, 2016.
- Kantsler, V. and Goldstein, R. E. Fluctuations, dynamics, and the stretch-coil transition of single actin filaments in extensional flows. *Physical review letters*, 108(3):038103, 2012.
- Kuei, S., Słowicka, A. M., Ekiel-Jezewska, M. L., Wajnryb, E., and Stone, H. A. Dynamics and topology of a flexible chain: knots in steady shear flow. *New Journal of Physics*, 17(5):053009, 2015.
- Mancuso, J. and Ristenpart, W. Stretching of red blood cells at high strain rates. *Physical Review Fluids*, 2(10):101101, 2017.
- Mercader, C., Lucas, A., Derré, A., Zakri, C., Moisan, S., Maugey, M., and Poulin, P. Kinetics of fiber solidification. *Proceedings of the National Academy of Sciences*, 2010.
- Nguyen, H. and Fauci, L. Hydrodynamics of diatom chains and semiflexible fibres. *Journal of The Royal Society Interface*, 11(96):20140314, 2014.
- Nunes, J. K., Constantin, H., and Stone, H. A. Microfluidic tailoring of the two-dimensional morphology of crimped microfibers. *Soft Matter*, 9(16):4227–4235, 2013.
- Oliveira, M., Rodd, L., McKinley, G., and Alves, M. Microfluid. nanofluid. 5 (6), 809 (2008). *CrossRef Google Scholar*.
- Pieuchot, L., Lai, J., Loh, R. A., Leong, F. Y., Chiam, K.-H., Stajich, J., and Jedd, G. Cellular subcompartments through cytoplasmic streaming. *Developmental cell*, 34(4):410–420, 2015.
- Quennouz, N., Shelley, M., du Roure, O., and Lindner, A. Transport and buckling dynamics of an elastic fibre in a viscous cellular flow. *Journal of Fluid Mechanics*, 769: 387–402, 2015.

- Rothstein, J. P. and McKinley, G. H. The axisymmetric contraction-expansion: the role of extensional rheology on vortex growth dynamics and the enhanced pressure drop. *Journal of non-newtonian fluid mechanics*, 98(1):33–63, 2001.
- Shelley, M. J., Lindner, A., Roure, O. D., and LIU, Y. personal communication.
- Strelnikova, N., Göllner, M., and Pfohl, T. Direct observation of alternating stretch-coil and coil-stretch transitions of semiflexible polymers in microstructured flow. *Macromolecular Chemistry and Physics*, 218(2):1600474, 2017.
- Weibel, D. B., DiLuzio, W. R., and Whitesides, G. M. Microfabrication meets microbiology. *Nature Reviews Microbiology*, 5(3):209, 2007.
- White, F. M. and Corfield, I. *Viscous fluid flow*, volume 3. McGraw-Hill New York, 2006.
- Zografos, K., Pimenta, F., Alves, M., and Oliveira, M. Microfluidic converging/diverging channels optimised for homogeneous extensional deformation. *Biomicrofluidics*, 10(4):043508, 2016.

Chapter 5

Actin filament suspensions

Contents

5.1 Introduction	82
5.2 Microfluidic rheometer	83
5.2.1 Microfluidic geometry	83
5.2.2 Interface detection	84
5.2.3 Y channel viscometer calibration using fluorescein	85
5.3 Monodisperse suspensions	85
5.3.1 A biochemical approach to fabricate monodisperse suspensions	85
5.3.2 Polymerization dynamics	86
5.4 Shear viscosities of actin suspensions	88
5.5 Summary and outlook	90
References	90

5.1 Introduction

After studying the dynamics of individual filaments in shear and straining flows, the next step is to study the rheological bulk properties of their suspensions, in order to understand the link between the microscopic structure and the macroscopic properties.

Little experimental work has investigated the rheology of dilute solutions of flexible fibers, as discussed in section 1.2.3, but a number of theoretical and numerical studies have been performed. For suspensions of Brownian rigid rods, increased alignment with the flow direction is expected as the Peclet number increases, leading to shear thinning of the viscosity (Saintillan and Shelley, 2013). No normal stress differences are expected for dilute suspensions of rigid fibers (Tornberg and Shelley, 2004).

For suspensions of flexible fibers the additional stresses exerted on the surrounding fluid (Batchelor, 1970) by the deformed fibers have been found numerically to lead to normal stress differences and shear thinning above the buckling threshold (Becker and Shelley, 2001; Tornberg and Shelley, 2004). No experimental verification of these predictions exist up to date. The main difficulty of such measurements is the limitation in resolution of experimental devices. Non-Newtonian effects are expected to be weak in the dilute regime and thus lie often outside of the resolution of experimental devices.

Following the work of (Batchelor, 1970; Becker and Shelley, 2001; Tornberg and Shelley, 2004), our collaborators Brato Chakrabarti and David Saintillan have calculated the contribution of the average extra stress over time $S = \int_0^L \mathbf{f}(s) \mathbf{r}(s) ds$ to the bulk stress tensor for the filament conformations obtained from their numerical simulation for flexible Brownian filaments in shear flow, discussed in chapter 3. The results for the first normal stress difference and the shear viscosity are showed in Fig. 5.1. A positive first normal stress difference and a shear thinning viscosity can be clearly seen from this figure. We have shown in chapter 3 the good agreement in filament dynamics between our experiments and the numerical simulations and we could thus expect a macroscopic response of our suspensions in agreement with the numerical results.

In this chapter we describe our first attempts at measuring shear viscosities of our suspensions in the dilute regime. Two main challenges need to be overcome. First, the filament length is the dominant parameter in varying the $\bar{\mu}$, the main control parameter of our system, as $\bar{\mu}$ is proportional to L^4 . It is thus essential to be able to work with monodisperse suspensions. Note that in all our previous studies we have investigated individual filament dynamics where it has been possible to determine the exact filament length by image processing for each filament studied. Working with a monodisperse suspensions was thus not necessary. Second, a measurement method with good resolution requiring only small amounts of sample needs to be implemented.

Here, we first test and calibrate a microfluidic rheometer, a Y channel, to be used as the measurement device. Then we develop a controllable and reliable protocol for fabricated

monodisperse suspension with given length distributions. Finally we present preliminary data on shear viscosities of filament suspensions.

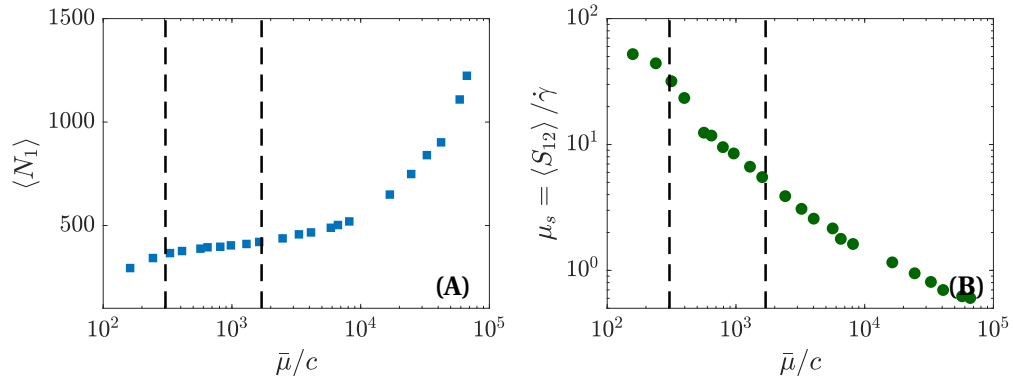


Figure 5.1: (A): First normal stress difference $\langle N_1 \rangle = \langle S_{11} - S_{22} \rangle$ and shear stress $\langle S_{12} \rangle$ as a function of $\bar{\mu}/c$. (B): Shear-viscosity μ_s as a function of $\bar{\mu}/c$ (Chakrabarti and Saintillan, in preparation).

5.2 Microfluidic rheometer

5.2.1 Microfluidic geometry

Here we opt to use an optical microfluidic viscometer Galambos and Forster (1998), a Y-channel to measure the viscosity of filament suspensions. The Y channel has a width of $600\mu m$ and a height of $100\mu m$, and the widths of the branches are half of the main branch. The method for measuring viscosities using the Y-channel requires to have a reference fluid with known viscosity and to be able to visually distinguish between the sample and the reference fluid. When the sample and the reference fluid are injected into the two arms of the Y-channel at the same flow rate Q , the viscosity ratio between sample and reference fluid can be approximated by the ratio of the occupied widths of the two fluids h_1/h_2 as shown in Eqn. (5.1).

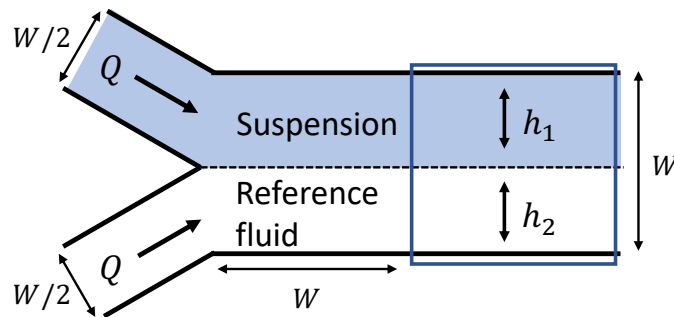


Figure 5.2: Sketch of the Y-channel with two co-flowing fluids driven by identical flow rates. The frame corresponds to the visual field of the camera.

$$1 = \frac{Q_1}{Q_2} = \frac{h_1 H \bar{U}_1}{h_2 H \bar{U}_2} = \frac{\Delta P H h_1 / \mu_2}{\Delta P H h_2 / \mu_1} \Rightarrow \frac{h_1}{h_2} = \frac{\mu_2}{\mu_1} \quad (5.1)$$

5.2.2 Interface detection

There are several ways to visualize the space occupied by the two fluids. One way is to use two immiscible fluids, but the presence of two immiscible fluids in the channel can cause instability in the flow due to different surface tension, and we have chosen not to work with this possibility. Another way is to use two miscible fluids but with distinct refractive index. This can for example be obtained by adding sucrose or other components, but the viscosity of the solution will also change. Finally, two miscible fluids can be used, but one of the fluids contains fluorescent molecules or particles. Under UV light, the interface between two fluids can then be easily detected due to the difference of intensities. The intensity profile across the width can be fitted with an error function (Gachelin et al., 2013) as shown in Eqn. (5.2). The error function accounts for the diffusion of the fluorescent molecules or particles. Depending on the size of the fluorescent molecules or particles and the flow rate, the interface width varies at the observation point, which is 0.6mm from the inlet of the main channel. The fitting parameter b gives the position of the interface as can be seen from the example shown in Fig. 5.3.

$$\text{Intensity} = a \operatorname{erf}\left(\frac{x-b}{c}\right) + d$$

$$\operatorname{erf}(x) = \frac{1}{\sqrt{\pi}} \int_{-x}^x e^{-t^2} dt \quad (5.2)$$

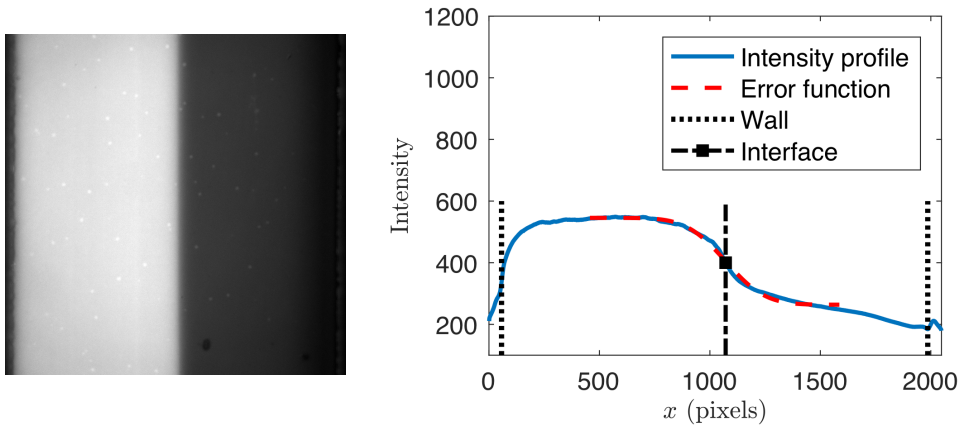


Figure 5.3: (left): Example of an image of co-flow of actin filament suspension (left part, fluorescent G-actin) and reference fluid (F-buffer, right part). (right): Detection of the interface through curve fitting of an error function to the intensity profile.

5.2.3 Y channel viscometer calibration using fluorescein

In order to measure the shear rate dependent viscosity of actin filament suspensions, we first calibrate the Y channel viscometer using water and a mixture of water and fluorescein. Note that the concentration of fluorescein is $0.2\text{g}/\text{mL}$ and the viscosities of two fluids can be regarded as equal. We thus expect a shear rate independent viscosity ratio $\mu_{\text{dye}}/\mu_{\text{nodye}} = 1$ between the two fluids. However, the diffusion of fluorescein causes an error in detecting the interface position at low flow rates.

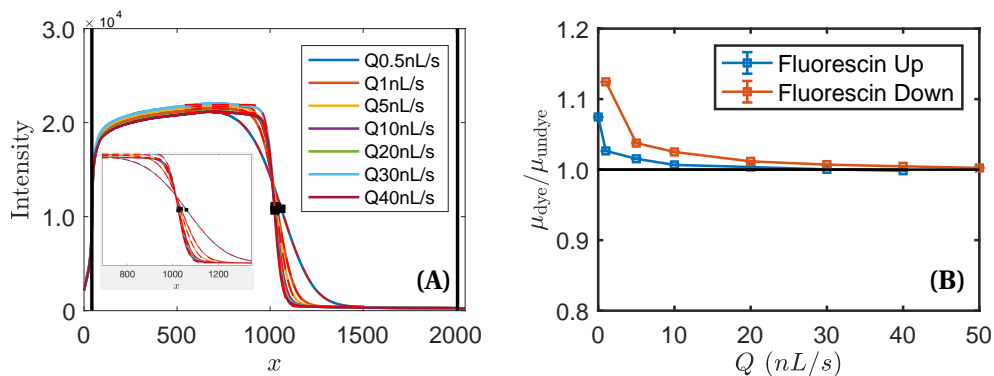


Figure 5.4: (A): The intensity profile between fluorescein solution (left part) and distilled water (right part) for different flow rates. The inset image is a zoom of the interface regime. (B): The apparent viscosity ratio between the two fluids.

Fig 5.4 shows the intensity profile of the co-flowing fluids and the apparent viscosity ratio with increasing flow rate. A non physical shear thinning behavior is observed in Fig 5.4. This behavior is not the result of a defect of the channel geometry as the same behavior is observed when the two inlet branches are inverted. It turns out that for small flow rates diffusion is too strong leading to an error in the detection of the interface position. We thus decided not to use fluorescein to dye one of the two fluids. Hence, we directly use Alexa 488 labeled G-actin to fabricate our actin filament suspensions. The size of the G-actin is quite large compare to fluoescin molecules, the error caused by diffusion can thus be ignored when detecting the interface.

5.3 Monodisperse suspensions

5.3.1 A biochemical approach to fabricate monodisperse suspensions

In the polymerization of actin monomers into filaments, the nucleation is the limiting step: when formed, a nucleus (3-4 monomers typically) elongates with a constant rate only determined by the concentration of the monomeric actin in solution. One consequence of this is that polymerization starts at different times for the different filaments and produces suspensions with very broad distribution of lengths. This is advantageous

when studying individual filaments as done in chapter 3 and 4 but prevents the fabrication of monodisperse suspensions. To overcome this issue, another strategy has to be developed. We took advantage of our collaboration with the group of Guillaume Romet Lemonne and Antoine Jégou at Institut Jacques Monod in Paris to use biochemical approaches to synchronize the onset of the polymerization in the suspension. Small fragments of stabilized actin filaments are used as nuclei from which elongation will start. These seeds are stabilized by a protein called spectrin and for this reason they are called 'spectrin-actin seeds' (Jégou et al., 2011; Niedermayer et al., 2012; Shekhar et al., 2015). They are kindly provided to us after purification by our collaborators. Figure 5.5 illustrates a filament polymerized directly from spectrin actin seed. Note that the size of spectrin-actin seed is small enough - around tens of nanometers - for the effect on the filament flexibility to be neglected.

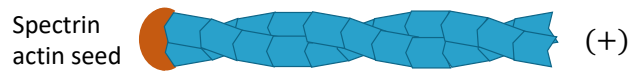


Figure 5.5: Sketch of a filament polymerized from a spectrin-actin seed.

If the concentration of monomeric actin $[G - actin] \geq 0.5\mu\text{M}$, spontaneous nucleation will occur in bulk which will broaden the distribution of lengths. Thus it is necessary to use another protein that prevents spontaneous nucleation so that only polymerization from seeds takes place. This protein, profilin, sequesters monomeric actin but dissociates from actin when polymerized. An excess of profilin is thus required and we usually use two or three times more profilin than actin. To avoid the influence of Phalloidin on the polymerization rate, non-fluorescent Phalloidin used to stabilize the filaments by preventing depolymerization, is added *after* polymerization is complete. For more details, one can refer to the protocol given in Appendix B. At the end, the concentration of filaments in the suspension is equal to the concentration of seeds and the length of the filaments is expected to be given by the ratio of monomeric actin concentration to the seeds concentration. The polymerization will stop when the concentration of monomeric actin is lower than $0.1\mu\text{M}$.

5.3.2 Polymerization dynamics

The growth rate of filaments is proportional to the concentration of monomeric actin, which decreases during the polymerization. Supposing C is the concentration of actin monomers, C_{seed} is the concentration of spectrin actin seed. The time derivation of monomer concentration C and the monomer number associated on one filament N from the spectrin actin seed is give by

$$\begin{cases} \dot{C} = -k_{\text{on}}(C - C_{\text{off}}) \times C_{\text{seed}} \\ C(0) = C_0 \\ \dot{N} = k_{\text{on}}(C - C_{\text{off}}) \\ N(0) = 0 \end{cases} \quad (5.3)$$

Here, C_0 is the initial concentration of monomers, $k_{\text{on}} = 10$ is the association rate of monomers at the barbed end and $C_{\text{off}} = 0.1$ accounts for concentration increase due to much slower dissociation of monomers at the barbed end. A filament of length $1\mu\text{m}$ consists of 370 G-actin monomers, therefore the filament with N monomers has a contour length of $N/370\mu\text{m}$. Figure 5.6 shows the time evolution of monomer consumption and length growth of a filaments polymerized from the spectrin seed as predicted by Eqn. (5.3) and corresponding experimental protocol.

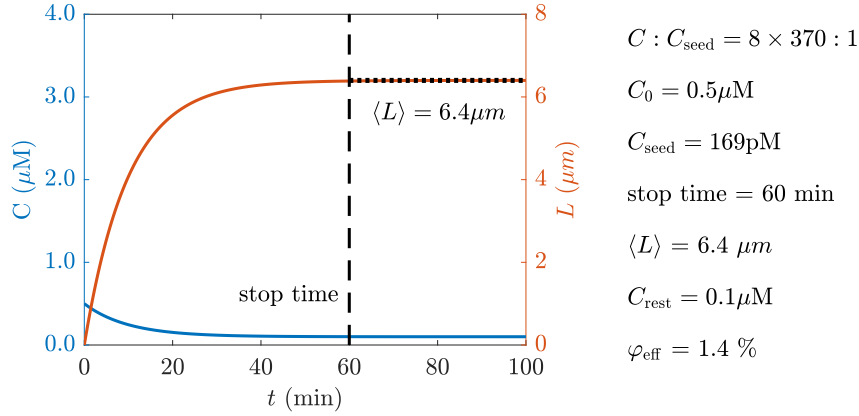


Figure 5.6: The time evolution of monomer concentration and average length of suspension and the corresponding protocol.

Here, C_{rest} is the concentration of residual monomers, φ_{eff} is the effective volume fraction calculated based on the assumption that each filament occupies the sphere with a diameter of average length of filaments. $\varphi_{\text{eff}} = nV_i/V_f$, n is the number of the filaments, $V_i = 4\pi(L/2)^3/3$ is the occupied volume of each filament, V_f is the total volume of the suspension. To measure the actual length of filaments in suspension, we use optical microscopy. As actin filaments are brownian and microscopy only allows imaging in two dimensions, it is necessary to confine filaments in 2-D before observations. To do so, we use electrostatic interaction between actin filaments and polylysine-grafted glass coverslip. This is a simple and easy way to visualize the whole body of the filaments. The contour length of a filament lying on the cover-slip is extracted from fluorescent image through a lab-written MATLAB code as mentioned in chapter 2.

Experimentally, we observed however a difference between the predicted average length and the one obtained in the experiments. The concentrations of different proteins have

	Suspension of short filaments	Suspension of long filaments	Suspension of long filaments
C_0	$0.5 \mu\text{M}$	$2 \mu\text{M}$	$3 \mu\text{M}$
C_{seed}	169M	270pM	270pM
C_{profilin}	\emptyset	$5 \mu\text{M}$	$7.5 \mu\text{M}$
Polymerization time	60min	60min	60min
Average $\langle L \rangle$	$4.3 \mu\text{m}$	$9.6 \mu\text{m}$	$15.1 \mu\text{m}$
φ_{eff}	0.4%	7.5%	23.9%

Table 5.1: Preparation of different suspensions: Composition of the solution, average length obtained and volumic fraction.

thus been adapted and are detailed in table 5.1. Figures 5.7,5.8,5.9 is a typical image showing filaments produced by the different protocols described in table 5.1 and the corresponding length distributions.

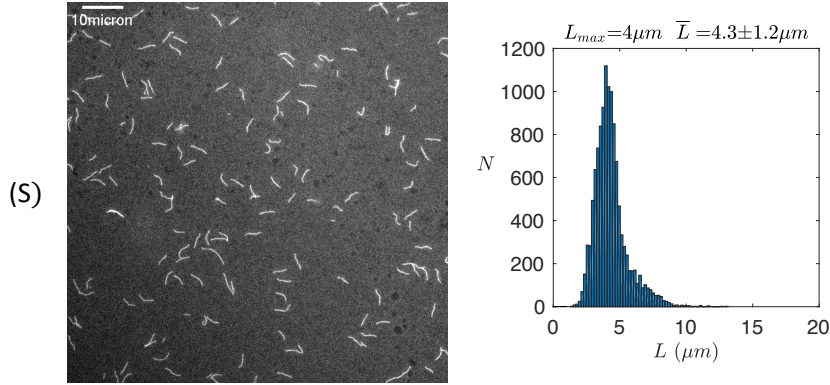


Figure 5.7: Filaments fabricated for short suspension and its length distribution.

5.4 Shear viscosities of actin suspensions

For measuring the shear viscosities of filament suspensions, we use F-buffer as the reference fluid whose viscosity is identical to the viscosity of water $\mu_{\text{eff}} = 1 \text{ mPa} \cdot \text{s}$. First measurements have been performed with a semi-dilute suspensions, without good length control and are showed here as an example. The monomer concentration at the beginning of the polymerization was $5 \mu\text{M}$. Figure 5.10 shows the visual drift of the interface with increasing flow rate between the reference fluid and the semi-dilute actin filament suspension, indicating a decrease in viscosity as the flow rate increases. The viscosity of this semi-dilute suspension as a function of the average shear rate $\langle \dot{\gamma} \rangle = Q/(WH^2)$ is showed in Fig. 5.11(A).

Due to the limit of time, systematic experiments on the shear viscosities of actin filament suspensions with different length distributions and volume fractions could not

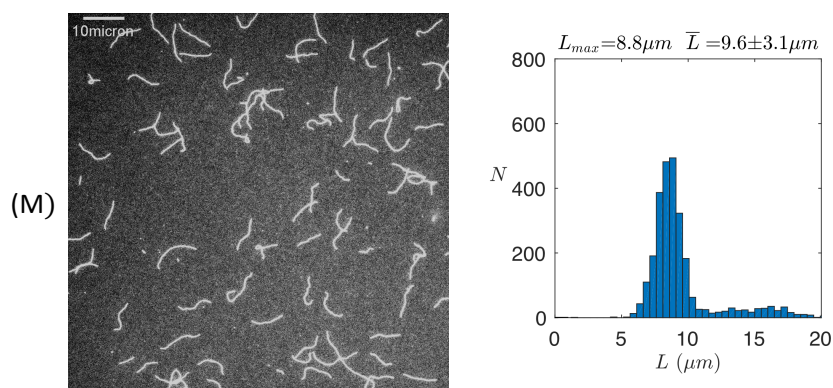


Figure 5.8: Filaments fabricated for medium suspension and its length distribution.

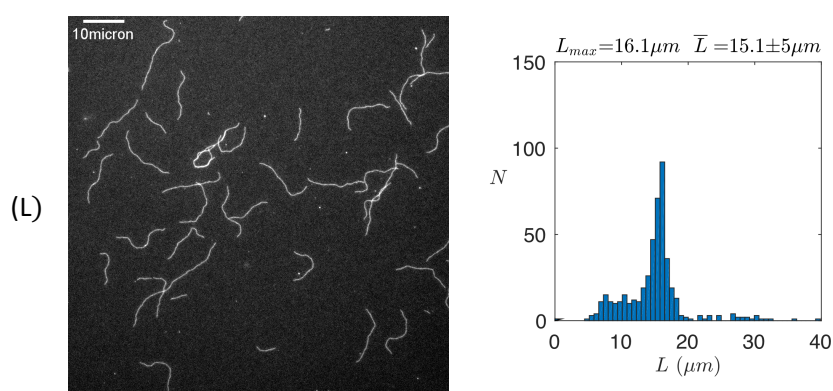


Figure 5.9: Filaments fabricated for long suspension and its length distribution.

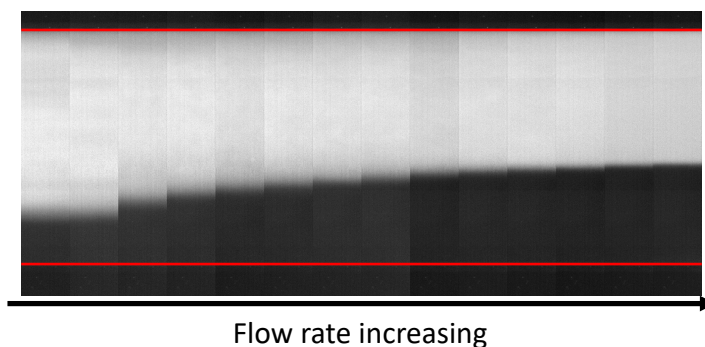


Figure 5.10: Varying interface between suspension (fluorescent) and reference fluid (dark) as increasing flow rate. Red lines are two walls.

be finished. Figure 5.11 shows a first experimental result. Fig. 5.11(B) shows the shear viscosity of a dilute suspension with an average filament length of $\langle L \rangle = 4.3 \mu\text{m}$ and an effective volume fraction $\varphi_{\text{eff}} = 0.5\%$. For a filament of length $4.3 \mu\text{m}$, buckling occurs above the critical shear rate $\dot{\gamma}_c = 5.55 \text{s}^{-1}$. Weak shear thinning observed is mostly likely due to increasing alignment against Brownian rotational diffusion with increasing shear rate.

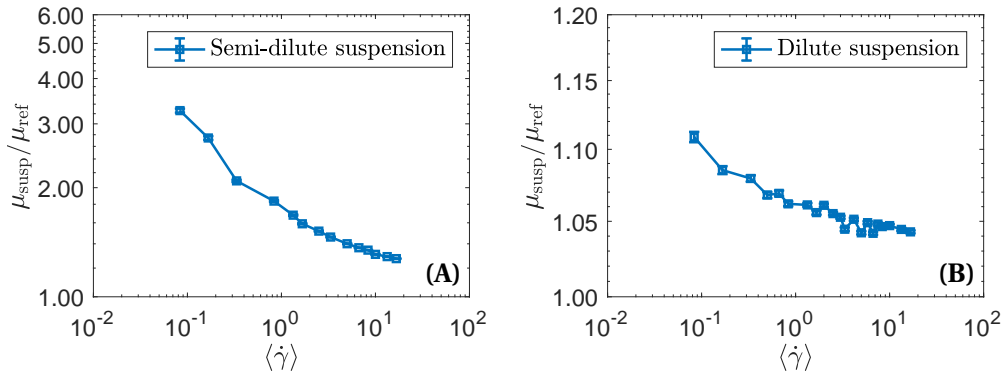


Figure 5.11: (A): The shear viscosities of semi-dilute suspension as a function of average shear rate. (B): The shear viscosities of dilute short suspension as a function of average shear rate.

5.5 Summary and outlook

In this chapter, we developed experimental protocols to fabricate monodisperse actin filament suspensions with narrow length distributions of different average lengths. We used reference fluids to calibrate a microfluidic rheometer that can now be used with an error of less than 5% for sample viscosities close to the viscosity of water. First experiments have been performed and show shear thinning behavior in the low shear rate regime. These preliminary experiments seem to indicate that our experimental system is capable of measuring non-Newtonian behavior of dilute actin suspensions, but final confirmation is still lacking.

Additional experiments are needed that systematically vary the volume fraction and the average length of the filament suspension. The obtained results on the shear viscosity could then be rationalized as a function of the Peclet number as well as the elasto-viscous number. In particular the question whether different slopes in the shear thinning behavior can be observed and linked to the microscopic transitions described in chapter 3 could then be addressed.

In the future it will be interesting to measure normal stress differences. We have been investigating the possibility of using microfluidic rheometers as serpentine channels (Zilz et al., 2014), where normal stress differences are known to lead to flow instabilities in dilute polymer solutions. However due to the different origins of the positive first normal stress differences in both solutions (and in particular a non zero second normal stress difference in the filament suspensions), the instability might not be observable for the actin filament suspensions. Other possibilities are currently being investigated. And finally oscillatory rheology, as currently implemented into a microfluidic device in the group, might also reveal interesting rheological properties.

References

- Batchelor, G. The stress system in a suspension of force-free particles. *Journal of fluid mechanics*, 41(3):545–570, 1970.
- Becker, L. E. and Shelley, M. J. Instability of elastic filaments in shear flow yields first-normal-stress differences. *Physical Review Letters*, 87(19):198301, 2001.
- Chakrabarti, B. and Saintillan, D., in preparation.
- Gachelin, J., Miño, G., Berthet, H., Lindner, A., Rousselet, A., and Clément, É. Non-newtonian viscosity of escherichia coli suspensions. *Physical review letters*, 110(26):268103, 2013.
- Galambos, P. and Forster, F. An optical micro-fluidic viscometer. *ASME Int. Mech. Eng. Cong. Exp., Anaheim, CA*, pages 187–191, 1998.
- Jégou, A., Carlier, M.-F., and Romet-Lemonne, G. Microfluidics pushes forward microscopy analysis of actin dynamics. *Bioarchitecture*, 1(6):271–276, 2011.
- Niedermayer, T., Jégou, A., Chièze, L., Guichard, B., Helfer, E., Romet-Lemonne, G., Carlier, M.-F., and Lipowsky, R. Intermittent depolymerization of actin filaments is caused by photo-induced dimerization of actin protomers. *Proceedings of the National Academy of Sciences*, 109(27):10769–10774, 2012.
- Saintillan, D. and Shelley, M. J. Active suspensions and their nonlinear models. *Comptes Rendus Physique*, 14(6):497–517, 2013.
- Shekhar, S., Kerleau, M., Kühn, S., Pernier, J., Romet-Lemonne, G., Jégou, A., and Carlier, M.-F. Formin and capping protein together embrace the actin filament in a ménage à trois. *Nature communications*, 6:8730, 2015.
- Tornberg, A.-K. and Shelley, M. J. Simulating the dynamics and interactions of flexible fibers in stokes flows. *Journal of Computational Physics*, 196(1):8–40, 2004.
- Zilz, J., Schäfer, C., Wagner, C., Poole, R. J., Alves, M. A., and Lindner, A. Serpentine channels: micro-rheometers for fluid relaxation times. *Lab on a Chip*, 14(2):351–358, 2014.

Chapter 6

Conclusion and outlook

Contents

6.1 Conclusion	94
6.2 Outlook	95
References	96

6.1 Conclusion

In this thesis, we used actin filaments as an experimental model system to systematically study the dynamics of flexible Brownian filaments in flows and the properties of their suspensions. The experiments are carried out through a combination of protocols for controlled protein polymerization, fluorescent labeling techniques, flow control and tracking techniques. The observed phenomena at different length scales are analyzed and understood from experiments, simulations and theory.

To study the dynamics of individual filaments in controlled flows, two different microfluidic geometries have been implemented. A vertical Hele-Shaw cell and a hyperbolic channel were used to provide linear shear and straining flows respectively. To obtain linear shear flow, the dimensions of a vertical Hele-Shaw cell were carefully chosen to separate the length scales of channel and filament dimensions. Locally the Poiseuille flow could thus be considered as a linear shear flow. To obtain constant strain rates over long distance, an optimized hyperbolic channel (Zografos et al., 2016) was used, taking into account the three dimensional flow structure induced by the bounding walls. To directly observe individual filament dynamics in these geometries, sophisticated tracking programs have been developed to track filaments during transport. In the shear flow, the tracking program realizes an automatic adjustment of the z position to keep the filament in focus when transported over long distances in the Hele-Shaw cell. In the hyperbolic flow, the tracking program displaces automatically the microscope stage to follow the flow profile, along the narrowing and widening channel. This requires strong acceleration and deceleration of the stage to follow the linear increase and decrease of the flow velocity.

In shear flow, we directly observed the dynamics of single actin filaments in terms of deformation and rotation. The control parameter of the system is the elasto-viscous number $\bar{\mu} = 8\pi\mu\dot{\gamma}L^4$, comparing viscous drag forces to elastic restoring forces. Through varying the length of the filaments and the experienced local shear rates, this control parameter could be varied over several orders of magnitude. Several typical dynamics, including rodlike tumbling, C buckling, U snake turn and S snake turn have been identified and quantitatively analyzed. They are in good agreement with numerical work based on non-local slender body theory in the presence of Brownian fluctuations. The transitions between these dynamics are characterized by $\bar{\mu}/c$, which is the ratio between the elasto-viscous number and the slenderness c , $c = \ln(\epsilon^2/e)$. The transition from rodlike tumbling to C shape buckling corresponds to a buckling instability that had been previously predicted using linear stability analysis (Becker and Shelley, 2001). Our results are in good agreement with the predicted threshold of $\bar{\mu}/c = 306.4$. The transition from C shape buckling to U snake turn has not been quantified before. Modeling the cross-over via a J shape configuration, which is a semi-circle connected to a straight arm with a tilt angle, we find a threshold of $\bar{\mu}/c \approx 1700$, in good agreement with experimental and nu-

merical findings. The J shape model also gives theoretical solution of the temporal evolution of the configurations, again in good agreement with experimental and simulation results. We have showed that Brownian fluctuations affect the transitions only weakly and they mainly tend to broaden the latter. This work has been accepted for publication in Proceedings of the National Academy of Sciences (Liu et al., 2018).

In straining flow, opposite signs of the strain rate lead to completely different dynamics. In extensional flow, we have observed that viscous forces suppressed thermal fluctuations. We have characterized these fluctuations and have compared them to results from previous experimental, numerical and theoretical studies (Kantsler and Goldstein, 2012; Harishankar, 2009). In compressive flow, strong fiber buckling, with high buckling modes, is observed. In addition, we identify for the first time experimentally the formation of a helical structure in such compressive flows. The cross-over from a quasi two dimensional filament towards these three dimensional structures has been seen in numerical simulations, but the necessary ingredients for helix formation remain unclear for the moment.

To study the macroscopic properties of actin filament suspensions, we developed reproducible protocols to fabricate monodisperse actin filament suspensions. Narrow length distributions with different mean length could be obtained. To measure the shear viscosities of these suspensions, a microfluidic channel with a Y shape has been calibrated and used as a viscometer. Preliminary results indicate a shear thinning behavior, but systematic experiments still need to be performed.

6.2 Outlook

In this PhD we have characterized the individual dynamics of flexible Brownian filaments in simple, well-controlled flows using actin filaments. Some questions remain open on the microscopic dynamics in these simple flows. For example, the frequency dynamics of individual flexible and Brownian filament in shear flows are still in discussion in the literature (Harasim et al., 2013; Lang et al., 2014), and need to be further explored. The origin of the helix formation observed in our experiments under compression is still not clear. While such flow induced helical structures have previously been observed experimentally (Mercader et al., 2010) and predicted numerically (Chelakkot et al., 2012), the necessary physical ingredients are not known. Our experiments are the first experimental identification of such helix formation and more precise analysis of these results might give important ingredients. Further more continuous collaboration with Brato Chakrabarti and David Saintillan on numerical simulations and Mike Shelley on linear stability analysis might lead to a more fundamental understanding. And finally, the understandings of filament dynamics in simple flows presented here, represent the first step towards the understanding of filament dynamics in more complex flows, as Poiseuille flows or oscillatory flows (Słowicka et al., 2013; Farutin et al., 2016; Pawłowska

et al., 2017).

The rheology of dilute suspensions of flexible Brownian filaments remains nearly unexplored from an experimental point of view. This is mainly due to the fact that it is not easy to obtain good enough resolution to be able to access non-Newtonian properties in this dilute regime. Our experiments on the shear viscosity of actin filament suspensions are a first and important step, which needs to be explored further. Theoretical results (Tornberg and Shelley, 2004) also predict the existence of first normal stress differences above the buckling threshold. No measurements on normal stress differences for dilute suspensions of flexible fibers exist so far. In the future, the use of a microfluidic rheometer based on the onset of an instability triggered by normal stress differences (Zilz et al., 2014) could be explored. The use of microfluidic rheometers as presented here, might finally also allow for a direct link between the microscopic filament dynamics and the macroscopic suspension properties (Lindner et al., 2018). In addition, a continuous cross-over towards semi-dilute suspensions could be investigated, with the aim to understand the importance of hydrodynamic interactions between filaments.

References

- Becker, L. E. and Shelley, M. J. Instability of elastic filaments in shear flow yields first-normal-stress differences. *Physical Review Letters*, 87(19):198301, 2001.
- Chelakkot, R., Winkler, R. G., and Gompper, G. Flow-induced helical coiling of semi-flexible polymers in structured microchannels. *Physical review letters*, 109(17):178101, 2012.
- Farutin, A., Piasecki, T., Słowicka, A. M., Misbah, C., Wajnryb, E., and Ekiel-Jezewska, M. L. Dynamics of flexible fibers and vesicles in poiseuille flow at low reynolds number. *Soft matter*, 12(35):7307–7323, 2016.
- Harasim, M., Wunderlich, B., Peleg, O., Kröger, M., and Bausch, A. R. Direct observation of the dynamics of semiflexible polymers in shear flow. *Physical review letters*, 110(10):108302, 2013.
- Harishankar, M. *Bending, Buckling, Tumbling, Trapping: Viscous Dynamics of Elastic Filaments*. PhD thesis, University of California, San Diego, 2009.
- Kantsler, V. and Goldstein, R. E. Fluctuations, dynamics, and the stretch-coil transition of single actin filaments in extensional flows. *Physical review letters*, 108(3):038103, 2012.
- Lang, P. S., Obermayer, B., and Frey, E. Dynamics of a semiflexible polymer or polymer ring in shear flow. *Physical Review E*, 89(2):022606, 2014.
- Lindner, A., Shelley, M. J., du Roure, O., and Nazockdast, E. Dynamics of flexible fibers in flows. *Annual Review of Fluid Mechanics*, 50(1), 2018.

- Liu, Y., Chakrabarti, B., Saintillan, D., Lindner, A., and Roure, O. d. Tumbling, buckling, snaking: Morphological transitions of elastic filaments in shear flow. *arXiv preprint arXiv:1803.10979*, 2018.
- Mercader, C., Lucas, A., Derré, A., Zakri, C., Moisan, S., Maugey, M., and Poulin, P. Kinetics of fiber solidification. *Proceedings of the National Academy of Sciences*, 2010.
- Pawłowska, S., Nakielski, P., Pierini, F., Piechocka, I. K., Zembrzycki, K., and Kowalewski, T. A. Lateral migration of electrospun hydrogel nanofilaments in an oscillatory flow. *PloS one*, 12(11):e0187815, 2017.
- Słowicka, A. M., Wajnryb, E., and Ekiel-Jezewska, M. L. Lateral migration of flexible fibers in poiseuille flow between two parallel planar solid walls. *The European Physical Journal E*, 36(3):31, 2013.
- Tornberg, A.-K. and Shelley, M. J. Simulating the dynamics and interactions of flexible fibers in stokes flows. *Journal of Computational Physics*, 196(1):8–40, 2004.
- Zilz, J., Schäfer, C., Wagner, C., Poole, R. J., Alves, M. A., and Lindner, A. Serpentine channels: micro-rheometers for fluid relaxation times. *Lab on a Chip*, 14(2):351–358, 2014.
- Zografos, K., Pimenta, F., Alves, M., and Oliveira, M. Microfluidic converging/diverging channels optimised for homogeneous extensional deformation. *Biomicrofluidics*, 10(4):043508, 2016.

Appendix A Eigenmodes under tension

Following the work of (Kantsler and Goldstein, 2012; Harishankar, 2009), we consider a flexible filament of length L transporting with flow $U_0 = (\dot{\gamma}x, 0)$. In the local axis on the center of the filament, the filament fluctuate nearly aligned with the x axis with amplitude $h(x)$ between $[-L/2, L/2]$ as showed in figure A.1. Then the potential energy of the filament due to elasticity and induced tension is given by,



Figure A.1: Fluctuations along flow with amplitude $h(x)$ away from the x -axis.

$$\mathcal{E} = \frac{1}{2} \int_{-L/2}^{L/2} [Bh_{xx}^2 + T(x)h_x^2] dx \quad (\text{A.1})$$

where subscripts indicate differentiation. The nonuniform tension $T(s)$ induced by the flow is given by (Batchelor, 1970),

$$T(s) = \frac{2\pi\mu\dot{\gamma}}{\ln((L/d)^2/e)} \left[\frac{L^2}{4} - x^2 \right] \quad (\text{A.2})$$

Now, the Euler-Lagrange equations that minimises \mathcal{E} for $h(x)$ is

$$\frac{\partial \mathcal{E}}{\partial x} - \frac{\partial}{\partial x} \left(\frac{\partial \mathcal{E}}{\partial h_x} \right) + \frac{\partial^2}{\partial x^2} \left(\frac{\partial \mathcal{E}}{\partial h_{xx}} \right) \quad (\text{A.3})$$

$f(x)$ is a force distribution per unit length that causes the filament to sustain the shape $h(x)$. The Euler-Lagrange equation thus gives us the energetically most favorable posi-

tions $h(x)$:

$$Bh_{xxxx} - (T(x)h_x)_x = f(x) \quad (\text{A.4})$$

Substituting the expression of tension Eq. A.2 into this formula, it turns to be an eigenvalue problem with eigenfunctions $W^n(x)$ and corresponding eigenvalues λ_n :

$$BW_{xxxx}^n - \frac{2\pi\mu\dot{\gamma}}{\ln((L/d)^2/e)} \left[\left(\frac{L^2}{4} - x^2 \right) W_x^n \right]_x = \lambda_n W^n \quad (\text{A.5})$$

with the free boundary conditions $W_{xx}^n(\pm L/2) = 0$, $W_{xxx}^n(\pm L/2) = 0$, $T(\pm L/2) = 0$. After scaling the length with $\xi = \pi x/L \in [-\pi/2, \pi/2]$ we have,

$$BW_{\xi\xi\xi\xi}^n - \Sigma \left[\left(\frac{\pi^2}{4} - \xi^2 \right) W_\xi^n \right]_\xi = \Lambda_n W^n \quad (\text{A.6})$$

here Σ is a dimensionless strain rate and Λ_n are the rescaled eigenvalues $\Lambda_n = L^4 \lambda_n / \pi^4 B$. Now, since $h(x)$ is projected into the $W^n(x)$ basis, we can write

$$h(x) = \sum_{n=1}^{\infty} a_n W^n(x) \quad (\text{A.7})$$

Note that the basis $W^n(x)$ are orthogonal that,

$$\frac{1}{L} \int_{-L/2}^{L/2} W^m(x) W^n(x) dx = \delta_{mn} \quad (\text{A.8})$$

Here, δ_{mn} is Dirac delta function. From Eqn. (A.1), by repeated integration by parts with the free boundary conditions we have,

$$\begin{aligned}
\mathcal{E} &= \frac{1}{2} \int_{-L/2}^{L/2} [Bh_{xx}^2 + T(x)h_x^2] dx \\
&= \frac{1}{2} \left[Bh_{xx}h_x \Big|_{-L/2}^{L/2} - B \int_{-L/2}^{L/2} h_{xxx}h_x dx + (T(x)h_xh) \Big|_{-L/2}^{L/2} - \int_{-L/2}^{L/2} (T(x)h_x)_x dx \right] \\
&= \frac{1}{2} \left[-B \left((h_{xxx}h) \Big|_{-L/2}^{L/2} - \int_{-L/2}^{L/2} h_{xxxx}h dx \right) - \int_{-L/2}^{L/2} (T(x)h_x)_x h dx \right] \\
&= \frac{1}{2} \int_{-L/2}^{L/2} [Bh_{xxxx} - T(x)h_x] h dx
\end{aligned} \tag{A.9}$$

Substituting Eqn. (A.7) and the eigenfunction Eqn. (A.5) into Eqn. (A.9), leads to,

$$\begin{aligned}
\mathcal{E} &= \frac{1}{2} \int_{-L/2}^{L/2} \left(B \sum_{n=1}^{\infty} a_n W_{xxxx}^n - \left[T(x) \sum_{n=1}^{\infty} a_n W_x^n \right]_x \right) \left(\sum_{n=1}^{\infty} a_n W^n \right) dx \\
&= \frac{1}{2} \int_{-L/2}^{L/2} \left(\sum_{n=1}^{\infty} a_n [B W_{xxxx}^n - (T(x)W_x^n)_x] \right) \left(\sum_{n=1}^{\infty} a_n W^n \right) dx \\
&= \frac{1}{2} \int_{-L/2}^{L/2} \left(\sum_{n=1}^{\infty} a_n \lambda_n W^n \right) \left(\sum_{n=1}^{\infty} a_n W^n \right) dx
\end{aligned} \tag{A.10}$$

Taking into account that basis are orthogonal as showed in Eqn. (A.8), we get,

$$\mathcal{E} = \frac{L}{2} \sum_{n=1}^{\infty} \lambda_n a_n^2 \tag{A.11}$$

This tells that that the energy is a sum of contributions from independent modes. The equipartition principle gives that $\lambda_n a_n^2 L/2 = k_B T/2$. Thus,

$$\langle a_m a_n \rangle = \delta_{mn} \frac{k_B T}{\lambda_n L} \tag{A.12}$$

Using the rescaled eigenvalue $\Lambda_n = \lambda_n L^4 / (\pi^4 B)$ and the definition of the persistence length $\ell_p = B / (k_B T)$, this simplifies to

$$\langle a_m a_n \rangle = \delta_{mn} \frac{L^3}{\Lambda_n \pi^4 \ell_p} \tag{A.13}$$

We now define the variance of amplitude fluctuations as

$$V(x) = \langle [h(x) - \bar{h}]^2 \rangle \quad (\text{A.14})$$

where \bar{h} is the mean filament amplitude. When aligned approximately with the x axis, we can set $\bar{h} = 0$. Thus Eqn. (A.14) is turned to

$$\begin{aligned} V(x) &= \langle h(x)^2 \rangle \\ &= \left\langle \left[\sum_{n=1}^{\infty} a_n W^n(x) \right]^2 \right\rangle \\ &= \sum_{n=1}^{\infty} \frac{L^3}{\Lambda_n \pi^4 \ell_p} W^n(x)^2 \end{aligned} \quad (\text{A.15})$$

$$V(x; \Sigma) = \frac{L^3}{\ell_p \pi^4} \sum_{n=1}^{\infty} \frac{W^n(x; \Sigma)}{\Lambda_n(\Sigma)} \quad (\text{A.16})$$

Another order parameter $\overline{V_e} = [V(-L/2) + V(L/2)]/2$ is introduced to quantify Brownian fluctuations through the mean end fluctuations.

References

- Batchelor, G. The stress system in a suspension of force-free particles. *Journal of fluid mechanics*, 41(3):545–570, 1970.
- Harishankar, M. *Bending, Buckling, Tumbling, Trapping: Viscous Dynamics of Elastic Filaments*. PhD thesis, University of California, San Diego, 2009.
- Kantsler, V. and Goldstein, R. E. Fluctuations, dynamics, and the stretch-coil transition of single actin filaments in extensional flows. *Physical review letters*, 108(3):038103, 2012.

Appendix B

Monodispersed suspension fabrication

Short length suspension fabrication:

Suppose that we have G-actin with concentration of $50\mu\text{M}$, spectrin actin seed with concentration of 22.4nM , normal Phalloidin with concentration of $500\mu\text{M}$. To have the short length suspension, we need to have the concentration ratio between G-actin and seeds to be $8 \times 370 : 1$. If the filaments start to polymer at a very low concentration around $0.5\mu\text{M}$, then we suppose the creation of spontaneous nucleation can be neglected, then the operating steps is following.

- Mix $294.7\mu\text{L}$ of F-buffer with $2.26\mu\text{L}$ of spectrin actin seed at 22.4nM
- Take $3\mu\text{L}$ of concentrated G-actin at 50nM on the bottom of the eppendorf tube
- Put the mixture of F-buffer and seeds into the tube of G-actin and mix thoroughly
- The total volume is $300\mu\text{L}$
- Leave in drak at room temperature 60 minutes
- Add $3\mu\text{L}$ of normal Phalloidin at $500\mu\text{M}$
- Wait for 10 minutes (in drak at room temperature) for Phalloidin diffusing and bounding

Middle and long length suspension fabrication:

In order to have longer filaments, we need to increase the concentration of the actin at the beginning of the polymerization, for instance at $2\mu\text{M}$. And the concentration ratio between G-actin and seeds is $20 \times 370 : 1$ for middle length suspension. In this case, we need to avoid the creation of spontaneous nucleation through adding three times profilin as showed below.

- Take $4\mu\text{L}$ G-actin at 50nM
- Add $2\mu\text{L}$ of 3x exchanging buffer (600mM EGTA, $100\mu\text{M}$ MgCl_2)
- Leave on ice for 5 minutes
- Add $1.8\mu\text{L}$ of Profilin at $170.9\mu\text{M}$
- Leave on ice for 5 minutes
- Mix $91\mu\text{L}$ of F-buffer with $1.21\mu\text{L}$ of spectrin actin seed at 22.4nM
- Put the mixture of F-buffer and seeds into the tube of Profilin bounded actin solution
- The total volume is $100\mu\text{L}$
- Leave in drak at room temperature 60 minutes
- Add $4\mu\text{L}$ of normal Phalloidin at $500\mu\text{M}$
- Wait for 10 minutes (in drak at room temperature) for Phalloidin diffusing and bounding

Tumbling, buckling, snaking: Morphological transitions of elastic filaments in shear flow

Yanan Liu^{a,1}, Brato Chakrabarti^{b,1}, David Saintillan^b, Anke Lindner^{a,2}, and Olivia du Roure^a

^aESPCI Paris, PSL Research University, CNRS, University Paris Diderot, University Pierre et Marie Curie, PMMH, Paris, 75005, France; ^bDepartment of Mechanical and Aerospace Engineering, University of California San Diego, 9500 Gilman Drive, La Jolla, CA 92093, USA

This manuscript was compiled on August 3, 2018

The morphological dynamics, instabilities and transitions of elastic filaments in viscous flows underlie a wealth of biophysical processes from flagellar propulsion to intracellular streaming, and are also key to deciphering the rheological behavior of many complex fluids and soft materials. Here, we combine experiments and computational modeling to elucidate the dynamical regimes and morphological transitions of elastic Brownian filaments in a simple shear flow. Actin filaments are employed as an experimental model system and their conformations are investigated through fluorescence microscopy in microfluidic channels. Simulations matching the experimental conditions are also performed using inextensible Euler-Bernoulli beam theory and non-local slender-body hydrodynamics in the presence of thermal fluctuations, and agree quantitatively with observations. We demonstrate that filament dynamics in this system is primarily governed by a dimensionless elasto-viscous number comparing viscous drag forces to elastic bending forces, with thermal fluctuations only playing a secondary role. While short and rigid filaments perform quasi-periodic tumbling motions, a buckling instability arises above a critical flow strength. A second transition to strongly-deformed shapes occurs at a yet larger value of the elasto-viscous number and is characterized by the appearance of localized high-curvature bends that propagate along the filaments in apparent “snaking” motions. A theoretical model for the so far unexplored onset of snaking accurately predicts the transition and explains the observed dynamics. We present a complete characterization of filament morphologies and transitions as a function of elasto-viscous number and scaled persistence length and demonstrate excellent agreement between theory, experiments and simulations.

polymer dynamics | actin | shear flow | fluid-structure interaction

The dynamics and conformational transitions of elastic filaments and semiflexible polymers in viscous fluids underlie the complex non-Newtonian behavior of their suspensions (1), and also play a role in many small-scale biophysical processes from ciliary and flagellar propulsion (2, 3) to intracellular streaming (4, 5). The striking rheological properties of polymer solutions hinge on the microscopic dynamics of individual polymers, and particularly on their rotation, stretching and deformation under flow in the presence of thermal fluctuations. Examples of these dynamics include the coil-stretch (6, 7) and stretch-coil (8, 9) transitions in pure straining flows, and the quasi-periodic tumbling and stretching of elastic fibers and polymers in shear flows (10, 11). Elucidating the physics behind these microstructural instabilities and transitions is key to unraveling the mechanisms for their complex rheological behaviors (12), from shear thinning and normal stress differences (13) to viscoelastic instabilities (14) and turbulence (15).

The case of long-chain polymers such as DNA (16), for which the persistence length ℓ_p is much smaller than the contour length L , has been characterized extensively in ex-

periments (7, 17) as well as numerical simulations (18) and mean-field models (19). The dynamics in this case is governed by the competition between thermal entropic forces favoring coiled configurations and viscous stresses that tend to stretch the polymer in strain-dominated flows. The interplay between these two effects is responsible for the coil-stretch transition in elongational flows and tumbling and stretching motions in shear flows, both of which are well captured by classic entropic bead-spring models (20–22).

On the contrary, the dynamics of shorter polymers such as actin filaments (23), for which $L \sim \ell_p$, has been much less investigated and is still not fully understood. Here, it is the subtle interplay of bending forces, thermal fluctuations and internal tension under viscous loading that instead dictates the dynamics. Indeed, bending energy and thermal fluctuations are now of comparable magnitudes, while the energy associated with stretching is typically much larger due to the small diameter of the molecular filaments (1). This distinguishes these filaments from long entropy-dominated polymers such as DNA in which chain bending plays little role.

The classical case of a rigid rod-like particle in a linear flow is well understood since the work of Jeffery (24), who first described the periodic tumbling now known as Jeffery orbits occurring in shear flow. When flexibility becomes significant, viscous stresses applied on the filament can overcome bending resistance and lead to structural instabilities reminiscent of

Significance Statement

Elastic filaments and semiflexible polymers occur ubiquitously in biophysical systems and are key components of many complex fluids, yet our understanding of their conformational dynamics under flow is incomplete. Here, we report on experimental observations of actin filaments in simple shear and characterize their various dynamical regimes from tumbling to buckling and snaking. Numerical simulations accounting for elastohydrodynamics as well as Brownian fluctuations show perfect agreement with measurements. Using a reduced-order theoretical model, we elucidate the unexplained mechanism for the transition to snaking. Our results pave the way for a better understanding of biophysical processes as well as the rheology of sheared soft materials, and provide a theoretical framework for the exploration of the dynamics of dilute and semi-dilute suspensions.

Author contributions: Y.L., A.L. and O.d.R. performed experiments. B.C. and D.S. performed simulations. All authors contributed to the theoretical model, to the analysis and interpretation of data, and to the manuscript preparation.

The authors declare no conflict of interest.

¹ Y.L. and B.C. contributed equally to this work.

² To whom correspondence should be addressed. E-mail: anke.lindner@espci.fr

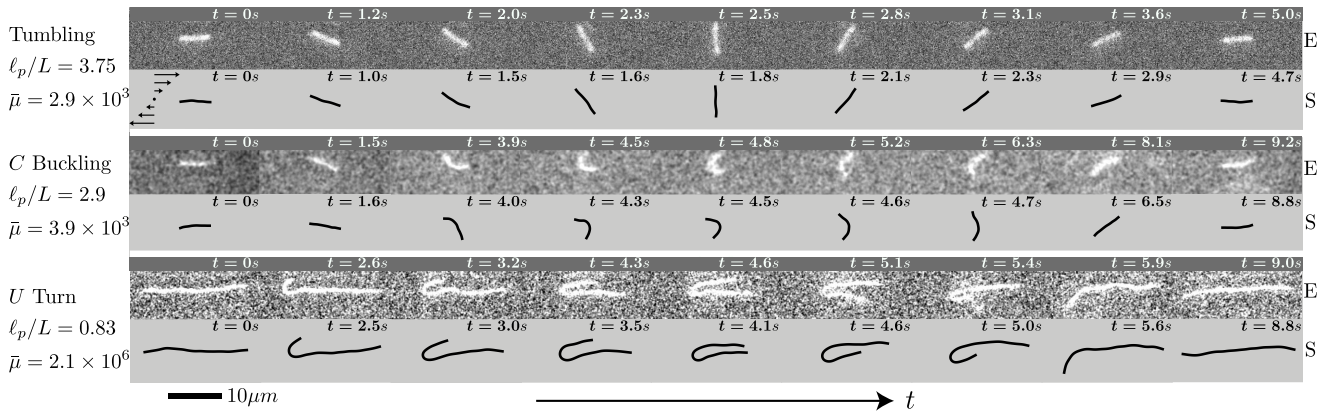


Fig. 1. Temporal evolution of the filament shape in planar shear over one period of motion, showing three representative cases corresponding to increasing elasto-viscous numbers. In each case, we compare fluorescence images from experiments (E) to Brownian dynamics simulations (S). Movies of the dynamics are provided in the SI Appendix.

Euler buckling of elastic beams (8–10, 25–28). On the other hand, Brownian orientational diffusion has been shown to control the characteristic period of tumbling (23, 29). In shear flow, the combination of rotation and deformation leads to particularly rich dynamics (23, 30–35), which have yet to be fully characterized and understood.

In this work, we elucidate these dynamics in a simple shear flow by combining numerical simulations, theoretical modeling and model experiments using actin filaments. The filaments we consider here have a contour length L in the range of 4–40 μm and a diameter of $d \sim 8\text{nm}$. By analyzing the fluctuating shapes of the filaments, we measured the persistence length, as shown in (36), to be $\ell_p = 17 \pm 1\mu\text{m}$ independent of the solvent viscosity. We combine fluorescent labeling techniques, microfluidic flow devices and an automated-stage microscopy apparatus to systematically identify deformation modes and conformational transitions. Our experimental results are confronted against Brownian dynamics simulations and theoretical models that describe actin filaments as thermal inextensible Euler-Bernoulli beams whose hydrodynamics follow slender-body theory (10). By varying contour length as well as applied shear rates in the range of $\dot{\gamma} \sim 0.5 - 10\text{s}^{-1}$, we identify and characterize transitions from Jeffery-like tumbling dynamics of stiff filaments to buckled and finally strongly bent configurations for longer filaments.

Results and discussion

Governing parameters and filament dynamics. In this problem, the filament dynamics results from the interplay of three physical effects – elastic bending forces, thermal fluctuations and viscous stresses, and is governed by three independent dimensionless groups. First, the ratio of the filament persistence length ℓ_p to the contour length L characterizes the amplitude of transverse fluctuations due to thermal motion, with the limit of $\ell_p/L \rightarrow \infty$ describing rigid Brownian fibers. Second, the elasto-viscous number $\bar{\mu}$ compares the characteristic time scale for elastic relaxation of a bending mode to the time scale of the imposed flow, and is defined in terms of the solvent viscosity μ , applied shear rate $\dot{\gamma}$, filament length L and bending rigidity B as $\bar{\mu} = 8\pi\mu\dot{\gamma}L^4/B$. Note that B and ℓ_p are related as $B = k_B T \ell_p$. Third, the anisotropic drag coefficients along the filament involve a geometric parameter $c = -\ln(\epsilon^2 e)$ capturing the effect of slenderness, where $\epsilon = d/L$.

The elasto-viscous number can be viewed as a dimensionless

measure of flow strength and exhibits a strong dependence on contour length. By varying L and $\dot{\gamma}$, we have systematically explored filament dynamics over several decades of $\bar{\mu}$ and observed a variety of filament configurations, the most frequent of which we illustrate in Fig. 1. In relatively weak flows, the filaments are found to tumble without any significant deformation in a manner similar to rigid Brownian rods. On increasing the elasto-viscous number, a first transition is observed whereby compressive viscous forces overcome bending rigidity and drive a structural instability towards a characteristic C shaped configuration during the tumbling motion. By analogy with Euler beams, we term this deformation mode “global buckling” as it occurs over the full length of the filament. In stronger flows, this instability gives way to highly bent configurations, which we call U turns and are akin to the snaking motions previously observed with flexible fibers (23, 32). During those turns, the filament remains roughly aligned with the flow direction while a curvature wave initiates at one end and propagates towards the other end. At yet higher values of $\bar{\mu}$, more complex shapes can also emerge, including an S turn which is similar to the U turn but involves two opposing curvature waves emanating simultaneously from both ends (see SI Appendix for movies). In all cases, excellent agreement is observed between experimental measurements and Brownian dynamics simulations. Our focus here is in describing and explaining the first three deformation modes and corresponding transitions.

We characterize the temporal shape evolution more quantitatively for each case in Fig. 2. In order to describe the overall shape and orientation of the filament, we introduce the gyration tensor, or the second mass moment, as

$$G_{ij}(t) = \frac{1}{L} \int_0^L [r_i(s, t) - \bar{r}_i(t)][r_j(s, t) - \bar{r}_j(t)] ds, \quad [1]$$

where $\mathbf{r}(s, t)$ is a two-dimensional parametric representation of the filament centerline with arclength $s \in [0, L]$ in the flow-gradient plane, and $\bar{\mathbf{r}}(t)$ is the instantaneous center-of-mass position. The angle χ between the mean filament orientation and the flow direction is provided by the eigenvectors of G_{ij} , while its eigenvalues (λ_1, λ_2) can be combined to define a sphericity parameter $\omega = 1 - 4\lambda_1\lambda_2/(\lambda_1 + \lambda_2)^2$ quantifying filament anisotropy: $\omega \approx 0$ for nearly isotropic configurations ($\lambda_1 \approx \lambda_2$), and $\omega \approx 1$ for nearly straight shapes ($\lambda_1 \gg \lambda_2 \approx 0$). Other relevant measures of filament conformation are the scaled end-to-end distance $L_{ee}(t)/L = |\mathbf{r}(L, t) - \mathbf{r}(0, t)|/L$, whose departures from its maximum value of 1 are indica-

tive of bent or folded shapes, and the total bending energy $E(t) = \frac{B}{2} \int_0^L \kappa^2(s, t) ds$, which is an integrated measure of the filament curvature $\kappa(s, t)$.

As is evident in Fig. 2, these different variables exhibit distinctive signatures in each of the three regimes and can be used to systematically differentiate between configurations. During Jeffery-like tumbling, filaments remain nearly straight with $\omega \approx 1$, $L_{ee} \approx L$ and $E \approx 0$ while the angle χ quasi-periodically varies from $-\pi/2$ to $\pi/2$ over the course of each tumble. During a C buckling event, the angle χ still reaches $\pi/2$, but the other quantities now deviate from their baseline as the filament bends and straightens again. This provides a quantitative measure for distinguishing tumbling motion and C buckling. During a U turn, however, deformations are also significant but χ only weakly deviates from 0 as the filament remains roughly aligned with the flow direction and executes a tank-treading motion rather than an actual tumble. This feature provides a simple test for distinguishing C and U turns in both experiments and simulations. Other hallmarks of U turns are the increased bending energy during the turn, which exhibits a nearly constant plateau while the localized bend in the filament shape travels from one end to the other, and a strong minimum in the end-to-end distance $L_{ee}(t)$, which reaches nearly zero halfway through the turn when the filament is symmetrically folded.

Order parameters. This descriptive understanding of the dynamics allows us to investigate transitions between deformation regimes as the elasto-viscous number increases. The dependence on $\bar{\mu}$ of the maximum bending energy E , minimum value of the sphericity parameter ω , and range $\Delta\chi$ of the mean angle over one or several periods of motion is shown in Fig. 3. In the case of U turns, the maximum bending energy is calculated as an average over the plateau seen in Fig. 2C.

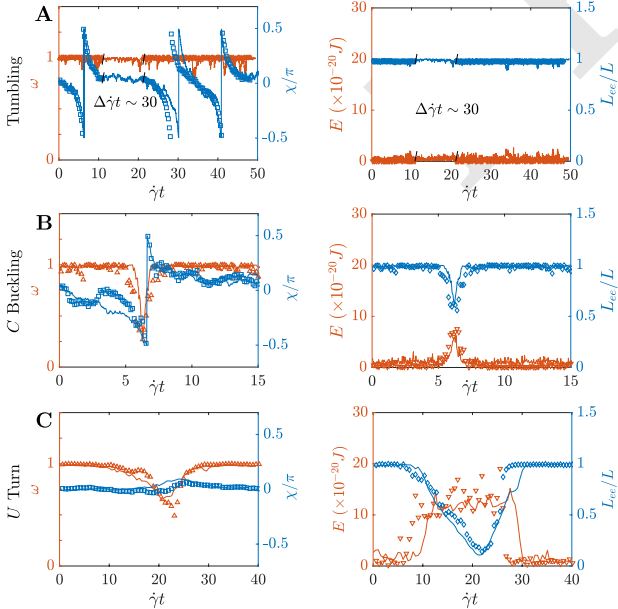


Fig. 2. Evolution of the sphericity parameter ω , mean angle χ with respect to the flow direction, bending energy E and scaled end-to-end distance L_{ee}/L over one period of motion for (A) Jeffery-like tumbling, (B) C buckling, and (C) U turn. Symbols: experiments. Solid lines: simulations. Parameter values are the same as in Fig. 1. The lack of experimental data during the interval $\Delta\dot{\gamma}t \sim 30$ in (A) is due to a temporary loss of focus caused by tumbling of the filament out of the flow-gradient plane.

In the tumbling regime, deformations are negligible beyond those induced by thermal fluctuations, as evidenced by the nearly constant values of $\max(E) \approx 0$ and $\min(\omega) \approx 1$. After the onset of buckling, however, the maximum bending energy starts increasing monotonically with $\bar{\mu}$ as viscous stresses cause increasingly stronger bending of the filament. This increased bending is accompanied by a decrease in ω as bending renders shapes increasingly isotropic, finally reaching $\min(\omega) \approx 0$. Interestingly, the transition to U turns is marked by a plateau of the bending energy, which subsequently only very weakly increases with $\bar{\mu}$. This plateau is indicative of the emergence of strongly bent configurations where the elastic energy becomes localized in one sharp fold, and suggests that the curvature of the folds during U turns depends only weakly on flow strength. The parameter ω also starts increasing again after the onset of U turns, as the filaments adopt hairpin shapes that become increasingly anisotropic. Figure 3AB also shows a few data points for S turns at high values of $\bar{\mu}$: in this regime, the maximum bending energy is approximately twice that of U turns, as bending deformations now become localized in two sharp folds instead of one. S shapes are, however, more compact than U shapes and thus show lower values of ω .

Oriental dynamics are summarized in Fig. 3C, showing the range $\Delta\chi = \chi_{\max} - \chi_{\min}$ of the mean angle χ over one period of motion. During a typical Jeffery-like tumbling or C buckling event, the main filament orientation rotates continuously and as a result $\Delta\chi = \pi$. The scatter in the experimental data is the result of the finite sampling rate during imaging. During U turns, the filament no longer performs tumbles but instead remains globally aligned with the flow direction as it undergoes its snaking motion, resulting in $\Delta\chi < \pi$. This explains the discontinuity in the data of Fig. 3C, where C and U turns stand apart. As $\bar{\mu}$ increases beyond the transition, we find that $\Delta\chi \rightarrow 0$ suggesting a nearly constant mean orientation for the folded shapes characteristic of U turns.

While we have not studied the tumbling frequency extensively, data based on a limited number of simulations and experiments recovers the classical $2/3$ scaling of frequency on flow strength (21, 23) for the explored range of parameters, with a systematic deviation towards $3/4$ in strong flows in agreement with results from Lang et al. (29).

Transitions between regimes and phase diagram. Our experiments and simulations have uncovered three dynamical regimes with increasing values of $\bar{\mu}$, the transitions between which we now proceed to explain. A summary of our results is provided in Fig. 4 as a phase diagram in the $(\bar{\mu}/c, \ell_p/L)$ parameter space, where the transitions are found to occur at fixed values of $\bar{\mu}/c$ independent of ℓ_p/L . The first transition from tumbling motion to C buckling has received much attention in the past, primarily in the case of non-Brownian filaments (10, 13, 31). This limit is amenable to a linear stability analysis (13), which predicts a supercritical pitchfork bifurcation whereby compressive viscous stresses exerted along the filament as it rotates into the compressional quadrant of the flow are sufficiently strong to induce buckling. The stability analysis is based on local slender-body theory, where the natural control parameter arises as $\bar{\mu}/c$, and predicts buckling above a critical value of $\bar{\mu}_c^{(1)}/c \approx 306.4$ (13), in reasonable agreement with our measurements (Fig. 4).

Thermal fluctuations do not significantly alter this threshold, but instead result in a blurred transition (9, 26, 37) with

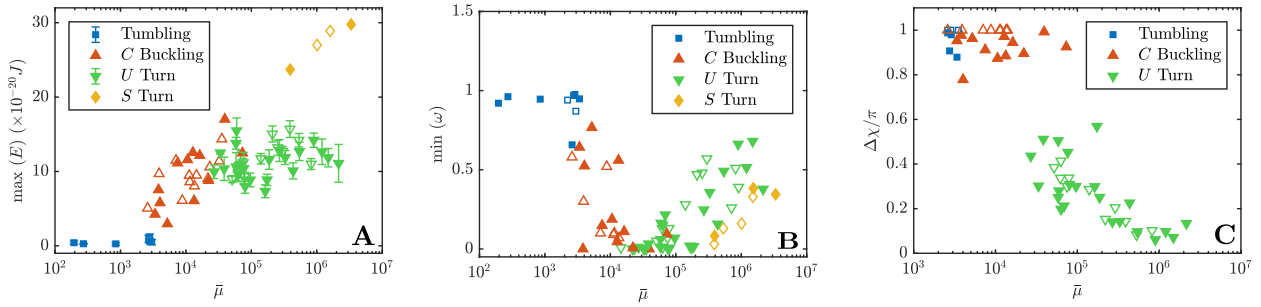


Fig. 3. Dependence on elasto-viscous number $\bar{\mu}$ of: (A) the maximum value of the bending energy E , (B) the minimum value of the sphericity parameter ω , and (C) the range $\Delta\chi$ of the mean angle in the various tumbling and deformation regimes. Full symbols: experiments; open symbols: simulations. For experimental data, the measurement error in $\bar{\mu}$ (due to errors in contour length ($\pm 0.5 \mu\text{m}$) and in local shear rate ($\pm 0.1 \text{ s}^{-1}$)) is comparable to the marker size.

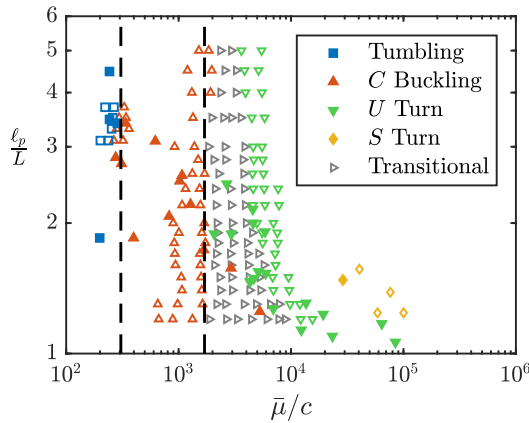


Fig. 4. Phase chart indicating the different dynamical regimes in the $(\bar{\mu}/c, \ell_p/L)$ parameter space. The dashed black lines show the theoretical transitions from tumbling motion to C buckling ($\bar{\mu}_c^{(1)}/c \approx 306.4$), and from C buckling to U turns ($\bar{\mu}_c^{(2)}/c \approx 1700$). Full symbols: experiments; open symbols: simulations.

an increasingly broad transitional regime where both tumbling and C buckling can be observed for a given value of $\bar{\mu}$. When Brownian fluctuations are strong, i.e., for low values of ℓ_p/L , it becomes challenging to differentiate deformations caused by viscous buckling vs fluctuations, and thus the distinction between the two regimes becomes irrelevant.

Upon increasing $\bar{\mu}/c$, the second conformational transition from C shaped filaments to elongated hairpin-like U turns undergoing snaking motions occurs. The appearance of U turns (shown in green in Fig. 4) occurs above a critical value $\bar{\mu}_c^{(2)}/c$ that is again largely independent of ℓ_p/L . However, the transition is not sharp, and near the critical value both shapes can be observed simultaneously (as indicated by gray points). In fact, a single filament in the transitional regime will typically execute both types of turns, switching stochastically between them (see SI Appendix, Fig. S6). This transition towards snaking dynamics has not previously been characterized. Our attempt at understanding its mechanism focuses on the onset of a U turn, which always involves the formation of a J shaped configuration as visible in Fig. 1 and also illustrated in Fig. 5.

To elucidate the transition mechanism, we develop a theoretical model for a J configuration, which can be viewed as a precursor to the U turn. We neglect Brownian fluctuations and idealize the J shape as a semi-circle of radius R connected to a straight arm forming an angle ϕ with the flow direction, with both sections undergoing a snaking motion responsible for the U turn; details of the model, which draws on analogies with the tank-treading motion of vesicles (38, 39), can be

found in the SI Appendix. By satisfying filament inextensibility as well as force and torque balances, and by balancing viscous dissipation in the fluid with the work of elastic forces, we are able to solve for model parameters such as R and ϕ without any fitting. A key aspect of the model is that consistent solutions for these parameters can only be obtained above a critical elasto-viscous number, and this solvability criterion thus provides a threshold $\bar{\mu}_c^{(2)}/c \approx 1700$ below which the J shape ceases to exist. This theoretical prediction is depicted by the dashed line in the phase chart of Fig. 4 and coincides perfectly with the onset of the transitional regime in simulations and experiments.

We can now discuss the initiation of the J -shape, in which two possible mechanisms may be at play. On the one hand, it may be caused by the global buckling of the filament in the presence of highly compressive viscous forces, in a manner consistent with the sequence of shapes of Fig. 5A. Under sufficiently strong shear, compressive forces can induce a buckling instability on a filament that has not yet aligned with the compressional axis and forms only a small angle with the flow direction. Alignment of the deformed filament with the flow then results in differential tension (compression vs tension) near its two ends, thus allowing one end to bend while the other remains straight. A second potential mechanism proposed in (29) is of a local buckling occurring on the typical length scale of transverse thermal fluctuations. Our data, however, clearly show that the transition to U turns is independent of thermal fluctuations, allowing us to discard this hypothesis. Thermal fluctuations are nonetheless responsible for the existence of the transitional regime above $\bar{\mu}_c^{(2)}/c$, where they can destabilize J shapes towards C shapes and thus prevent the occurrence of U turns. This interpretation is consistent with the increasing extent of the transitional regime with decreasing ℓ_p/L .

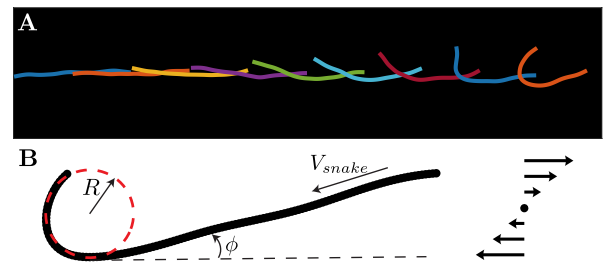


Fig. 5. (A) Numerical snapshots of filament shapes during the formation of a J shape before the initiation of a U turn. (B) The J shape can be approximated by a semicircle of radius R connected to a straight arm forming a tilt angle of ϕ with the flow direction. During snaking, the filament translates tangentially with an axial velocity V_{snake} .

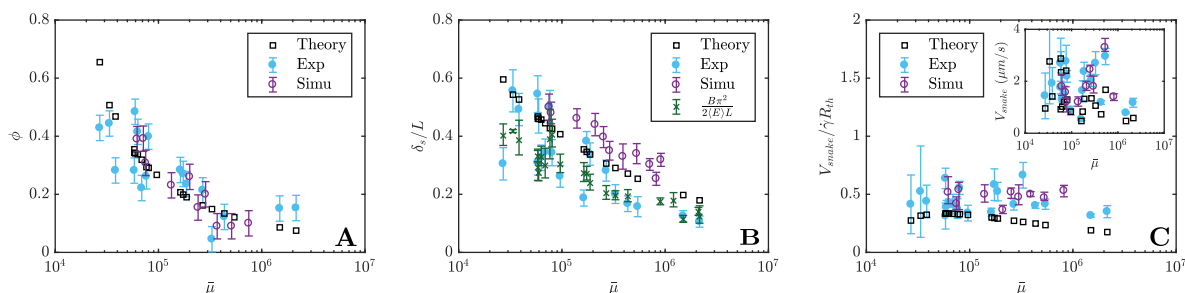


Fig. 6. (A) Dependence on $\bar{\mu}$ of the tilt angle ϕ formed by J shapes with respect to the flow direction in experiments, simulations and in our theoretical model. (B) Fraction δ_s/L of the filament length that is bent during a U turn (see Fig. S4 for the detailed definition of δ_s). The theoretical predictions are based on the J shape at the start of the turn. Since the bending energy during a U turn is concentrated in the fold, an estimate for δ_s/L is also provided by $B\pi^2/2\langle E\rangle L$ where $\langle E\rangle$ is the average bending energy during the turn, and good agreement is found between both measures. (C) Snaking velocity V_{snake} rescaled with $\dot{\gamma}R_{th}$ and plotted against $\bar{\mu}$ from experiments, simulations and theory; here, R_{th} is the theoretically predicted fold radius.

Dynamics of U turns. We further characterize the dynamics during U turns, for which our theoretical model also provides predictions. The filament orientation at the onset of a turn is plotted in Fig. 6A, showing the tilt angle ϕ formed by the straight arm of the J shape with respect to the flow direction as a function of $\bar{\mu}$. Our theoretical model for dynamics of the J shape also provides the value of ϕ , in excellent agreement with experiments. In both cases, the tilt angle decreases with increasing flow strength due to increased alignment by the flow. For very long filaments (limit of large $\bar{\mu}$), accurate measurements of the tilt angle become challenging due to shape fluctuations, hence the increased scatter in the data.

After a J shape is initiated as discussed above, the curvature of the folded region remains nearly constant in time as suggested by the plateau in the bending energy (Fig. 3C). This provides a strong basis for approximating the bent part of the filament as a semi-circle of radius R in our model. The theoretical prediction R_{th} and measurements of the radius on J shapes from experiments and simulations agree quite well in Fig. 6B (see SI Appendix for details). The radius of the bend is seen to decrease with $\bar{\mu}$, as compressive viscous stresses in strong flows allow increasingly tighter folding of the filament.

The rotation of the end-to-end vector during the U turn results primarily from tank-treading of the filament along its arclength, unlike the global rotation that dominates the tumbling and C buckling regimes. While the snaking velocity is not constant during a turn, its average value can be quantitatively measured through the time derivative of the end-to-end distance, yielding the approximation $V_{snake} \approx \dot{L}_{ee}/2$. The relevant dynamic length and time scales during this snaking motion are the radius of curvature R of the bent segment and shear rate $\dot{\gamma}$. This is supported by our theory, where rescaling V_{snake} by $\dot{\gamma}R_{th}$ collapses the predicted velocities over a range of filament lengths (SI Appendix, Fig. S3). The same rescaling applied to the experimental and numerical data and using the theoretical radius R_{th} also provides a good collapse in Fig. 6C.

Harasim *et al.* (23) previously proposed a simplified theory of the U turn, which shares similarities with ours but assumes that the filament is aligned with the flow direction and neglects elastic stresses inside the fold. Their predictions are in partial agreement with our results in the limit of very long filaments and strong shear (see SI Appendix). Their theory is unable to predict and explain the transition from buckling to U turns.

Concluding remarks

Using stabilized actin filaments as a model polymer, we have systematically studied and analyzed the conformational transitions of elastic Brownian filaments in simple shear flow as the elasto-viscous number is increased. Our experimental measurements were shown to be in excellent agreement with a computational model describing the filaments as fluctuating elastic rods with slender-body hydrodynamics. By varying filament contour length and applied shear rate, we performed a broad exploration of the parameter space and confirmed the existence of a sequence of transitions, from rod-like tumbling to elastic buckling to snaking motions. While snaking motions had been previously observed in a number of experimental configurations, the existence of a C buckling regime had not been confirmed clearly. This is due to the fact that C buckling is only visible over a limited range of elasto-viscous numbers and occurs only in simple shear flow, challenging to realize experimentally. We showed that both transitions are primarily governed by $\bar{\mu}/c$. Brownian fluctuations do not modify the thresholds but tend to blur the transitions by allowing distinct dynamics to coexist over certain ranges of $\bar{\mu}$.

While the first transition from tumbling to buckling had been previously described as a supercritical linear buckling instability (13), the transition from buckling to snaking was heretofore unexplained. Using a simple analytical model for the dynamics of the J shape that is the precursor to snaking turns, we were able to obtain a theoretical prediction for the threshold elasto-viscous number above which snake turns become possible. The model did not take thermal noise into account, but highlighted the subtle role played by tension and compression during the onset of the turn. Our analysis and model lay the groundwork for illuminating a wide range of other complex phenomena in polymer solutions, from their rheological response in flow and dynamics in semi-dilute solutions (40, 41) to migration under confinement and microfluidic control of filament dynamics.

Materials and Methods

Experimental Methods. The protocol for assembly of the actin filaments is well controlled and reproducible. Concentrated G-actin, which is obtained from rabbit muscle and purified according to the protocol described in (42), is placed into F-Buffer (10mM Tris-HCl pH=7.8, 0.2mM ATP, 0.2mM CaCl₂, 1mM DTT, 1mM MgCl₂, 100mM KCl, 0.2mM EGTA and 0.145mM DABCO) at a final concentration of 1 μ M. At the same time, Alexa488-fluorescent phalloidin in the same molarity as G-actin is added to prevent depolymerization and thus to stabilize as well as to visualize the

filaments. After 1 hour of polymerization in the dark at room temperature, concentrated F-actin is stored at 4°C for following experiments. To avoid interactions between filaments, F-actin used in experiments has a final concentration of 0.1 nM obtained by diluting the previous solution with F-buffer. 1 mM ascorbic acid is added to decrease photo-bleaching effects and 45.5% (w/v) sucrose to match the refractive index of the PDMS channel ($n = 1.41$). The viscosity of the dilute filament suspension is 5.6 mPa·s at 20°C, measured on an Anton Paar MCR 501 rheometer.

A micro PDMS channel is designed as a vertical Hele-Shaw cell, with length $L = 30$ mm, height $H = 500$ μm and width $W = 150$ μm . In this geometry the filament dynamics can be directly observed in the horizontal shear plane whereas shear in the vertical direction can be neglected at a sufficient distance from the bottom wall (see SI Appendix for more details). To consider pure shear flow, filament and flow scales should be properly separated, and we thus chose a width (150 μm) much larger than the typical dimension of the deformed filament (≈ 10 μm). An objective with long working-distance is required to observe in a plane far enough from the bottom; the objective should also have a large numerical aperture to collect as much light as possible from the fluorescent actin filaments. To combine both of these requirements, we have used a water immersion objective from Zeiss (63X C-Apochromat /1.2NA) with $WD \approx 280$ μm .

Stable flow is driven by a syringe pump (Cellix ExiGo) and particle tracking velocimetry has been used to check the agreement of the velocity profile with theoretical predictions (43). We impose flow rates Q in the range of 5 – 7.5 nL/s, leading to typical filament velocities $u_x \sim 20 - 150$ $\mu\text{m/s}$ in the observation area in the plane $z = 150$ μm . The filament Reynolds number is of the order $Re \sim 10^{-4}$. To follow the filaments during their transport in the channel we use a motorized stage programmed to accurately follow the flow and also to correct for small changes in the z plane, occurring due to slight bending of the channel. This step is necessary as the focal

depth of the objective is only of a few microns and streamlines need to be followed with high precision over distances of several mm.

Images are captured by a s-CMOS camera (HAMAMATSU ORCA flash 4.0LT, 16 bits) with an exposure time of $\Delta t = 65$ ms and are synchronized with the stage displacement. They are processed by Image J to obtain the position of the center of mass and the filament shape. The center of mass is used to calculate the local shear rate experienced by the filament. The shape is extracted through Gaussian blur, threshold, noise reduction and skeletonize procedures. A custom MATLAB code is then used to reconstruct the filament centerline as a sequence of discrete points along the arclength s and to calculate the parameters plotted in Fig. 2.

Modeling and Simulations. We model the filaments as inextensible Euler-Bernoulli beams and use non-local slender-body hydrodynamics to capture drag anisotropy and hydrodynamic interactions (10, 25). Simulations without hydrodynamic interactions (free-draining model) were also performed but did not compare well with experiments. Brownian fluctuations are included and satisfy the fluctuation-dissipation theorem. As experiments only consider quasi-2D trajectories involving dynamics in the focal plane, we perform all simulations in 2D and indeed found better agreement compared to 3D simulations. Details of the governing equations and numerical methods are provided in the SI Appendix. The simulation code is available upon request to the authors.

ACKNOWLEDGMENTS. We are grateful to Guillaume Romet-Lemonne and Antoine Jégou for providing purified actin and to Thierry Darnige for help with the programming of the microscope stage. We thank Michael Shelley, Lisa Fauci, Julien Deschamps, Andreas Bausch, Gwenn Boedec, Anupam Pandey, Harishankar Manikantan and Lailai Zhu for useful discussions, and Roberto Alonso-Matilla for checking some of our calculations. The authors acknowledge support from ERC Consolidator Grant No. 682367, from a CSC Scholarship, and from NSF Grant CBET-1532652.

- Lindner A, Shelley M (2016) Elastic fibers in flows, in *Fluid-Structure Interactions in Low-Reynolds-Number Flows*. (The Royal Society of Chemistry), pp. 168–192.
- Brennen C, Winet H (1977) Fluid mechanics of propulsion by cilia and flagella. *Annu. Rev. Fluid Mech.* 9:339–398.
- Blake JR (2001) Fluid mechanics of ciliary propulsion, in *Computational Modeling in Biological Fluid Dynamics*. (Springer), pp. 1–51.
- Ganguly S, Williams LS, Palacios IM, Goldstein RE (2012) Cytoplasmic streaming in *Drosophila oocytes* varies with kinesin activity and correlates with the microtubule cytoskeleton architecture. *Proc. Natl. Acad. Sci. USA* 109:15109–15114.
- Suzuki K, Miyazaki M, Takagi J, Itabashi T, Ishiwata S (2017) Spatial confinement of active microtubule networks induces large-scale rotational cytoplasmic flow. *Proc. Natl. Acad. Sci. USA* 114:2922–2927.
- De Gennes P (1974) Coil-stretch transition of dilute flexible polymers under ultrahigh velocity gradients. *J. Chem. Phys.* 60:5030–5042.
- Schroeder CM, Babcock HP, Shaqfeh ES, Chu S (2003) Observation of polymer conformation hysteresis in extensional flow. *Science* 301:1515–1519.
- Young YN, Shelley MJ (2007) Stretch-coil transition and transport of fibers in cellular flows. *Phys. Rev. Lett.* 99:058303.
- Kantsler V, Goldstein RE (2012) Fluctuations, dynamics, and the stretch-coil transition of single actin filaments in extensional flows. *Phys. Rev. Lett.* 108:038103.
- Tornberg AK, Shelley MJ (2004) Simulating the dynamics and interactions of flexible fibers in Stokes flows. *J. Comp. Phys.* 196:8–40.
- Schroeder CM, Teixeira RE, Shaqfeh ESG, Chu S (2005) Characteristic periodic motion of polymers in shear flow. *Phys. Rev. Lett.* 95:018301.
- Bird RB, Armstrong RC, Hassager O, Curtiss CF (1977) *Dynamics of polymeric liquids*. (Wiley New York) Vol. 1.
- Becker LE, Shelley MJ (2001) Instability of elastic filaments in shear flow yields first-normal-stress differences. *Phys. Rev. Lett.* 87:198301.
- Shaqfeh ESG (1996) Purely elastic instabilities in viscometric flows. *Annu. Rev. Fluid Mech.* 28:129–185.
- Morozov AN, van Saarloos W (2007) An introductory essay on subcritical instabilities and the transition to turbulence in visco-elastic parallel shear flows. *Phys. Rep.* 447:112–143.
- Schroeder CM (2018) Single polymer dynamics for molecular rheology. *J. Rheol.* 62(1):371–403.
- Perkins TT, Smith DE, Chu S (1997) Single polymer dynamics in an elongational flow. *Science* 276(5321):2016–2021.
- Hur JS, Shaqfeh ES, Larson RG (2000) Brownian dynamics simulations of single DNA molecules in shear flow. *J. Rheol.* 44(4):713–742.
- Gerashchenko S, Steinberg V (2006) Statistics of tumbling of a single polymer molecule in shear flow. *Phys. Rev. Lett.* 96(3):038304.
- Schroeder CM, Shaqfeh ESG, Chu S (2004) Effect of hydrodynamic interactions on DNA dynamics in extensional flow: Simulation and single molecule experiment. *Macromolecules* 37:9242–9256.
- Schroeder CM, Teixeira RE, Shaqfeh ES, Chu S (2005) Characteristic periodic motion of polymers in shear flow. *Phys. Rev. Lett.* 95(1):018301.
- Hsieh CC, Larson RG (2005) Prediction of coil-stretch hysteresis for dilute polystyrene molecules in extensional flow. *J. Rheol.* 49:1081–1089.
- Harasim M, Wunderlich B, Peleg O, Kröger M, Bausch AR (2013) Direct observation of the dynamics of semiflexible polymers in shear flow. *Phys. Rev. Lett.* 110(10):108302.
- Jeffery GB (1922) The motion of ellipsoidal particles immersed in a viscous fluid. *Proc. R. Soc. London A* 102(715):161–179.
- Manikantan H, Saintillan D (2013) Subdiffusive transport of fluctuating elastic filaments in cellular flows. *Phys. Fluids* 25(7):073603.
- Manikantan H, Saintillan D (2015) Buckling transition of a semiflexible filament in extensional flow. *Phys. Rev. E* 92(4):041002.
- Quennou N, Shelley M, du Roure O, Lindner A (2015) Transport and buckling dynamics of an elastic fibre in a viscous cellular flow. *J. Fluid Mech.* 769:387–402.
- Guglielmini L, Kushwaha A, Shaqfeh E, Stone H (2012) Buckling transitions of an elastic filament in a viscous stagnation point flow. *Phys. Fluids* 24:123601.
- Lang PS, Obermayer B, Frey E (2014) Dynamics of a semiflexible polymer or polymer ring in shear flow. *Phys. Rev. E* 89(2):022606.
- Munk T, Hallatschek O, Wiggins CH, Frey E (2006) Dynamics of semiflexible polymers in a flow field. *Phys. Rev. E* 74(4):041911.
- Nguyen H, Fauci L (2014) Hydrodynamics of diatom chains and semiflexible fibres. *J. R. Soc. Interface* 11(96):20140314.
- Forgacs O, Mason S (1959) Particle motions in sheared suspensions: X. Orbits of flexible threadlike particles. *J. Colloid Sci.* 14(5):473–491.
- Pawłowska S, et al. (2017) Lateral migration of electrospun hydrogel nanofilaments in an oscillatory flow. *PLOS ONE* 12(11):1–21.
- Delmotte B, Climent E, Plouraboué F (2015) A general formulation of Bead Models applied to flexible fibers and active filaments at low Reynolds number. *Journal of Computational Physics* 286:14–37.
- Chelakkot R, Winkler RG, Gompper G (2010) Migration of semiflexible polymers in microcapillary flow. *EPL* 91:14001.
- Gittes F, Mickey B, Nettleton J, Howard J (1993) Flexural rigidity of microtubules and actin filaments measured from thermal fluctuations in shape. *J. Cell. Biol.* 120:923–923.
- Baczynski K, Lipowsky R, Kierfeld J (2007) Stretching of buckled filaments by thermal fluctuations. *Phys. Rev. E* 76(6):061914.
- Keller SR, Skalak R (1982) Motion of a tank-treading ellipsoidal particle in a shear flow. *J. Fluid Mech.* 120:27–47.
- Rioual F, Biben T, Misbah C (2004) Analytical analysis of a vesicle tumbling under a shear flow. *Phys. Rev. E* 69(6):061914.
- Kirchenbuechler I, Guu D, Kurniawan Na, Koenderink GH, Lettinga MP (2014) Direct visualization of flow-induced conformational transitions of single actin filaments in entangled solutions. *Nature Comm.* 5:5060.
- Huber B, Harasim M, Wunderlich B, Kröger M, Bausch AR (2014) Microscopic origin of the non-Newtonian viscosity of semiflexible polymer solutions in the semidilute regime. *ACS Macro Letters* 3(2):136–140.
- Spudis JA, Watt S (1971) The regulation of rabbit skeletal muscle contraction I. Biochemical studies of the interaction of the tropomyosin-troponin complex with actin and the proteolytic fragments of myosin. *J. Biol. Chem.* 246(15):4866–4871.
- White FM, Corfield I (2006) *Viscous fluid flow*. (McGraw-Hill New York) Vol. 3.

Supporting Information

Liu et al.

Microfluidic channel geometry

The microfluidic channel used in experiments is a vertical Hele-Shaw cell in which we drive a horizontal flow as illustrated in figure S1A. The channel dimensions are designed based on two factors: (1) The aspect ratio between height and width should be large enough to provide a velocity plateau in the z direction near the channel center as soon as $z \gtrsim W$; in this region, the flow is nearly two-dimensional and the filaments are mainly deformed by the imposed shear rate $\dot{\gamma}_y$ in the xOy plane; (2) The width of the channel is much larger than the typical transverse length scale Δy of the deformed filaments, so that the shear can be approximated as constant over that length scale. To avoid wall-interaction effects and artefacts due to the change in sign of $\dot{\gamma}_y$ near the centerline, we focus on trajectories of filaments flowing in the blue region in figure S1B. Figure S1C shows raw images and reconstructed filaments for two different configurations as well as corresponding parameters: \mathbf{L}_{ee} (red) is the end-to-end vector, $\mathbf{t}(s)$ (black) is the tangential vector, $\boldsymbol{\xi}_{max}$ (blue) is the eigenvector corresponding to the largest eigenvalue of the gyration tensor of the filament, and χ is the angle between $\boldsymbol{\xi}_{max}$ and the flow direction.

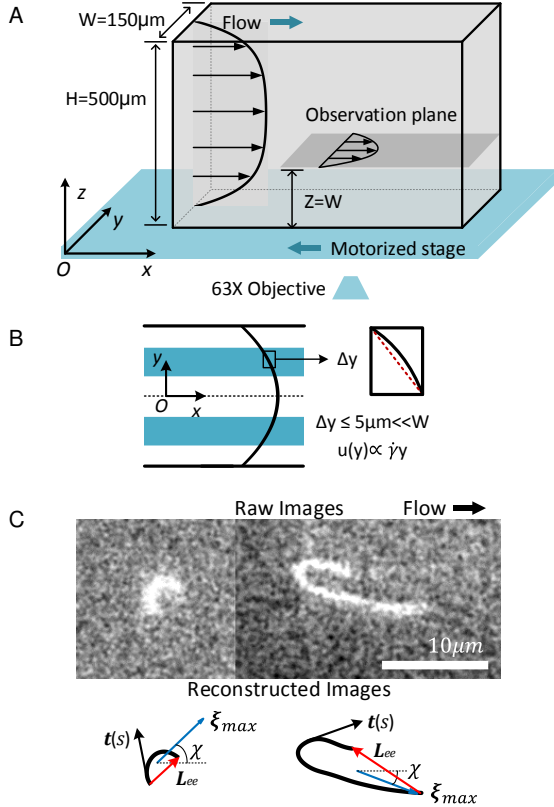


Fig. S1. (A) Sketch of the experimental setup. (B) Velocity profile in the observation plane. Measurements take place in the blue regions, where the profile can be approximated as linear on the typical transverse scale Δy of a filament. (C) Raw images and reconstructed images of two configurations with corresponding parameters.

Liu et al.

Computational model and methods

Actin filaments considered in this work have a characteristic diameter $d \sim 8$ nm and typical lengths in the range of $L \sim 4 - 40$ μm . Due to the slenderness of these filaments (aspect ratio $\epsilon \equiv d/L \ll 1$), we opt to describe them as space curves parameterized by arc length $s \in [0, L]$, with Lagrangian marker $\mathbf{r}(s, t)$ denoting the position of any point along the centerline. Under over-damped conditions typical of microscale flows, seeking a balance between forces due to stretching and viscous drag provides the characteristic time scale for relaxation of a stretching mode as $\tau_s \sim \mu(L/d)^2/Y$, where Y denotes Young's modulus (1). A similar balance between bending forces and viscous drag provides the relaxation time of bending modes as $\tau_b \sim \mu(L/d)^4/Y$. The ratio of these two time scales is $\tau_s/\tau_b \sim (L/d)^{-2} \sim \mathcal{O}(10^{-6})$, which implies that stretching modes relax much faster than bending modes. Consequently, we can approximate the filaments as inextensible, which results in a metric constraint on the Lagrangian marker: $\mathbf{r}_s \cdot \mathbf{r}_s = 1$, where indices denote partial differentiation and $\mathbf{r}_s = \hat{\mathbf{t}}$ is the local tangent vector. The bending energy of a filament with contour length L is given by:

$$E = \frac{B}{2} \int_0^L |\mathbf{r}_{ss}|^2 ds, \quad [1]$$

where B is the bending rigidity of the filament, which also defines its persistence length $\ell_p = B/k_B T$. The phalloidin-stabilized actin filaments considered here have a persistence length of $\ell_p = 17 \pm 1$ μm (2-4). We model these filaments as inextensible fluctuating Euler-Bernoulli beams whose hydrodynamics in an imposed flow $\mathbf{U}_0(\mathbf{r}) = \dot{\gamma}y$ are described by non-local slender-body theory (5, 6) as

$$8\pi\mu(\mathbf{r}_t - \mathbf{U}_0(\mathbf{r})) = -\Lambda[\mathbf{f}](s) - K[\mathbf{f}](s), \quad [2]$$

with

$$\Lambda[\mathbf{f}] = [-c(\mathbf{I} + \mathbf{r}_s \mathbf{r}_s) + 2(\mathbf{I} - \mathbf{r}_s \mathbf{r}_s)] \cdot \mathbf{f}(s), \quad [3]$$

$$K[\mathbf{f}] = \int_0^L \left(\frac{\mathbf{I} + \hat{\mathbf{R}}\hat{\mathbf{R}}}{|\hat{\mathbf{R}}|} \mathbf{f}(s') - \frac{\mathbf{I} + \mathbf{r}_s \mathbf{r}_s}{|s - s'|} \mathbf{f}(s) \right) ds'. \quad [4]$$

Here, μ is the suspending fluid viscosity, $\hat{\mathbf{R}} = \mathbf{r}(s) - \mathbf{r}(s')$, and $c = -\ln(\epsilon e^2)$ is a geometric parameter. Λ is a local mobility operator that accounts for drag anisotropy, while the integral operator K captures the effect of hydrodynamic interactions between different parts of the filament. The force per unit length $\mathbf{f}(s)$ has contributions from bending and tension forces as well as Brownian fluctuations:

$$\mathbf{f}(s, t) = B\mathbf{r}_{ssss} - (\sigma(s)\mathbf{r}_s)_s + \mathbf{f}^{br}, \quad [5]$$

where $\sigma(s)$ is the Lagrange multiplier that enforces the constraint of inextensibility and can be interpreted as internal tension. The Brownian force density \mathbf{f}^{br} obeys the fluctuation-dissipation theorem (7, 8):

$$\langle \mathbf{f}^{br}(s, t) \rangle = \mathbf{0}, \quad [6]$$

$$\langle \mathbf{f}^{br}(s, t) \mathbf{f}^{br}(s', t') \rangle = 2k_B T \Lambda^{-1} \delta(s - s') \delta(t - t'). \quad [7]$$

1 of 5

Since the filament is freely suspended, we apply force- and moment-free boundary conditions at both filament ends, which translate to: $\mathbf{r}_{sss} = \mathbf{r}_s = \sigma = 0$.

We non-dimensionalize the governing equations by scaling spatial variables with L , time by the characteristic relaxation time $8\pi\mu L^4/B$, the external flow by $L\dot{\gamma}$, deterministic forces by the bending force scale B/L^2 and Brownian fluctuations by $\sqrt{L/\ell_p}B/L^2$ (7, 8). The dimensionless equations are given as follows:

$$\mathbf{r}_t = \bar{\mu}\mathbf{U}_0(\mathbf{r}(s, t)) - \Lambda[\mathbf{f}](s) - K[\mathbf{f}](s), \quad [8]$$

$$\mathbf{f} = \mathbf{r}_{ssss} - (\sigma(s)\mathbf{r}_s)_s + \sqrt{L/\ell_p}\boldsymbol{\zeta}, \quad [9]$$

where two-dimensionless groups govern the dynamics: the elasto-viscous number $\bar{\mu} = 8\pi\mu\dot{\gamma}L^4/B$ is the ratio of the characteristic flow time scale to the time scale for elastic relaxation of a bending mode, while L/ℓ_p compares the filament contour length to its persistence length and measures the magnitude of thermal fluctuations. The random vector $\boldsymbol{\zeta}$ is uncorrelated in space and time and drawn from a Gaussian distribution with zero mean and unit variance. Eqs. (8)–(9) are numerically integrated in time using an implicit-explicit time-stepping method that treats the stiff linear terms coming from bending elasticity implicitly and non-linear terms explicitly. At every time step, the unknown tensions are obtained by solution of an auxiliary dense linear system that can be derived from the inextensibility condition: $\mathbf{r}_{ts} \cdot \mathbf{r}_s = 0$. Further details of the numerical method can be found in (6, 8). All simulations presented here were carried out in two dimensions using $N = 64$ points along the arc length of the filament. Typical time steps for the simulations were in the order of $\Delta t \sim 10^{-10} - 10^{-12}$.

Theoretical model

Dynamics of the J -shaped configuration. The initiation of a U turn in both experiments and simulations involves the formation of a J -shaped configuration which is tilted with respect to the flow direction and is a precursor to the snaking motion. To understand the transition to U turns, we seek a simplified model of this configuration using the geometry shown in Fig. S2. We approximate the bent portion of the filament by a semi-circle of yet unknown radius R and assume that the rest of the filament is straight and has a tilt angle ϕ with respect to the flow direction. We also introduce the following notations:

- $T^{(1)} \equiv$ velocity of the straight arm in the tangential direction $\hat{\mathbf{t}}$.
- $v_{\perp}^{AO} \equiv$ velocity of the straight arm in the normal direction $\hat{\mathbf{n}}$.
- $T(\theta) \equiv$ velocity of the semi-circle along $\hat{\mathbf{e}}_{\theta}$.
- $v_{\perp}^{OB}(\theta) \equiv$ Velocity of the semi-circle in the $\hat{\mathbf{e}}_r$ direction.
- $C(x_c, y_c) \equiv$ filament center of mass.
- $(x, y) \equiv$ global coordinate axes centered at O .
- $l \equiv$ length of the straight arm, also given by: $l = L - \pi R$ where L is the filament contour length.

Note that the assumption of a semi-circular shape for the bend leads to some inconsistencies. In particular, it is not possible to satisfy the force- and moment-free boundary conditions at point B . Adding a second straight arm emanating from B would allow circumventing this issue, and the model

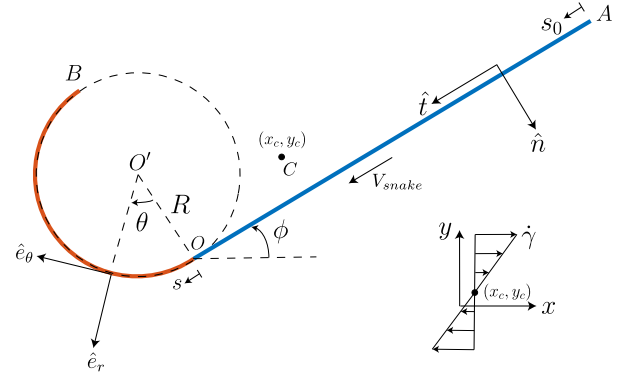


Fig. S2. Theoretical model of the J configuration. The bent part is approximated by a semi-circle of radius R . There is a snaking velocity V_{snake} along the contour of the shape. The straight part of the configuration has a tilt angle of ϕ with the direction of the flow.

we present here is justified in the limit of the length of that second arm becoming zero. Additional inconsistencies also arise at point O , where not all derivatives of the filament shape are continuous. These assumptions are necessary to make analytical progress, and we will see *a posteriori* that the model produces results that are in good agreement with experimental and simulation data. As we discuss later, the model does also satisfy a global energy balance that serves to make the assumptions rigorous while neglecting the boundary layers that may arise at geometric discontinuities.

With the definitions above, the relative velocity between the fluid and the straight arm in the tangential and normal directions can be expressed as:

$$v_{\parallel}^{rel} = T^{(1)} + \dot{\gamma} [(l - s_0) \sin \phi - y_c] \cos \phi, \quad [10]$$

$$v_{\perp}^{rel} = v_{\perp}^{AO}(s_0) - \dot{\gamma} [(l - s_0) \sin \phi - y_c] \sin \phi. \quad [11]$$

As there are no forces acting in the normal direction inside the straight arm, we set $v_{\perp}^{rel} = 0$ which yields

$$v_{\perp}^{AO}(s_0) = \dot{\gamma} [(l - s_0) \sin \phi - y_c] \sin \phi. \quad [12]$$

In the tangential direction, the internal tension $\sigma(s)$ induces an elastic force density $\mathbf{f}(s) = \sigma_s \hat{\mathbf{t}}$. This force density is balanced against viscous stresses using resistive force theory as $-\sigma_s = c_{\parallel} v_{\parallel}^{rel}$, which can be integrated using the force-free boundary condition at point A to yield

$$\sigma(s_0) = -c_{\parallel} T^{(1)} s_0 + c_{\parallel} \dot{\gamma} \left[\left(l s_0 - \frac{1}{2} s_0^2 \right) \sin \phi - y_c s_0 \right] \cos \phi. \quad [13]$$

We have introduced the coefficient of resistance per unit length in the tangential direction, which is expressed as

$$c_{\parallel} \approx \frac{2\pi\mu}{\log(2L/d)}, \quad [14]$$

and we similarly define $c_{\perp} \approx 2c_{\parallel}$ as the resistance coefficient for transverse motion.

We analyze the kinematics and force balance on the semi-circular arc in a similar fashion and first express the relative

velocities along the arc as

$$v_{\parallel}^{rel} = T + \underbrace{v_f \cos(\theta - \phi)}_{v_{\parallel}^f}, \quad [15]$$

$$v_{\perp}^{rel} = v_{\perp}^{OB} + \underbrace{v_f \sin(\theta - \phi)}_{v_{\perp}^f}, \quad [16]$$

where $v_f = \dot{\gamma}R [\cos \phi - \cos(\theta - \phi)] - \dot{\gamma}y_c$. Seeking a balance between elastic and viscous forces in the tangential and normal directions, we obtain:

$$-\frac{1}{R} \frac{d\sigma}{d\theta} = c_{\parallel} v_{\parallel}^{rel}, \quad [17]$$

$$\frac{\sigma}{R} + \frac{B}{R^3} = c_{\perp} v_{\perp}^{rel}. \quad [18]$$

The constraint of inextensibility introduces a kinematic relation between the Lagrangian velocities in the tangential and perpendicular directions everywhere along OB , and provides the condition:

$$\frac{dT}{d\theta} + v_{\perp}^{OB} = 0. \quad [19]$$

Eqs. (15)–(19) can be combined to yield a second-order non-homogeneous ODE for $v_{\perp}^{OB}(\theta)$:

$$2 \frac{d^2 v_{\perp}^{OB}}{d\theta^2} - v_{\perp}^{OB} = 2 \frac{d^2 v_{\perp}^f}{d\theta^2} + \frac{d^2 v_{\parallel}^f}{d\theta^2}. \quad [20]$$

This ODE can be solved analytically subject to continuity of the velocity at point O and to the tension-free boundary condition at point B :

$$v_{\perp}^{OB}(\theta) = C_1 \cosh(\lambda\theta) + C_2 \sinh(\lambda\theta) + \sum_{n=1,2} [\alpha_n \cos(n\theta) + \beta_n \sin(n\theta)], \quad [21]$$

where $\lambda = 1/\sqrt{2}$ and

$$C_1 = \frac{\dot{\gamma}R \sin 2\phi}{18}, \quad [22]$$

$$C_2 = \frac{B}{c_{\perp} R^3 \sinh(\pi\lambda)} - \frac{\dot{\gamma}R}{18} \sin 2\phi \tanh\left(\frac{\pi\lambda}{2}\right), \quad [23]$$

$$\alpha_1 = \dot{\gamma}(y_c - R \cos \phi) \sin \phi, \quad \alpha_2 = -\frac{5}{9} \dot{\gamma}R \sin 2\phi, \quad [24]$$

$$\beta_1 = -\dot{\gamma}(y_c - R \cos \phi) \cos \phi, \quad \beta_2 = \frac{5}{9} \dot{\gamma}R \cos 2\phi. \quad [25]$$

From v_{\perp}^{OB} , the tangential velocity along the bend is easily inferred as

$$T = v_{\parallel}^f - 2 \left(\frac{dv_{\perp}^{OB}}{d\theta} - \frac{dv_{\perp}^f}{d\theta} \right). \quad [26]$$

Seeking continuity of tangential velocity and internal tension at point O , we obtain two distinct expressions for the tangential velocity $T^{(1)}$ of the straight arm:

$$T^{(1)} = -\frac{2B\lambda}{c_{\perp} R^3 \sinh(\pi\lambda)} + \dot{\gamma}y_c \cos \phi - \frac{2}{9} \dot{\gamma}R \cos 2\phi + \frac{\dot{\gamma}R\lambda}{9} \sin 2\phi \tanh\left(\frac{\pi\lambda}{2}\right), \quad [27]$$

$$T^{(1)} = \frac{B}{c_{\parallel} R^2 l} - \frac{\dot{\gamma}l}{4} \sin 2\phi + \dot{\gamma}y_c \cos \phi. \quad [28]$$

Interestingly, Eq. (28) can be shown to also satisfy the torque balance on the filament.

For consistency, we require that Eqs. (27)–(28) be equal. Note, however, that both R and ϕ remain unknown at this point. We therefore seek a third condition based on dissipation arguments similar to those used to explain the tank-treading motion of vesicles (9). Over the course of an infinitesimal time interval δt during a U turn, a length of $\delta L \equiv V_{snake} \delta t$ that was initially straight becomes bent into the semi-circular curve of radius R , where V_{snake} is the snaking velocity. During that same time, the same small amount of length becomes straight on the other side of the bend. The amount of work required to bend the straight part can be estimated as the change in its elastic energy:

$$\delta E = \frac{B}{2} \frac{V_{snake} \delta t}{R^2}. \quad [29]$$

This expression provides an estimate for the rate of change $\dot{E} = \delta E / \delta t$ of bending energy due to the deformation of the filament at it undergoes snaking. An alternative expression can be obtained from first principles by differentiating the bending energy as:

$$\dot{E} = B \int_0^L \mathbf{r}_{ss} \cdot \mathbf{r}_{tss} ds. \quad [30]$$

Applying two integrations by parts and using the fact that tension forces do not perform any work leads to:

$$\dot{E} = B \int_0^L \mathbf{r}_t \cdot \mathbf{r}_{ssss} ds = \int_0^L \mathbf{r}_t \cdot \mathbf{f}^e ds \equiv - \int_0^L \mathbf{r}_t \cdot \mathbf{f}^h ds. \quad [31]$$

where \mathbf{r}_t is the velocity of a material point along the filament, and $\mathbf{f}^e = B \mathbf{r}_{ssss}$ is the local elastic force density whose work balances that of the hydrodynamic force density $\mathbf{f}^h = -[c_{\parallel} \mathbf{t} \mathbf{t} + c_{\perp} (\mathbf{I} - \mathbf{t} \mathbf{t})] \cdot \mathbf{v}^{rel}$. The detailed expression for the integral in Eq. (31) is cumbersome and therefore omitted here. The above derivation involves integration by parts and assumes continuity of derivatives. Equating (31) with $\delta E / \delta t$ from Eq. (29), and identifying the snaking velocity with the tangential velocity $T^{(1)}$ of the straight arm in the J shape, we obtain the additional condition:

$$\frac{BT^{(1)}}{2R^2} = - \int_0^L \mathbf{r}_t \cdot \mathbf{f}^h ds. \quad [32]$$

The above relation is essentially an integral energy balance in the system where we have included the dominant terms that come from the approximated J shape. In principle, there may be other terms arising from boundary layers near the junctions of approximate straight and semi-circular arcs which are ignored here in an asymptotic sense to facilitate analytical progress.

It is possible to recombine Eq. (27), Eq. (28) and Eq. (32) to form two equations for the unknowns R and ϕ . These two equations are then solved numerically using a Newton-search algorithm. The equations essentially specify two curves in the $\phi - R$ plane, and a solution only exists when the curves intersect. For a given aspect ratio of the filament, we find that there exists a critical value of $\bar{\mu}$ below which the curves do not intersect. This suggests that below this value J -shapes can no longer form and therefore U turns cannot occur. The theoretically calculated value of $\bar{\mu}_c^{(2)} / c \approx 1700$ is plotted as a

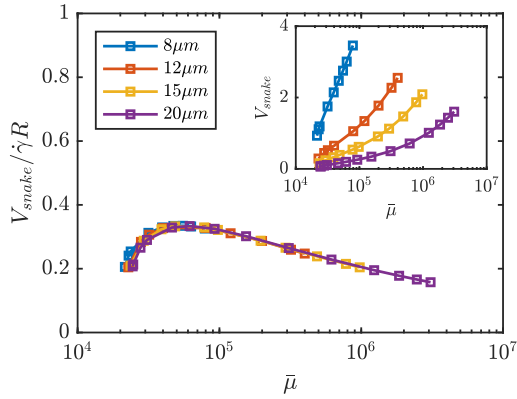


Fig. S3. Snaking velocity V_{snake} scaled by $\dot{\gamma}R$ as a function of $\bar{\mu}$ as predicted by our theoretical model. Inset: same data before rescaling by $\dot{\gamma}R$.

dashed line in Fig. 4 of the main article and indeed provides a very good estimate for the onset of U turns.

The model also provides the theoretical snaking velocity for the straight segment OA . The snaking velocities for different filaments with varying lengths are plotted in the inset of the Fig. S3 as a function of elasto-viscous number. After rescaling with the product of the bend radius R and shear rate $\dot{\gamma}$, all the data for different filament lengths collapse onto a master curve that only depends weakly on $\bar{\mu}$ in Fig. S3. This collapse therefore confirms that the relevant dynamic length and time scales during the snaking motion are R and $\dot{\gamma}^{-1}$, respectively.

Measurement of the bend radius. Our theoretical model approximates the J shape by a straight segment and a semi-circular arc. In this idealized configuration, the curvature is zero along the straight segment and then constant at $1/R$ over a length of $\delta_s = \pi R$. In experiments and simulations, however, the curvature varies smoothly and must reach zero at $s = L$ due to the boundary conditions. A typical curvature profile from a simulation is shown in Fig. S4. In order to estimate the radius R in a way that is consistent with the model, we measure the arclength δ_s over which the curvature, which increases from zero at $s = L$, decreases again to reach nearly zero. This measured length from simulations and experiments is shown in Fig. 6B of the main article and is in good agreement with the predictions from our model.

An alternative measure of the radius can also be obtained from the plateau of the bending energy during a snaking turn as seen in Fig. 2C of the main text. Since the majority of the energetic contribution comes from the sharp fold, we can get an estimate of the radius as

$$R = \frac{\delta_s}{\pi} \approx \frac{B\pi}{2\langle E \rangle}, \quad [33]$$

where $\langle E \rangle$ is the average bending energy over the plateau. This measure is also plotted against the theoretical predictions in Fig. 6B and follows similar trends.

In previous work, Harasim *et al.* (10) provided an expression for the bend radius that was independent of the length of the filament. For the parameter space explored in their study, they estimated $R \approx 1 \mu\text{m}$. Our results partially agree with their finding in the limit of long filaments and strong shear. In our model, experiments and simulations, we find that the value of δ_s decreases weakly with flow strength and is in the range of $R \sim 0.7 - 1.5 \mu\text{m}$.

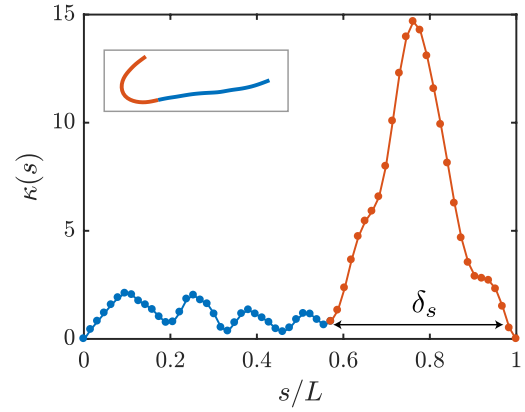


Fig. S4. Variation of curvature κ along the filament centerline for a typical J shape chosen from a simulation. The length marked as δ_s provides an estimate for the arclength of the bent portion.

Onset of J shape by global buckling

While our theoretical model for the J shape provides quantitative predictions for the onset of U turns and parameters characterizing the shape and dynamics, the detailed mechanism for the formation of a J shape from a nearly straight filament remains unclear. One mechanism, proposed by Lang *et al.* (11), hypothesizes that the filament buckles locally over the characteristic length scale of transverse thermal fluctuations. However, the threshold derived from this local buckling hypothesis is inconsistent with the transition from C buckling to U turn found in our simulations and experiments.

Another potential mechanism, which we elaborate on here, consists in global buckling of the filament at a small angle. To illustrate this mechanism, we show in Fig. S5 typical snapshots of filament configurations during the formation of the J shape from a simulation. From these images, we see that the mean filament orientation enters the compressional quadrant of the flow before significant deformations arise (configurations iii and iv). As the filament starts to buckle under compressional viscous stresses (configurations iv and v), its changed shape causes portions of it to become aligned with the direction of extension, even though the mean orientation remains in the compressional quadrant. This results in a tension profile that changes sign along the filament, which in turn causes differential bending and migration of the high-curvature region from the filament center towards one of the ends (configurations vii and viii), thus giving rise to a J shape (configuration ix). These findings are qualitatively different from C buckling, where the entire filament experiences compression as it buckles during global rotation.

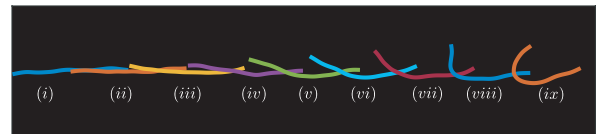


Fig. S5. Numerical simulation showing the onset of a J shape, which appears to result from buckling of the filament at a small angle.

Characterization of the transition regime

Brownian fluctuations are responsible for three effects: diffusion of the filament center of mass, rotational diffusion, and transverse shape fluctuations. In the present work, the effect of center-of-mass diffusion on the dynamics we observe can be neglected due to the large size of filaments. Orientational diffusion is well known to control the characteristic period of rotation in shear flow (11), and the length scales of polymer extension and transverse thickness resulting from the balance between shear viscous forces and fluctuations are also directly linked to bulk shear viscosities (12, 13). Our results suggest, however, that Brownian fluctuations do not play a significant role in determining the onset of the buckling instability and the transition between C and U dynamics. Nonetheless, fluctuations tend to smooth the transitions between regimes, with transitional regions that become broader with decreasing ℓ_p/L .

Near the transition from C buckling to U turns, we have noted that both types of dynamics can occur over multiple tumblings of the end-to-end vector. This resulted in the gray area in Fig. 4 of the main article. This stochastic transitional regime can be characterized more precisely by the probability of observing either shape, which we can estimate in simulations and is shown in Fig. S6 as a function of $\bar{\mu}$ for a fixed value of $\ell_p/L = 1.2$. As expected, we find that the probability of U turns continuously increases from 0 to 1 as $\bar{\mu}$ is varied across the transition. Similar stochastic transitions have been reported for the onset of buckling in compressional flows (14, 15).

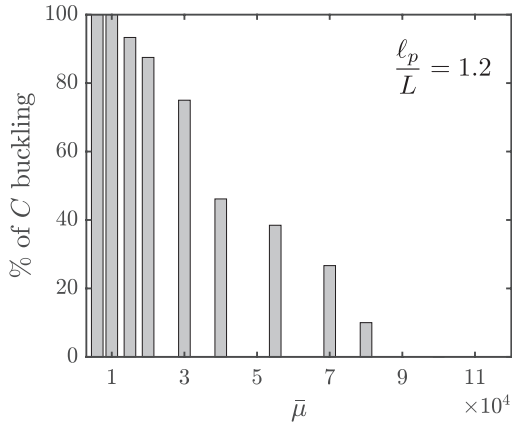


Fig. S6. Percentage of C buckling events as a function of $\bar{\mu}$ near the transition from C buckling to U turns in numerical simulations. The probability was estimated over a minimum of 10 distinct turns. The results shown are for $\ell_p/L = 1.2$.

Supplementary movie information

1. **Jeffery tumbling experiments:** Movies from experiments are shown in `rod-experiments.mov`. The relevant

parameters are $\ell_p/L = 3.75$ and $\bar{\mu} = 2.9 \times 10^3$.

2. **Jeffery tumbling simulations:** Movies from simulations are shown in `rod-simulation.mov`. The relevant parameters are same as above mentioned experiments.
3. **C buckling experiments:** Movies from experiments are shown in `C-experiments.mov`. The relevant parameters are $\ell_p/L = 2.9$ and $\bar{\mu} = 3.9 \times 10^3$.
4. **C buckling simulations:** Movies from simulations are shown in `C-simulation.mov`. The relevant parameters are same as above mentioned experiments.
5. **U turn experiments:** Movies from experiments are shown in `U-experiments.mov`. The relevant parameters are $\ell_p/L = 0.84$ and $\bar{\mu} = 2.1 \times 10^6$.
6. **U turn simulations:** Movies from simulations are shown in `U-simulation.mov`. The relevant parameters are same as above mentioned experiments. Over the multiple tumbling events shown in these movies we also observe an occasional S turn.

1. Powers TR (2010) Dynamics of filaments and membranes in a viscous fluid. *Rev. Mod. Phys.* 82(2):1607.
2. Gittes F, Mickey B, Nettleton J, Howard J (1993) Flexural rigidity of microtubules and actin filaments measured from thermal fluctuations in shape. *J. Cell Bio.* 120:923–923.
3. Isambert H, et al. (1995) Flexibility of actin filaments derived from thermal fluctuations. Effect of bound nucleotide, phalloidin, and muscle regulatory proteins. *J. Biol. Chem.* 270:11437–11444.
4. Brangwynne CP, et al. (2007) Bending dynamics of fluctuating biopolymers probed by automated high-resolution filament tracking. *Biophys. J.* 93:346–359.
5. Johnson RE (1980) An improved slender-body theory for Stokes flow. *J. Fluid Mech.* 99:411–431.
6. Tornberg AK, Shelley MJ (2004) Simulating the dynamics and interactions of flexible fibers in Stokes flows. *J. Comp. Phys.* 196:8–40.
7. Munk T, Hallatschek O, Wiggins CH, Frey E (2006) Dynamics of semiflexible polymers in a flow field. *Phys. Rev. E* 74:041911.
8. Manikantan H, Saintillan D (2013) Subdiffusive transport of fluctuating elastic filaments in cellular flows. *Phys. Fluids* 25:073603.
9. Rioual F, Biben T, Misbah C (2004) Analytical analysis of a vesicle tumbling under a shear flow. *Phys. Rev. E* 69:061914.
10. Harasim M, Wunderlich B, Peleg O, Kröger M, Bausch AR (2013) Direct observation of the dynamics of semiflexible polymers in shear flow. *Phys. Rev. Lett.* 110:108302.
11. Lang PS, Obermayer B, Frey E (2014) Dynamics of a semiflexible polymer or polymer ring in shear flow. *Phys. Rev. E* 89:022606.
12. Teixeira RE, Babcock HP, Shaqfeh ES, Chu S (2005) Shear thinning and tumbling dynamics of single polymers in the flow-gradient plane. *Macromolecules* 38(2):581–592.
13. Schroeder CM, Teixeira RE, Shaqfeh ES, Chu S (2005) Dynamics of DNA in the flow-gradient plane of steady shear flow: observations and simulations. *Macromolecules* 38(5):1967–1978.
14. Kantsler V, Goldstein RE (2012) Fluctuations, dynamics, and the stretch-coil transition of single actin filaments in extensional flows. *Phys. Rev. Lett.* 108:038103.
15. Manikantan H, Saintillan D (2015) Buckling transition of a semiflexible filament in extensional flow. *Phys. Rev. E* 92:041002.

List of Figures

Chapter 1	1
1.1 Parametrization of the filament. $\mathbf{r}(s, t)$ describes the centerline of the filament along the arclength s , at time t . d is the filament diameter. The tangential vector is the derivative of $\mathbf{r}(s, t)$ with respect to s , $\mathbf{t}(s) = \mathbf{r}_s$	5
1.2 Critical values of $\bar{\mu}/c$ and corresponding buckling modes from linear stability analysis and experiments (Quennouz et al., 2015).	9
1.3 (A): Experimental study of the dynamics of flexible fibers in an array of stagnation points (Wandersman et al., 2010). (B): Buckling under compression of fluctuating filaments - actin - held at a stagnation point by microfluidic device (Kantsler and Goldstein, 2012). (C): Amplitude of the first buckling mode of non-Brownian filaments (black dash line) and Brownian filaments (colorful lines and markers) as a function of flow strength in numerical simulations (Manikantan and Saintillan, 2015).	10
1.4 (A): Numerical study of flow-induced helical coiling of Brownian filaments in a diverging channel (Chelakkot et al., 2012). (B): Actin filaments dynamics in a confined hyperbolic channel (Strelnikova et al., 2017).	10
1.5 Schematic of a straight rod in a simple shear flow	11
1.6 (A): Original experiment on the dynamics of millimetric elastic fibers in a Couette cell (Forgacs and Mason, 1959a) . (B): Superimposition of the configurations of flexible filaments in shear flow while rotating obtained from numerical simulations (Becker and Shelley, 2001). (C): Numerical simulations of a long flexible fiber in shear flow (Nguyen and Fauci, 2014). (D): Experimental studies of the dynamics of actin filaments in microfluidic channel (Harasim et al., 2013).	12
1.7 (A): Diffusive and advective phases of a tumbling event for a Brownian filament. (B): Polar probability density of the mean orientation of the filament from simulations at three different flow strengths. The shear flow is from right to left in the upper half and the opposite in the lower half (Harishankar, 2009).	13

1.8	(A)-(left): Scaled Power spectral density of polymer orientation angle for DNA in steady shear flow for experiment and simulation at $Wi = 49$. (A)-(right): Scaling of peak frequencies as function of Wi of two DNA molecules with different length (Schroeder et al., 2005a). (B)-(left): Numerical work on dynamics of semiflexible polymer shows The rescaled tumbling frequency $f_c \tau Wi^{-3/4}$ is shown as a function of $(\ell_p/L)Wi^{-1/3}$. (B)-(right): Comparison of simulational results from (Lang et al., 2014) and experimental results from (Harasim et al., 2013) on the frequency scale between $f_c \tau$ and Wi	13
1.9	The behaviors of Non-Newtonian fluids. (A): Dynamic deformation snapshots of Oobleck (starch suspension) under sine wave (Bond, 2011). (B): Die swell in Newtonian and polymeric liquids (PSIDOT, 2007). (C): Rod climbing effect (McKinley, 2008).	14
1.10	(A): first normal stress difference caused by straight filament with dashed line and buckling filaments with solid line (corresponding shapes on the top) (Tornberg and Shelley, 2004). (B): Asymptotic contributions of tensile, bending and thermal forces to shear modulus for semiflexible filaments $L \gg \ell_p$ (Shankar et al., 2002).	15
1.11	Experimental set combining a rheometer and confocal imaging to measure the shear viscosity of semi-dilute of actin filaments and corresponding configurations (Kirchenbuechler et al., 2014).	15
Chapter 2		21
2.1	Actin filaments related different cellular processes	22
2.2	Polymerization of actin monomers into filaments: (A) Crystal structure of actin monomer (Otterbein et al., 2001). (B) Formation of spontaneous nucleus. (C) Polymerization of filaments with helical structure in the presence of Alexa 488 Phalloidin.	23
2.3	2D confinement to observe the fluctuations of filaments in solution	26
2.4	Image processing procedure of first four modes configurations	27
2.5	Brownian fluctuation of actin filaments in solution	28
2.6	(left): Cosine correlation function of tangential vectors over a distance l . (right): Persistence length ℓ_p measured in different viscosities	29
Chapter 3		31
3.1	A picture of the experimental setup.	33
3.2	Sketch of the experimental device.	34
3.3	(Left) Linear approximation of the flow velocity in the observation plane. (Right) Solid line: The ratio of shear rates at $z = 150 \mu\text{m}$. Dashed line: $\dot{\gamma}_y/\dot{\gamma}_z = 10$	34

3.4	(Left) Velocity profiles of different flow rates in observation plane xOy . (Right) Velocity profile along z in the centre for a flow rate $Q = 7.5 \text{ nl/s}$. Solid lines of different colors are theoretical velocities and markers are the corresponding experimental measurements obtained through PIV.	35
3.5	Operation flow chart of Labview program.	36
3.6	The interface of the Labview program.	37
3.7	Raw image and reconstructed image with corresponding parameters.	37
3.8	The decomposition of shear flow into a rotational and a straining part.	40
3.9	Typical dynamics of filaments in shear flow observed in experiments.	41
3.10	Local curvatures propagating along the arc length over time. Each color line represents the curvature along the arc length at different time steps. Colour frames indicate the type of dynamics: (a) Rod-like tumbling, (b) C shape buckling, (c) U snake turn, (d) S snake turn.	41
3.11	Temporal evolution of the filament performing rod-like tumbling in planar shear over one period of motion, comparing experimental images (E) to simulations (S). $\ell_p/L = 3.75$, $\bar{\mu} = 2.9 \times 10^3$	42
3.12	The evolution of parameters of a filament performing rod-like tumbling, including the sphericity parameter ω , mean angle χ with respect to the flow direction, bending energy E and scaled end-to-end distance L_{ee}/L over a few periods of motion. Symbols are measurements from experiments and the solid lines are from simulations.	42
3.13	Temporal evolution of the filament performing C shaped buckling in pla- nar shear over one period of motion, comparing experimental images (E) to simulations (S). $\ell_p/L = 2.9$, $\bar{\mu} = 3.9 \times 10^3$	42
3.14	The evolution of parameters of a filament performing C shaped buckling dynamics, including the sphericity parameter ω , mean angle χ with re- spect to the flow direction, bending energy E and scaled end-to-end dis- tance L_{ee}/L over a few periods of motion. Symbols are measurements from experiments and the solid lines are from simulations.	43
3.15	Temporal evolution of the filament performing a U snake turn in planar shear over one period of motion, comparing experimental images (E) to simulations (S). $\ell_p/L = 0.83$, $\bar{\mu} = 2,0 \times 10^6$	43
3.16	The evolution of parameters of a filament performing U snake turns, in- cluding the sphericity parameter ω , mean angle χ with respect to the flow direction, bending energy E and scaled end-to-end distance L_{ee}/L over a few periods of motion. Symbols are measurements from experiments and the solid lines are from simulations.	44
3.17	Temporal evolution of the filament performing a S snake turn in planar shear over one period of motion, comparing experimental images (E) to simulations (S). $\ell_p/L = 0.83$, $\bar{\mu} = 2,0 \times 10^6$	45

3.18	The evolution of parameters of a filament performing S snake turn dynamics, including the sphericity parameter ω , mean angle χ with respect to the flow direction, bending energy E and scaled end-to-end distance L_{ee}/L over a few periods of motion. Symbols are measurements from experiments and the solid lines are from simulations.	45
3.19	Complex configurations of long filaments under shear comparing experimental results and simulations results Nguyen and Fauci (2014)	46
3.20	The evolution of the maximum bending energy E (left) and the minimum value of the sphericity parameter ω (right) as a function of the elasto-viscous number $\bar{\mu}$ in the different regimes. Full symbols are experimental results; open symbols are simulation results.	47
3.21	$\Delta\chi/\pi = (max(\chi) - min(\chi))/\pi$ as a function of $\bar{\mu}$	47
3.22	Phase chart indicating the different regimes in the $(\bar{\mu}/c, \ell_p/L)$ parameter space. The dashed black lines show the theoretical transitions from stability analysis and U turn dynamics analysis, full symbols are experiments, open symbols are simulations.	48
3.23	Percentage of C buckling events as a function of $\bar{\mu}$ near the transition from C buckling to U turns. The probability is estimated over 10 distinct turns. The results shown are for $\ell_p/L = 1.2$	49
3.24	(A) A typical J shape before the initiation of a U turn taken from an experimental image. (B) The bent part is approximated by a semicircle of radius R ; the straight part has a tilt angle of ϕ with the direction of the flow and there is an axial velocity V_{snake}	50
3.25	Theoretical model of the J configuration. The bent part is approximated by a semi-circle of radius R . There is a snaking velocity, V_{snake} along the contour of the shape. The straight part of the configuration has a tilt angle of ϕ with the direction of the flow.	51
3.26	Snaking velocity V_{snake} scaled by $\dot{\gamma}R$, the product of shear rate and semicircle radius, as a function of elasto-viscous number $\bar{\mu}$ as predicted by our theoretical model. Inset: V_{snake} as function of $\bar{\mu}$ with different contour lengths.	54
3.27	(L): Variation of curvature κ along the filament centerline for a typical J shape chosen from a simulation. The length marked as δs provides an estimate for the arclength of the bent portion. (R): Comparison of measurements of the length of the bending portion normalized by L vs the elasto-viscous number $\bar{\mu}$ during a U turn.	55
3.28	(L) Theoretical predictions compared with experiments and simulations on the tilt angle of the J shape with the direction of flow. (R) Snaking velocity rescaled with $\dot{\gamma}R_{th}$ plotted against $\bar{\mu}$ comparing experiments, simulations and theory; here R_{th} is theoretically predicted radius.	56

3.29 (L): The periodically varying of the scaled mean orientation χ/π . (R): The probability distribution of scaled mean orientation $\chi\pi$ during multiple rotations. The filament performs tumbling and buckling during the multiple rotations.	57
3.30 Frequency scaling for a limited number of rotations. The tumbling frequency f is non-dimensionalized by the relaxation time $\tau = 8\pi\mu L^4/Bc$, where μ is viscosity, L is the length of the filament, B is bending rigidity and $c = -\ln(e^2/e)$ is the slenderness.	58
Chapter 4	61
4.1 The geometry of the microfluidic channel (processed experimental image). The left part corresponds to the flow focusing device, the right part to the hyperbolic channel. The connection between parts is a straight part with a length of $5mm$ to let filaments relax after flow focusing.	64
4.2 The top view of the optimized hyperbolic channel with the upstream part width $W_u = 800\mu m$, the contraction part width $W_c = 100\mu m$, the height of the channel $H = 100\mu m$, geometry parameters $n_1 = l_c/W_u = 2$ and $n_2 = 1$ (processed experimental image of microfluidic device).	64
4.3 Ideal velocity profile (a) and extension rate profile (b) along the centreline of the flow	65
4.4 The diagram of pulses and information exchange of the Labview program. .	68
4.5 (a) Comparison between flow velocity $u(x)$ (black line), Mathematica code simulated stage velocity $\hat{u}(x_i)$ (red "+") and actual velocity of the stage $\check{u}(x_i)$ (blue "x"). (b) Comparison between flow displacement $x(t)$ (black line), Mathematica code simulated stage displacement $\hat{x}(t_i)$ (red "+") and actual displacement of the stage $\check{x}(t_i)$ (blue "x"). (c): The difference in displacement Dx between the flow and predicted stage motion (red "+") as well as the difference between flow and actual stage motion (blue "x"). (d): Image blur during exposure time due to the velocity difference between the flow and predicted stage motion (red "+") and actual stage motion (blue "x"). . .	69
4.6 (Left): Velocity as a function of position. (Right): Displacement as a function of time. The markers represent the real movement of the stage, and the lines are the corresponding calculated flow profiles. Capital letters represent different geometries as shown in table 4.1.	70
4.7 The temporal configurations of three different filaments in hyperbolic channels. The lengths are $12.2\mu m$, $27.4\mu m$, $57.8\mu m$ respectively. The maximum strain rates they experience are $0.34s^{-1}$, $0.61s^{-1}$, $0.65s^{-1}$ respectively. The governing parameter $\bar{\mu}/c$ they experiences during maximum strain rate are 1.1×10^3 , 4.5×10^4 , 8.8×10^5 respectively. Positive strain rate represents extensional flow, negative strain rate represents compressive flow.	71

4.8	The temporal configurations of a filament in a hyperbolic channel and the corresponding measured quantities. (a) Comparison of velocities between calculated flow profile and actual velocity of the filament. (b) Evolution of the parameters a_{\perp}/L and L_{ee}/L as well as the strain rate.	72
4.9	Measurement of the transverse amplitude a_{\perp}	72
4.10	(left): The average scaled end to end distance as a function of Peclet number. (right): The average amplitude of transverse fluctuations as a function of Peclet number.	73
4.11	Scaled filament end point fluctuations as a function of scaled tension.	74
4.12	Complex three dimension coiling structures of different filaments under compression. Brownian fluctuations and different in lengths and strain rates make the configurations are diverse and complex.	75
4.13	The time derivative of the end to end distance as function of $\dot{\epsilon}L$ in the homogeneous compression part of the channel.	76
4.14	(A) : Numerical study of flow induced helical coiling of Brownian filaments in a diverging channel (Chelakkot et al., 2012). (B) : The solidification of synthetic wet-spun fibers in converging and diverging channel (Mercader et al., 2010). (C) : Buckling of microtubules with helical structure when they passing through a septal pore (Pieuchot et al., 2015). (D) : Complex configuration in three dimension of a long flexible filament in shear flow (Nguyen and Fauci, 2014).	78

Chapter 5 **81**

5.1	(A) : First normal stress difference $\langle N_1 \rangle = \langle S_{11} - S_{22} \rangle$ and shear stress $\langle S_{12} \rangle$ as a function of $\bar{\mu}/c$. (B) : Shear-viscosity μ_s as a function of $\bar{\mu}/c$ (Chakrabarti and Saintillan, in preparation).	83
5.2	Sketch of the Y-channel with two co-flowing fluids driven by identical flow rates. The frame corresponds to the visual field of the camera.	83
5.3	(left): Example of an image of co-flow of actin filament suspension (left part, fluorescent G-actin) and reference fluid (F-buffer, right part). (right): Detection of the interface through curve fitting of an error function to the intensity profile.	84
5.4	(A) : The intensity profile between fluorescein solution (left part) and distilled water (right part) for different flow rates. The inset image is a zoom of the interface regime. (B) : The apparent viscosity ratio between the two fluids.	85
5.5	Sketch of a filament polymerized from a spectrin-actin seed.	86
5.6	The time evolution of monomer concentration and average length of suspension and the corresponding protocol.	87
5.7	Filaments fabricated for short suspension and its length distribution.	88
5.8	Filaments fabricated for medium suspension and its length distribution.	89

5.9	Filaments fabricated for long suspension and its length distribution.	89
5.10	Varying interface between suspension (fluorescent) and reference fluid (dark) as increasing flow rate. Red lines are two walls.	89
5.11	(A): The shear viscosities of semi-dilute suspension as a function of average shear rate. (B): The shear viscosities of dilute short suspension as a function of average shear rate.	90
Appendix A		99
A.1	Fluctuations along flow with amplitude $h(x)$ away from the x -axis.	99

List of Tables

2.1	The compositions of different buffers	25
2.2	Viscosity of F-buffer varing with sucrose concentration	25
4.1	The dimensions of different optimized hyperbolic channels.	67
4.2	The actual dimensions of the experimental geometries.	67
5.1	Preparation of different suspensions: Composition of the solution, average length obtained and volumic fraction.	88

